Development of a Raman microscope for applications in radiobiology

by

Quinn Matthews

BSc, University of Victoria, 2006

A Dissertation Submitted in Partial Fulfillment of the
Requirements for the Degree of

Masters of Science

in the Department of Physics and Astronomy

University of Victoria

Development of a Raman microscope for applications in radiobiology

by

Quinn Matthews

BSc, University of Victoria, 2006

Supervisory Committee

Dr. A. Jirasek, Supervisor (Department of Physics and Astronomy)

Dr. M. Lefebvre, Member (Department of Physics and Astronomy)

Dr. W. Ansbacher, Member (British Columbia Cancer Agency - Vancouver Island Centre)

Dr. A. Brolo, External Examiner (Department of Chemistry - University of Victoria)

Supervisory Committee

Dr. A. Jirasek, Supervisor (Department of Physics and Astronomy)

Dr. M. Lefebvre, Member (Department of Physics and Astronomy)

Dr. W. Ansbacher, Member (British Columbia Cancer Agency - Vancouver Island Centre)

Dr. A. Brolo, External Examiner (Department of Chemistry - University of Victoria)

Abstract

Raman microscopy (RM) is a vibrational spectroscopic technique capable of obtaining sensitive measurements of molecular composition, structure, and dynamics from a very small sample volume ($\sim$1 μm^3). In this work, a RM system was developed for future applications in cellular radiobiology, the study of the effects of ionizing radiation on cells and tissues, with particular emphasis on the capability to investigate the internal molecular composition of single cells (10-50 μm in diameter). The performance of the RM system was evaluated by imaging 5 μm diameter polystyrene microbeads dispersed on a silicon substrate. This analysis has shown that RM of single cells is optimized for this system when using a 100x microscope objective and a 50 μm confocal collection aperture. Quantitative measurements of the spatial, confocal, and spectral resolution of the RM system have been obtained using metal nanostructures deposited on a flat silicon substrate. Furthermore, a spectral investigation of several substrate materials was successful in identifying low-

fluorescence quartz as a suitable substrate for RM analysis of single cells. Protocols have been developed for culturing and preparing two human tumor cell lines, A549 (lung) and DU145 (prostate), for RM analysis, and a spectroscopic study of these two cell lines was performed. Spectra obtained from within cell nuclei yielded detectable Raman signatures from all four types of biomolecules found in a human cell: proteins, lipids, carbohydrates, and nucleic acids. Furthermore, Raman profiles and 2D maps of protein and DNA distributions within single cells have been obtained with micron-scale spatial resolution. It was also found that the intensity of Raman scattering is highly dependent on the concentration of dense nuclear material at the point of Raman collection. RM shows promise for studying the interactions of ionizing radiation with single cells, and this work has been successful in providing a foundation for the development of future radiobiological RM experiments.

Table of Contents

Supervisory Committee **ii**

Abstract **iii**

Table of Contents **v**

List of Tables **vii**

List of Figures **viii**

Acknowledgements **xii**

1 Introduction **1**

1.1 Radiation therapy 1

1.2 Cellular radiobiology 3

1.3 Overview of modern biomedical Raman microscopy 12

1.4 Thesis scope 15

2 Raman Spectroscopy **17**

2.1 History 17

2.2 Theory of Raman scattering 19

2.3 Raman spectroscopy instrumentation 26

2.4 Raman microscopy instrumentation 32

2.5 Raman microscopy of biological materials 35

2.6 Advantages and disadvantages of Raman spectroscopy 38
2.7 Some modern applications of Raman spectroscopy 39

3 Materials & Methods **41**
3.1 General Raman microscopy 42
3.2 Raman microscopy of human tumor cells 51

4 Results and Discussion I:
Raman microscope development and characterization **55**
4.1 Qualitative investigation of optimum parameters for cellular imaging 56
4.2 Spatial, confocal, and spectral resolution 72
4.3 Substrate materials for biological Raman microscopy 76
4.4 Summary 82

5 Results and Discussion II:
Raman microscopy of human tumor cells **84**
5.1 Single-point spectra of A549 and DU145 cell nuclei 85
5.2 Raman profiles across A549 and DU145 cells 94
5.3 Raman mapping of cells 99
5.4 Intra-batch cell spectral variability 104

6 Conclusions and Future Work **110**
6.1 Conclusions 110
6.2 Future work 111

Bibliography **113**

List of Tables

5.1 Peak assignment for Raman spectra of A549 and DU145 cells. Superscript numbers indicate references used for the particular assignment. 93

List of Figures

1.1 Schematic diagrams of (a) the general structure of an amino acid and (b) the joining of two amino acids in a dehydration reaction 4
1.2 Block diagram of a section of double-stranded DNA 4
1.3 (a) Single dose survival curves and (b) fractionated dose survival curves 8

2.1 Energy level diagram for a molecule irradiated with optical photons of frequency v_0 19
2.2 (a)-(c) Normal mode vibrations of the CO_2 molecule and (d) symmetric ring breathing of benzene 24
2.3 Changes in polarizability ellipsoids during normal mode vibrations of CO_2 25
2.4 General schematic of the light path for a typical Raman spectroscopy system 27
2.5 Design of a Czerny-Turner dispersive spectrometer 28
2.6 The arrangement of a CCD detector array placed at the focal plane of the spectrometer 31
2.7 General schematic of the light path for a typical RM system 33
2.8 Example of numerical apertures (NA) calculated for two microscope objectives 33
2.9 Principle of confocal Raman microscopy 36

3.1 Schematic of the RM system developed for this work 42

3.2 Example of applying TPMEM smoothing to a raw Raman spectrum . 49
3.3 Example of applying the signal removal method for baseline estimation 50
3.4 Optical images of (a) A549 and (b) DU145 human tumor cells 52

4.1 Relative (a,b) optical images and (c,d) X-Y profiles of the focused laser spot for the (a,c) 50x and (b,d) 100x objectives 57
4.2 Sample Raman spectrum obtained from the centre of a polystyrene microbead resting on a silicon substrate 58
4.3 Optical microscope images of 5 μm diameter polystyrene beads on silicon 59
4.4 Spatial maps of the polystyrene signal from the single and triple bead patterns, for step sizes of (a,b) 0.8 μm, (c,d) 0.4 μm, and (e,f) 0.2 μm 60
4.5 Horizontal averaged profiles 61
4.6 Normalized depth profiles from the (a,b) single and (c,d) triple bead patterns for the (a,c) 50x and (b,d) 100x objectives and 50 μm and 100 μm confocal apertures 63
4.7 Spatial maps of the polystyrene signal from single bead scans, for the 50x and 100x objectives and the 50 μm and 100 μm confocal apertures 65
4.8 Spatial maps of the silicon signal from the single bead scans 66
4.9 Spatial maps of the polystyrene signal from the triple bead pattern scans, for 50x and 100x objectives and for 50 μm and 100 μm apertures 69
4.10 Spatial maps of the silicon signal from the triple bead pattern scans . 70
4.11 Horizontal profiles through the middle region of the bottom two beads 71
4.12 Optical images of 300 nm wide wire 73
4.13 (a) Raw and deconvolved LSFs obtained from scanning across a 300 nm wire on a silicon substrate, and (b) the corresponding MTFs . . . 73
4.14 (a) Line spread functions and (b) corresponding MTFs, obtained from depth profiles through the silicon surface 74

4.15 (a,b) Raw measured, theoretical, and deconvolved silicon spectra with (c,d) the corresponding MTFs 75
4.16 Raman spectra of common substrate materials for cell culture that are unsuitable for Raman imaging 77
4.17 Raman spectra of the first group of CaF_2 disks obtained 78
4.18 Depth profiles through the surface of a CaF_2 disc 79
4.19 Raman spectra of the second group of CaF_2 disks obtained 79
4.20 Raman spectra of GE 124 type and Corning 7980 type low-fluorescence quartz 81
4.21 Raman spectra, in the window of interest for biological RM (600-1800 cm^{-1}), of Corning 7980 type low-fluorescence quartz discs 82

5.1 Optical microscope images of A549 cells 1-4 86
5.2 Optical microscope images of DU145 cells 1-4 87
5.3 Single-point Raman spectra of the four A549 cell nuclei 88
5.4 Single-point Raman spectra of the four DU145 cell nuclei 89
5.5 Raman peak assignments for A549 (cell 2) and DU145 (cell 3) spectra 91
5.6 Optical images and Raman peak profiles of A549 cells (a) 1, (b) 2, (c) 3, and (d) 4 96
5.7 Optical images and Raman peak profiles of DU145 cells (a) 1, (b) 2, (c) 3, and (d) 4 97
5.8 (a) Optical image, (b,c) sample spectra, and (d,e) protein maps of A549 cell #4 100
5.9 (a,b) Raman DNA maps of A549 cell #4, compared to (c,d) maps generated from the “no signal” region of same data set 102
5.10 (a) Optical image, (b,c) sample spectra, and (d,e) protein maps of DU145 cell #3 103

5.11 (a,b) Raman DNA maps of DU145 cell #3, compared to (c,d) maps generated from "no signal" region of same data set 105

5.12 Relationship between mean grayscale intensity in A549 cell nuclear regions and the Raman peak intensity 108

Acknowledgements

I'd like to thank the staff of the Deeley Research Center at the BC Cancer Agency, in particular May Wong, Rob Sahota, and Dr. Xiaobo Duan, for helping me with all things biological during the course of this project. A big thank you also goes out to Dave Smith in the machine shop for making pretty much anything I asked him to make, and doing an excellent job of it as well. Thanks as well to the nanomagnetism group next door for letting me shoot lasers at some of their old samples. I'd like to sincerely thank my committee members, Dr. Will Ansbacher and Dr. Michel Lefebvre, and my external examiner, Dr. Alex Brolo, for reading my thesis and providing excellent feedback. I look forward to working more closely with all of you in the future. Finally, a huge thank you to my supervisor, Dr. Andrew Jirasek, for buying me lab stuff, not reaming me out when I break said stuff, keeping me on track, providing constant support and expertise, and ultimately guiding me through the project from start to finish.

Chapter 1

Introduction

1.1 Radiation therapy

Since the discovery of the X-ray in 1895 by Wilhelm Conrad Röntgen [1], the medical applications of ionizing radiation have been numerous and extremely beneficial [2]. The first therapeutic use of X-rays, for treatment of superficial cancers, occurred shortly after Pierre and Marie Curie's discovery and isolation of the radioactive elements polonium and radium in 1898 [3]. The introduction of cobalt treatment units and clinical linear accelerators in the 1950s [4] provided the means for clinical production of higher energy photons, allowing for the treatment of deep-seated tumor sites. This advancement revolutionized the field and paved the way for such modern treatments as 3D conformal radiation therapy (3DCRT), intensity modulated radiation therapy (IMRT), image-guided radiation therapy (IGRT), tomotherapy, and many others.

Radiation therapy is now the prescribed method of treatment for about one-third of all cancer patients. It is estimated that over 50,000 Canadians will undergo radiation therapy for newly diagnosed cancer in 2008 [5]. Many radiation therapy patients have highly successful treatments, greatly improving their quality of life and increasing their life expectancy. Some patients, however, have much more limited levels of success; the outcome of a treatment may vary depending on the type and

location of the tumor, the level of progression of the disease, and an individual's response to the treatment. Almost all patients experience side-effects from radiation therapy, ranging from mild to debilitating, due to the negative effects of radiation on healthy tissue.

The primary goal of modern radiation therapy is to maximize the radiation dose to the known tumor volume while minimizing the dose to the surrounding healthy tissue. With modern advances in medical imaging technology (ultrasound, computed tomography, medical resonance imaging, etc...) the position and shape of the tumor can be determined and digitized very accurately, provided that the bulk of the tumor is easy to visualize (areas of microscopic disease are difficult to locate). Using radiation delivery techniques such as 3DCRT and IMRT, the radiation treatments can be designed to conform to the 3D tumor volume, greatly minimizing the dose to surrounding healthy tissue. Ideally, the correct amount of dose, as prescribed by the radiation oncologist for a curative treatment of the tumor, will be successfully delivered to the desired location with minimal irradiation of surrounding organs and tissues. The exact mechanisms and physical bases behind the generation, delivery, and verification of such clinical treatments are described in detail in standard medical physics and radiotherapy texts [6, 7].

The ability to quantify and understand the interactions of radiation with biological tissues is vital to the success of any radiation treatment. With increased understanding of the fundamental processes that cause damage to human cells and tissues, both healthy and cancerous, the benefit to an individual patient could potentially be greatly increased. However, before any further discussion it is necessary to understand the basics of the field of radiobiology, as applied to human cells and tissues.

1.2 Cellular radiobiology

1.2.1 Biomolecules and the human cell

At its very simplest, the human cell is a collection of biological molecules, or biomolecules, organized into the single living unit that is the building block of life. These biomolecules can be classified as either nucleic acids (e.g. DNA, RNA), proteins (e.g. enzymes, structural or transport molecules), lipids (e.g. phospholipids in the cell membrane, fatty acids), or carbohydrates (e.g. sugars, starch, glycogen). Human cells consist of membrane bound organelles suspended in cytoplasm, a saline solution that is 70-85% water, surrounded by a phospholipid bilayer membrane. In terms of biomolecule composition, the non-cytoplasmic parts of the cell are ∼79% protein, ∼5% nucleic acid, ∼11% lipid, and ∼5% carbohydrate [8]. The largest organelle is the nucleus, which contains the cell's DNA, the genetic material responsible for the cell's proper function and reproduction. The highest concentrations of protein and nucleic acids are found in the cell nucleus. The results presented in chapter 5 will largely focus on protein and nucleic acids, so a brief description of these two classes of biomolecules is warranted.

Proteins are large molecules composed of a collection of amino acids linked together by peptide bonds. A single amino acid has an amine group, a carboxyl group, and a side-chain (**R**) specific to the amino acid (figure 1.1a). When two amino acids join together they undergo a dehydration reaction, forming an amide group (N-C=O) containing the peptide bond (C-N) and a water molecule (figure 1.1b). There are 20 standard amino acids used for protein synthesis. The ordering of amino acids, specified by the cell's genetic code, determines the type of protein synthesized.

The primary nucleic acid in the cell is deoxyribonucleic acid (DNA). A single strand of DNA contains a chain of alternating sugar and phosphate groups, forming the *backbone* of the strand. Attached to each sugar group is a nitrogen-containing

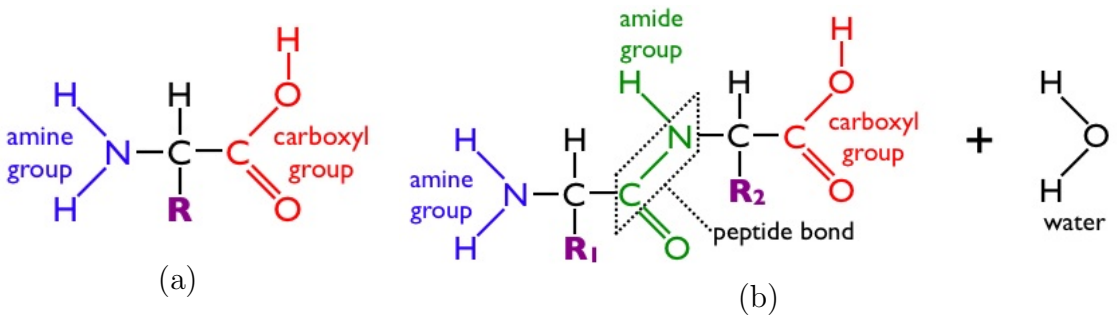

Figure 1.1: Schematic diagrams of (a) the general structure of an amino acid showing the amine and carboxyl groups and location of the side-chain, and (b) the joining of two amino acids in a dehydration reaction forming an amide group with a peptide bond, and a water molecule.

molecule called a *base*. The four DNA bases are classified into two groups based on their chemical structure: the *pyrimidines*, thymine (T) and cytosine (C), have a single ring, and the *purines*, adenine (A) and guanine (G), have a double ring. In double-stranded DNA the bases on one strand form hydrogen bonds with bases on the other strand, and the two strands intertwine into a double-helix. Due to the chemical structure of the bases, T always forms hydrogen bonds with A, and C with G, making the two strands in the DNA helix complementary to each other (figure 1.2). The sequence of the bases in DNA is the recipe for protein synthesis, the origin of genetic traits, and is responsible for directing the activities of the cell.

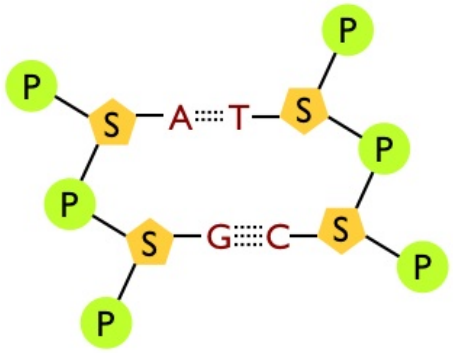

Figure 1.2: Block diagram of a section of double-stranded DNA, showing the backbone of alternating sugar (S) and phosphate (P) groups and the hydrogen bonding (dotted lines) of the bases adenine (A), thymine (T), guanine (G), and cytosine (C).

Before onset of DNA replication, which is necessary to provide each of the two

cells formed during division (daughter cells) with the necessary complement of DNA, the DNA helices are packed with nuclear proteins into dense units called *chromosomes*. During DNA replication each chromosome is duplicated to form two *sister chromatids*. The sequence of bases is copied and shared between the two daughter cells during cell division (mitosis), thus passing the necessary genetic information to future generations. The huge role DNA plays in the general health of a cell, and the viability of a cell to reproduce, makes DNA a primary biomolecule of interest in radiobiology.

1.2.2 Radiation effects on biomolecules

Due to its important role in the cell, DNA is currently considered the primary cellular target of radiation. This means that direct damage to DNA would result in the highest probability of cell death [9]. Other biomolecules show radiation-induced damage as well, such as chain breakage in carbohydrates, structural changes in proteins, and changes to the activity of enzymes [8]. The importance of these effects is currently not well understood, and other biomolecules are not considered the primary target of radiation. As such, most of the work done in radiobiology to date has been focused on DNA damage and chromosomal aberrations resulting from radiation.

Photon and electron radiation can affect the cell in two ways. When photons of sufficient energy enter biological media, photoelectric, Compton, and pair production processes (the likelihood of each process occurring depends on the incident photon energy) cause the release of high energy (few keV to MeV) electrons. If the photons or electrons interact directly with the critical cell targets (e.g. DNA strand), then the atoms in the target molecule may be ionized or excited, potentially causing damage directly to the biomolecule. This is called *direct action* of radiation [9]. More commonly, the photons can interact with other components of the cell (particularly water) to create long-lived species known as *free radicals*. Free radicals can diffuse long distances (on the order of tens of nanometers [10]) compared to the width of a

DNA strand (∼2 nm), and due to the presence of unpaired electrons can react with and damage the critical targets. This is called *indirect action* of radiation, and is the dominant source of damage from irradiation with photons and electrons (as opposed to irradiation with heavier particles such as protons, neutrons, or α-particles) [9].

The creation of free radicals from water occurs when the absorption of radiation by water molecules results in a water ion pair (H_2O^+, H_2O^-) by the reactions

$$\begin{aligned} H_2O &\rightarrow H_2O^+ + e^- \\ H_2O + e^- &\rightarrow H_2O^- \end{aligned} \tag{1.1}$$

The water ions are unstable and rapidly dissociate in the presence of other water molecules by the reactions

$$\begin{aligned} H_2O^+ &\rightarrow H^+ + OH^\bullet \\ H_2O^- &\rightarrow OH^- + H^\bullet \end{aligned} \tag{1.2}$$

forming an ion pair (H^+, OH^-) and the free radicals $H^\bullet$ and $OH^\bullet$. The ion pair will likely recombine to a water molecule, but free radicals have enough energy to diffuse distances great enough (i.e., greater than the diameter of the DNA helix) to react with target biomolecules. It is estimated that about two-thirds of all indirect cell damage is caused by the highly reactive $OH^\bullet$ free radical [8, 9].

Restricting the discussion to damage to DNA, a double-stranded helix can be subject to either a single-strand break (SSB) or a double-strand break (DSB), depending on the amount of energy deposited by charged particles and free radicals at the site of interaction. SSBs are characterized by damage to a single base-backbone section, and are often repaired by the cell using the opposite strand as the complementary template. DSBs, however, result in a complete snapping of the DNA molecule, and can

result in aberrations to an entire chromosome. There is a large body of work showing direct evidence of SSBs, DSBs, and both SSB and DSB repair of DNA in cells, using methods such as pulsed-field gel electrophoresis, single-cell electrophoresis, and gas-chromatography mass-spectrometry, the details of which will not be presented here [11–14].

Chromosomal damage resulting from one or more DSBs is the most immediately evident radiation effect in a cell, and is often visible with a high power microscope [9]. There has been significant work in this field, as the correct replication and splitting of the chromosomes during cell division will determine the ultimate health of the daughter cells. There are many different types of chromosomal aberrations, depending on the number of breaks in a chromosome or chromatid and depending on how the chromosome attempted to repair such breaks. Incorrect repairs can result in grossly disfigured chromosomes, or chromosomes that appear normal but are coded incorrectly. Many aberrations result in the inability of the cell to divide properly, thus killing the cell in a process termed *mitotic death*. Other aberrations cause the cell to undergo *apotosis*, a process of programmed cell death independent of division. Not all aberrations are lethal to the cell; some simply cause a mutation, which might turn out to be carcinogenic, but does not affect the successful reproduction of the cell. Current radiobiological models that characterize the radiation response of cell cultures and tissues are insensitive to the different types of cell death and mutations, and focus purely on cell survival. These models are discussed in the following section.

1.2.3 Radiation effects on cells and tissues

To quantify the effect of radiation on cells and tissues, a common approach is to generate a *cell survival curve*, which plots the *surviving fraction* of irradiated cells as a function of radiation *dose*. Dose is defined as the amount of energy absorbed by the sample per unit mass and is expressed in units of Gray (Gy), where 1 Gy = 1 Joule / kg [6]. The surviving fraction is determined by sparsely seeding a known

number of cells in a culture dish, irradiating the cells to a known dose, incubating the cells to allow exponential growth of each surviving cell into a single colony, and then counting the number of colonies and dividing by the number of cells originally seeded [9]. The surviving fraction is plotted on a log scale, with dose on a linear scale. The shape of a typical survival curve for mammalian cells is shown in figure 1.3a, which also displays the effect of the relative *radiosensitivity* of the irradiated cells or tissues. The more radiosensitive a certain type of cell or tissue, the less dose is required to achieve the same radiobiological *effect*. In the case of figure 1.3a, the effect is the surviving fraction of cells, but for tissues, organs, or tumors, the effect can be quantified differently (e.g., tumor control, normal tissue damage, etc...). For a variety of reasons not discussed here, tumor cells are generally more radiosensitive than healthy cells [8, 9]. This is one of the fundamental reasons why radiation therapy works for cancer treatment.

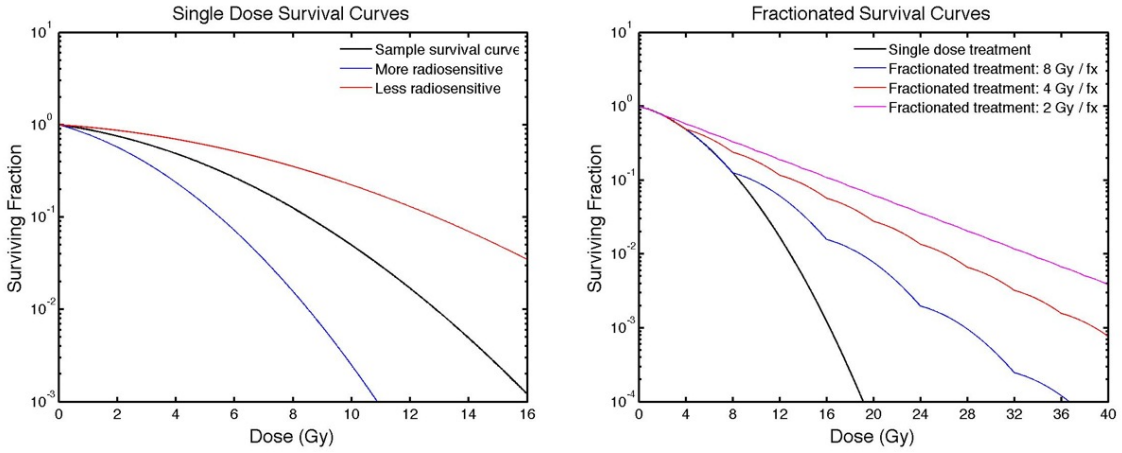

(a) (b)

Figure 1.3: (a) Single dose survival curves for mammalian cells with varying cell (or tissue) radiosensitivity and (b) fractionated dose survival curves (for constant radiosentitivity) with varying amounts of dose per fraction (fx).

The shape of the experimental cell survival curve (figure 1.3a) is characterized by an initial linear portion at low doses (typically < 2 Gy), meaning that the surviving fraction decreases exponentially with dose. This is followed by a downward curving

portion. At doses much higher than those delivered clinically in a single treatment the curve becomes linear again. The most accepted theoretical model for the shape of the survival curve is the *linear-quadratic* model. This model assumes that two components contribute to cell killing. The first component is proportional to dose, giving rise to the initial linear portion of the curve (i.e., surviving fraction decreases exponentially with dose). This component can be explained by lethal chromosomal aberrations (recall section 1.2.2) resulting from a single electron, as the probability of a single electron damaging a chromosome directly or indirectly is proportional to dose. The second component is quadratic with dose, giving rise to the downward curving portion of the curve. This component can be explained by lethal chromosomal aberrations resulting from two independently created electrons, as the probability of two electrons damaging the same chromosome is proportional to the square of the dose. Thus, the equation that governs the shape of the survival curve is

$$S = e^{-\alpha D - \beta D^2} \tag{1.3}$$

where S is the surviving fraction, D is the radiation dose, and α and β are constants that give the relative contributions of the linear and quadratic components, respectively. The drawback of this model is that the theoretical curve bends continuously downwards at high doses where the quadratic term dominates; this is contrary to experimental curves, which become linear at high doses. However, in the low dose region, which encompasses the clinical dose range for a single treatment, the model is an fairly accurate representation of experimental data.

In clinical radiotherapy, delivery of a single high dose to a tumor is very rare. Instead, the total treatment is divided into *fractions*, in which multiple low dose treatments are given, usually separated by $\sim$24 hours. There are significant advantages to fractionating a treatment. The delay between treatments allows healthy

tissues to both repair any non-lethal damage and repopulate any lethally damaged regions with new healthy cells. This is doubly beneficial as the rate of repair is typically higher in normal tissues than in cancerous tissues. The delay also allows tumor cells to progress to more radiosensitive phases of the cell cycle prior to the next treatment. Additionally, prolonging the treatment using low doses helps spare the patient from acute, early-onset side effects resulting from higher doses to healthy tissues. Ultimately, the total dose to the tumor can be significantly increased through fractionation, thus improving the probability of eradicating the tumor. The effect of fractionated treatment on the survival curve is shown in figure 1.3b, indicating that as the dose per fraction is decreased, the fractionated curve increasingly approximates a continuation of the initial linear component of the curve. The linear-quadratic model described above is very useful for fractionated treatment planning, once the prescribed total dose has been determined [9].

1.2.4 Current problems and questions in radiobiology

In theory, the linear-quadratic model discussed above could be used with experimental data to generate survival curves for various tissues, tumors, and organs, for the purposes of accurate treatment planning. However, it is very difficult to quantify a radiobiological effect for bulk tissues or organs *in vivo* (in the original organism). Most of the experimental data obtained to date has been collected *in vitro* (in the lab in a controlled environment), but it is quite difficult to obtain tissue samples directly from a patient that survive well enough in the lab to perform a radiation survival experiment. There has been limited success with *in situ* experiments, in which irradiated tumor cells are implanted into mice and the resulting tumor development is monitored. However, very few tissue and organ types are able to be successfully transplanted and analyzed using this technique [9]. Furthermore, it is difficult to relate radiobiological data obtained from cell cultures or non-human organisms to human radiation therapy patients [15]. As such, the models are unable to predict

the necessary minimum doses required for complete control of a given tumor. These prescribed doses are instead obtained from past clinical treatments by using population averages of a patient's radiation response (of healthy and cancerous tissues) to a given dose, for a given type of cancer [16].

One of the most troubling and elusive problems in modern radiotherapy and radiobiology is the variability in the clinical response to radiation treatment between patients. The level of normal tissue complications, and the curative response of the tumor, is dependent on the sensitivity of the patient to radiation. The prescribed tumor doses and normal tissue tolerances, obtained from the distribution of previous successfully treated patients, are not necessarily the optimum values for all patients. As such, there is considerable interest in developing a clinical *predictive assay*, in which individual patient radiosensitivity could be determined before treatment. With such an assay in place, the prescribed dose could be escalated for more resistant patients, and reduced for more sensitive patients, to optimize the curative outcome while minimizing the negative responses of normal tissues [17]. In recent years, a number of efforts have been made to correlate experimental radiosensitivities of cell samples obtained from patients with the clinically observed radiation response. However, these studies have had conflicting measures of success [18–21]. In addition to the need for a predictive assay, there is also no proven method in place for assessing the response of a patient during the course of an extended (i.e., fractionated) radiation treatment.

A further limitation to the radiobiological models presented here is that they are only sensitive to the *survival* of cells, and can give only limited information on what type of damage is causing cell death, or in what component or region of the cell the damage was caused. Limiting the investigation to cell survival alone is also insensitive to radiation induced mutations that may not be lethal to the cell itself. The primary radiobiological focus has been on DNA and chromosome damage, and the effect of

damage to other biomolecules, which are also vital to the health of the cell, has not been fully investigated. A major incentive to examine other cellular components is the relatively recent discovery of the *bystander effect*. First demonstrated in 1992 [22], it was seen that when a known fraction of cells in a culture is irradiated with low doses of α-particles, a higher fraction of cells show chromosomal damage than what was known to be irradiated. Many recent experiments have confirmed this effect. A common method is to use focused radiation microbeams, capable of irradiating only the nucleus of a single cell, to demonstrate that cells in the vicinity of the irradiated cell have higher incidences of mortality, mutation, and general damage [23]. Other experiments have harvested cells from an irradiated culture and transplanted them into a non-irradiated culture, subsequently observing the same damaging effects in the non-irradiated cells as in the irradiated cells, albeit to a lesser degree [24]. This is direct evidence of some passage of information, or toxic substance, from the damaged cells to the healthy cells, and indicates that the principal target of radiobiology is not restricted to DNA and chromosomes, which are restricted to the nucleus of the cell.

In light of these issues, there is a clear need for continued investigation of the interactions between ionizing radiation and human cells and tissues. The experimental modality used for such investigations should be sensitive to different types of biomolecules, and ideally should be able to localize any information obtained to physical structures within the cell. One technique that shows great promise for studying cellular processes is Raman microscopy.

1.3 Overview of modern biomedical Raman microscopy

The physical basis for the Raman effect is the inelastic scattering of a photon. The energy lost by the photon during "Stokes" Raman scattering (described in chapter 2) is transferred to a chemical bond or molecular group, exciting the bond or group into a vibrational energy state. The amount of energy lost is characteristic to the bond or

molecular group being excited. Therefore, the Stokes Raman scattered photon has a characteristic shift to a longer wavelength than that of the incident photon.

Raman microscopy (RM) focuses a laser through a microscope objective lens onto a sample. The laser induces vibrations in the various molecules of the sample and creates Raman scattered photons with frequencies and intensities characteristic to the properties of the molecules in the material being analyzed. The scattered Raman photons are collected and passed through a spectrometer, then collected on a charge-coupled device (CCD) camera for spectroscopic analysis. The resulting Raman spectrum provides a detailed description of the molecular composition within the sampling volume. The theory of RM will be presented in detail in chapter 2.

With aid from modern technological advances, RM has developed into an effective tool for application in the biological sciences. At sufficiently low laser powers and with correct choice of the laser wavelength, RM is non-invasive and non-destructive. This allows live cells and tissues to be analyzed without causing any damage or perturbation to the sample. Additionally, a high-power focusing objective combined with a precision motorized microscope stage can provide spatial resolutions on the order of 1 μm. This level of spatial discrimination allows the interior structure of a single human cell (typically 10-50 μm in diamter) to be resolved. Most importantly, RM is sensitive to many types of molecular structures and chemical bonds, enabling the analysis of all four types of biomolecules: proteins, lipids, carbohydrates, and nucleic acids.

The first successful application of RM for single-cell analysis was reported in 1990 [25]. One of the first biomedical applications of modern RM was to characterize and create spatial maps of the molecular composition of bacteria and other medically relevant microorganisms [26–29]. RM has been applied in similar fashion to single human tumor cells, and has been used successfully to map the distribution of protein and nucleic acids within the cytoplasm and nucleus [30–33]. Many studies have used

RM to characterize the spectral differences between normal and cancerous cells and tissues, or to distinguish between different types of tumor cells [34–40]. RM has also been used to investigate the spectral differences between living and dead tumor cells [41] and to monitor the spectral changes of tumor cells undergoing cell death via apoptosis [42].

Other Raman spectroscopy techniques, without the spatial discrimination of modern RM, have been applied to the field of radiobiology but have not yet been used to investigate the effects of radiation in single cells. Previously, Fourier-transform Raman spectroscopy has been used to investigate the radiation-induced spectral changes in isolated aqueous DNA [43]. However, achieving a measurable change in the spectra of isolated DNA using this modality requires very high doses (hundreds to thousands of Gray) which are well above the levels used in clinical radiation therapy and well above the levels known to cause over 99.9% mortality in a typical *in vitro* cell culture (figure 1.3). Raman spectroscopy has also been used to investigate the effect of proton irradiation on both healthy and cancerous human skin samples, and was successful in demonstrating increased sensitivity to protein damage in cancerous tissues [44]. Raman spectroscopy was also successful in measuring changes in protein levels in mice tissues after irradiation of the brain [45].

These previous studies suggest that RM could be a powerful tool for the investigation of radiation interactions with human cells and tissues. RM irradiation experiments could help address some of the radiobiological problems and questions discussed in section 1.2.4. Some attractive clinical applications of RM are the development of a predictive assay, and the development of a method to assess patient response during treatment. RM is also suitable for investigating radiobiological targets other than DNA and chromosomes; these investigations could help explain such phenomena as the bystander effect, and would be of great benefit to the development of future radiobiological models.

1.4 Thesis scope

The primary goal of this work is twofold: (1) to design, develop, and characterize a Raman microscope that is capable of investigating the structure and spectra of samples with physical dimensions comparable to those of a human cell, and (2) to develop protocols for suitable cell culture preparation prior to RM acquisition and fully characterize the pre-irradiation Raman spectra of the cell types which will be used for irradiation experiments. This work provides a foundation for future investigations of the interactions between ionizing radiation and human cells.

This work details the design and development of a RM system designed for investigation of human cells at high spatial resolution. For the initial development and qualitative characterization of the RM system, polystyrene microbeads (5 μm diameter spheres) dispersed on silicon are used as test samples. The microbeads are used to determine the optimum operating parameters of the system for RM of cells, an approach used successfully by other groups doing high resolution RM [46]. Once the optimum parameters are determined, quantitative measurements of the system's spatial and spectral resolution are performed using metallic nanostructures deposited on a flat silicon substrate. The initial results also include a detailed investigation and discussion of possible substrate materials suitable for RM of human cells. A variety of materials have been used with success by other groups, but not all are suitable or practical for use in radiobiological studies of human cell cultures.

The remainder of the results in this work present a detailed investigation into the Raman spectra of two types of human tumor cells. Before any radiation experiments can be performed, a detailed understanding of the Raman signals obtained from non-irradiated cells is required. Much of the work presented will address the issue of spectral variability between cells in the same culture, as this will have a significant impact on the methods developed for future experiments. To fully characterize the

cell spectra and correlate measured spectral features with optically observed morphological features, line profiles and full maps of selected cells are presented and compared with optical microscopy images. The results are discussed with respect to the development of future radiobiological RM experiments.

Chapter 2

Raman Spectroscopy

This chapter provides a theoretical and experimental overview of Raman spectroscopy and Raman microscopy (RM). A brief history of the development of Raman spectroscopy is presented (section 2.1), followed by a theoretical description of Raman scattering and molecular vibrations (section 2.2). The necessary theoretical and experimental details pertaining to the practical application of Raman spectroscopy (section 2.3) and RM (section 2.4) are outlined. Some important considerations that arise when performing RM on biological materials such as cells and tissues are discussed (section 2.5). The chapter concludes with a general discussion of the advantages and disadvantages of Raman spectroscopy (section 2.6) and a brief overview of some of the more prevalent modern applications (section 2.7).

2.1 History

The initial theory for the inelastic scattering of optical wavelengths, now known as the Raman effect, was published in 1923 by A. Smekal [47]. The effect was first observed experimentally in 1928 by C. V. Raman and K. S. Krishnan [48]. Raman and Krishnan used a telescope and a series of optical filters which allowed them to isolate blue light from the sun, focus it onto a transparent liquid sample of carbon tetrachloride, and observe scattered green light [49]. Shortly after this experiment a mercury lamp was substituted as the incident light source and the apparatus was

used to measure the scattered Raman spectrum of benzene [50]. This was the first molecule to be analyzed in detail using Raman spectroscopy.

Following Raman's discovery many efforts were made to improve the excitation source. Various types of lamps were implemented, using elements such as helium, bismuth, lead, zinc, and mercury; mercury lamps proved the most effective due to their high intensity [51–53]. The development and improvement of mercury lamps for Raman excitation continued until the introduction of lasers in 1962 [54]. Lasers proved to be excellent Raman excitation sources and are still used in modern Raman applications due to their high power, ease of collimation and focusing, excellent monochromaticity, and availability in a number of wavelengths from the ultra-violet (UV) to the infrared (IR).

A similar technological evolution occurred in the improvement of detection methods for Raman scattered light. Early measurements were performed using photographic plates, but the need for long integration times and photographic plate development made this a highly inefficient method. The first photoelectric Raman systems were developed in the 1940's and 1950's using photomultiplier tubes for light collection [55, 56]. However, obtaining a Raman spectrum with a single detector is time-consuming since the user must scan the desired frequency range and collect signal at each point. Multi-channel detection using photo-diode arrays was introduced in the early 1980's [57, 58], and was followed shortly after by detection using charge-coupled device (CCD) arrays [59, 60]. CCDs are still the detectors of choice for modern systems due to their low readout noise, high efficiency, and excellent sensitivity over a wide range of wavelengths.

The advancement of Raman spectroscopy has also been aided by technological improvements in diffraction gratings, monochromators and spectrometers, optical filters, and many other components. There are many types of Raman spectroscopy currently being performed, including Fourier transform (FT) Raman spectroscopy,

surface enhanced Raman spectroscopy (SERS), fiber-optic Raman spectroscopy, and UV resonance Raman spectroscopy (UVRRS). Each Raman variant has its own advantages and disadvantages, depending on the sample being analyzed, but all are being used with great success in a variety of scientific disciplines and industrial applications.

2.2 Theory of Raman scattering

2.2.1 Origin of the Raman effect

If a molecule is irradiated with optical photons of frequency v_0 and energy hv_0, where h is Planck's constant, most of the the light is elastically scattered with no frequency shift (Rayleigh scattering). However, approximately one in every 10^6 photons [61] is inelastically scattered with frequency $v^{'} = v_0 \pm v_m$ (Raman scattering), where v_m is the frequency of a vibrational energy state (m = 0, 1, 2,...) of the molecule. The $v_0 - v_m$ frequency shift is known as *Stokes* scattering and occurs when the scattered photon loses energy to a vibrational state, whereas the $v_0 + v_m$ shift is known as *anti-Stokes* scattering and occurs when the scattered photon gains energy from an existing vibrational state (figure 2.1).

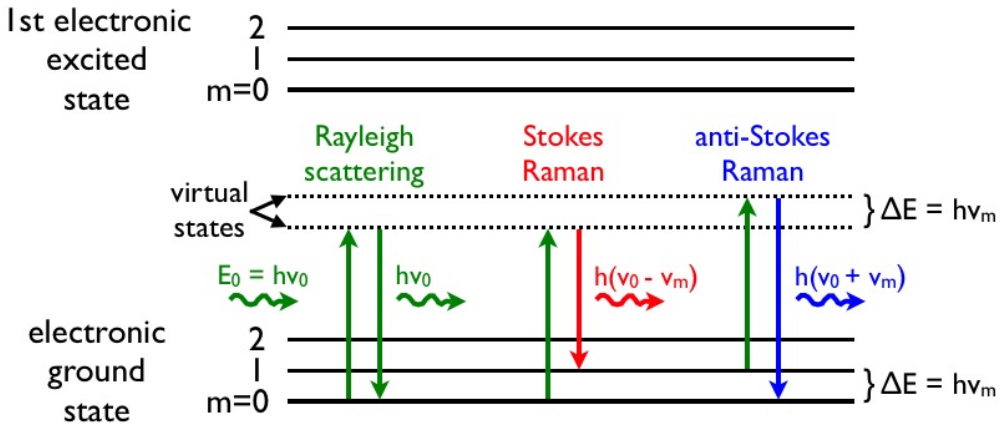

Figure 2.1: Energy level diagram for a molecule irradiated with optical photons of frequency v_0 subject to either elastic Rayleigh scattering, or inelastic Stokes or anti-Stokes Raman scattering.

In most Raman spectroscopy applications, the energy of the incident photons is chosen to be less than the energy of the first electronic excited state of the molecule. The molecule is excited from its ground state to a virtual excited state, which yields a distorted electron distribution that is highly unstable and decays almost immediately to either the original state, in the case of Rayleigh scattering, or an excited vibrational energy state, in the case of Stokes Raman scattering.

The existence of Raman scattering from a molecule can be derived using a classical model in which the exciting laser source is expressed as an electric field vector $\mathbf{E}$ with frequency v_0, oscillating with time as

$$\mathbf{E} = \mathbf{E_0} \cos 2\pi v_0 t \tag{2.1}$$

where $\mathbf{E}_0 = (E_{0x}, E_{0y}, E_{0z})$ is the maximum electric field amplitude.

If a molecule is placed in the electric field of equation 2.1, the field will induce a charge separation within the molecule and create an electric dipole moment $\mathbf{P}$ given by

$$\mathbf{P} = \alpha \mathbf{E} \tag{2.2}$$

where the proportionality constant α is called the *polarizability* of the molecule. Expressed in matrix form with cartesian coordinates, α becomes a 3×3 polarizability tensor and equation 2.2 takes the form

$$\begin{bmatrix} P_x \\ P_y \\ P_z \end{bmatrix} = \begin{bmatrix} \alpha_{xx} & \alpha_{xy} & \alpha_{xz} \\ \alpha_{yx} & \alpha_{yy} & \alpha_{yz} \\ \alpha_{zx} & \alpha_{zy} & \alpha_{zz} \end{bmatrix} \begin{bmatrix} E_x \\ E_y \\ E_z \end{bmatrix} \tag{2.3}$$

The polarizability tensor is symmetric for normal Raman scattering, and the molecular vibration will yield Raman scattered photons if any one of the polarizability tensor's components is changed during the vibration [62], as shown below.

If the induced molecular charge separation from the electric field causes vibrations of the atomic nuclei with frequency v_m, then the displacement from the equilibrium position of the ith nucleus, q_i, is written as

$$q_i = q_{i0} \cos 2\pi v_m t \tag{2.4}$$

where q_{i0} is the vibrational amplitude of the ith nucleus. For small amplitude vibrations the polarizability α is linear with q_i and can be expanded about the nuclear equilibrium position as

$$\alpha = \alpha_0 + \left(\frac{\delta\alpha}{\delta q_i}\right)_0 q_i + \ldots \tag{2.5}$$

where α_0 is the equilibrium polarizability, and $(\delta\alpha/\delta q_i)_0$ is the rate of change of α with respect to q_i, evaluated at the equilibrium position.

If equations 2.1 and 2.5 are substituted into equation 2.2, the induced dipole moment becomes

$$\begin{aligned} \mathbf{P} &= \alpha \mathbf{E_0} \cos 2\pi v_0 t \\ &= \alpha_0 \mathbf{E_0} \cos 2\pi v_0 t + \left(\frac{\delta\alpha}{\delta q_i}\right)_0 q_i \mathbf{E_0} \cos 2\pi v_0 t \end{aligned} \tag{2.6}$$

and using equation 2.4 for q_i, equation 2.6 becomes

$$\mathbf{P} = \alpha_0 \mathbf{E_0} \cos 2\pi v_0 t + \left(\frac{\delta\alpha}{\delta q_i}\right)_0 q_{i0} \mathbf{E_0} \cos(2\pi v_0 t) \cos(2\pi v_m t) \tag{2.7}$$

Finally, making use of the trigonometric identity $2\cos x \cos y = \cos(x-y)+\cos(x+y)$, equation 2.7 becomes

$$\mathbf{P} = \alpha_0 \mathbf{E_0} \cos 2\pi v_0 t + \frac{1}{2}\left(\frac{\delta\alpha}{\delta q_i}\right)_0 q_{i0} \mathbf{E_0} [\cos\{2\pi(v_0 - v_m)t\} + \cos\{2\pi(v_0 + v_m)t\}] \tag{2.8}$$

Classical electrodynamics predicts that the first term in equation 2.8 describes

an oscillating dipole that radiates light of frequency v_0, corresponding to Rayleigh scattering. Likewise, the second term describes the radiation of frequencies $v_0 - v_m$, corresponding to Stokes Raman scattering, and $v_0 + v_m$, corresponding to anti-Stokes Raman scattering. However, if $(\delta\alpha/\delta q_i)_0$ is zero (i.e., the polarizability tensor (equation 2.3) is unchanged with displacement of the nuclei) the molecular vibration will not be *Raman-active* and will not produce any Raman scattering. A discussion of Raman-active and Raman-inactive vibrations is provided in section 2.2.2.

A misleading aspect of equation 2.8 is that it predicts equal intensity of Stokes $(v_0 - v_m)$ and anti-Stokes $(v_0 + v_m)$ scattering. Experimental observations show that Stokes scattering is the dominant process. This is explained by the relative population of the vibrational states depicted in figure 2.1. The population ratio of the first excited vibrational state (m=1) to the ground state (m=0) is determined by the Maxwell-Boltzmann distribution

$$\frac{P_{m=1}}{P_{m=0}} = e^{-\Delta E/kT} \tag{2.9}$$

where ΔE is the change in energy between the two states, k is Boltzmann's constant, and T is the absolute temperature. Therefore as the temperature increases or the energy gap between $m = 0$ and $m = 1$ decreases, the fraction of molecules in the higher vibrational energy state increases, leading to a larger anti-Stokes effect. However, for most molecules and bond types at room temperature the population is almost entirely in the ground vibrational state, leading to a much stronger Stokes contribution [62]. Most Raman applications, with the exception of coherent anti-Stokes Raman spectroscopy (CARS), exclusively measure Stokes scattering; likewise in this work the anti-Stokes contributions will not be considered.

An expression for the absolute intensity of Raman scattering is difficult to derive, and the details are presented elsewhere [62, 63]. However, a basic expression for the

intensity of Stokes scattered radiation arising from a transition from a vibrational state m to a vibrational state n of higher energy is given by

$$I_{mn} = C \cdot I_0 \cdot (v_0 - v_{mn})^4 \cdot \alpha_{mn}^2 \tag{2.10}$$

where C is a constant, I_0 is the incident laser intensity, v_{mn} is the frequency difference between vibrational states m and n, and α_{mn} is the change in polarizability resulting from the molecular transition from state m to a virtual excited state and then to state n. The magnitude of the polarizability term α_{mn} determines the relative Raman scattering intensity for the given transition. However, the most important aspect of equation 2.10 for the experimental Raman spectroscopist is that the scattered intensity is proportional both to the incident laser intensity, and to the fourth power of the frequency of the scattered Raman radiation, $v_0 - v_{mn}$. Since the incident laser frequency is adjustable and the frequency differences between vibrational states remain constant (a property of the molecule), the scattered intensity is essentially proportional to the fourth power of the incident laser frequency, v_0. Therefore, a high-power, high-frequency laser is desirable for increasing the intensity of Raman scattering.

2.2.2 Molecular vibrations and Raman activity

The vibration of a polyatomic molecule can be very complicated. However, any vibration can be broken down into an orthogonal set of *normal mode* vibrations which oscillate independent of each other, and usually with a unique frequency. A complicated vibration pattern can be expressed as a superposition of the normal mode vibrations, and it is these normal mode frequencies which are detected by a Raman spectroscopy instrument. The number of normal modes depends on both the number of atoms in the molecule and the geometry of the molecule.

Each normal mode is a unique vibrational *degree of freedom* (DOF) for the

molecule. An N-atom molecule will have $3N$ DOF of motion, since any atom can move in any of the three independent directions x, y, and z. However, $3N$ includes three translational DOF for the molecule as a single unit, and three rotational DOF about the principal axes running through the molecule's centre of mass. For a linear molecule, there is no rotation about the molecular axis, so there are only two rotational DOF. As such, the number of normal mode vibrations becomes $3N - 6$ for an arbitrary molecule, and $3N - 5$ for a linear molecule. Carbon dioxide (CO_2), for example, is a linear triatomic molecule, and therefore has $3 \times 3 - 5 = 4$ normal mode vibrations.

It is common practice in vibrational spectroscopy to assign descriptive names to the various types of normal mode vibrations. As an example, the normal mode vibrations of CO_2 consist of one *symmetric stretching* mode (figure 2.2a), two *bending* or *deformation* modes (figure 2.2b), and one *antisymmetric stretching* mode (figure 2.2c). The only difference between the two bending modes (figure 2.2b) is that their planes of oscillation are perpendicular to each other. As such the two modes have the same vibrational frequency, and are called doubly degenerate modes.

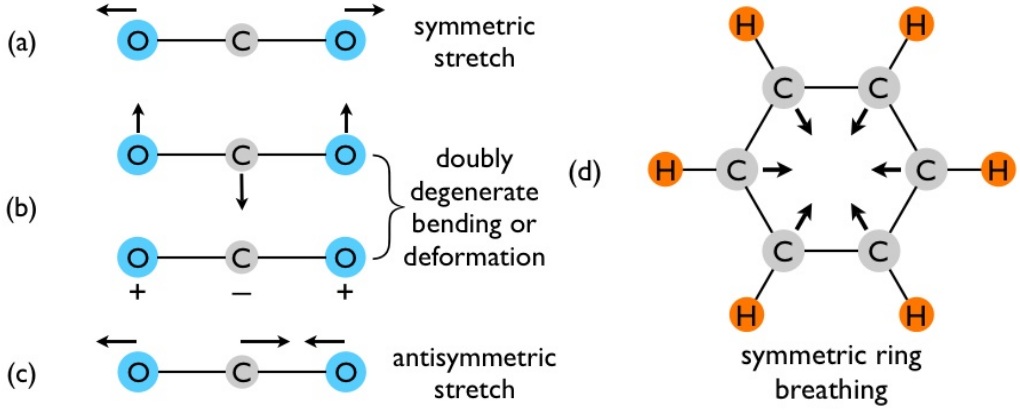

Figure 2.2: (a)-(c) Normal mode vibrations of the CO_2 molecule (O=C=O). In (b), + and − indicate motion in and out of the page, respectively. (d) Symmetric ring breathing of benzene (C_6H_6).

For more complicated molecules (i.e., $N > 3$), the normal modes become increasingly complex as well. However, a simple example of a large N molecule normal mode

is the *ring breathing* mode of an aromatic ring, such as the one in benzene (C_6H_6) (figure 2.2d). Aromatic ring breathing modes typically yield intense Raman scattering and are therefore easily observed in chemical and biological Raman applications.

Not all normal mode vibrations will produce Raman scattered photons. As discussed in section 2.2.1, a vibration will only be Raman-active if there is a change in the polarizability, α, with a small nuclear displacement from the equilibrium position (equation 2.8). As an example, consider the normal mode vibrations of CO_2. Due to the molecular geometry, the polarizability is not the same in all directions from the centre of mass of the molecule. For CO_2, the electrons are most polarizable (highest α) along the molecular axis, and are least polarizable perpendicular to the molecular axis. Plotting $1/\sqrt{\alpha}$ (by convention [62]) in all directions from the centre of mass of the molecule creates a *polarizability ellipsoid*. If the size, shape, or orientation of the ellipsoid is changing at the equilibrium position during the normal mode vibration, then the vibration will be Raman-active. The changes of the polarizability ellipsoid for the three types of vibrations of CO_2 are depicted in figure 2.3.

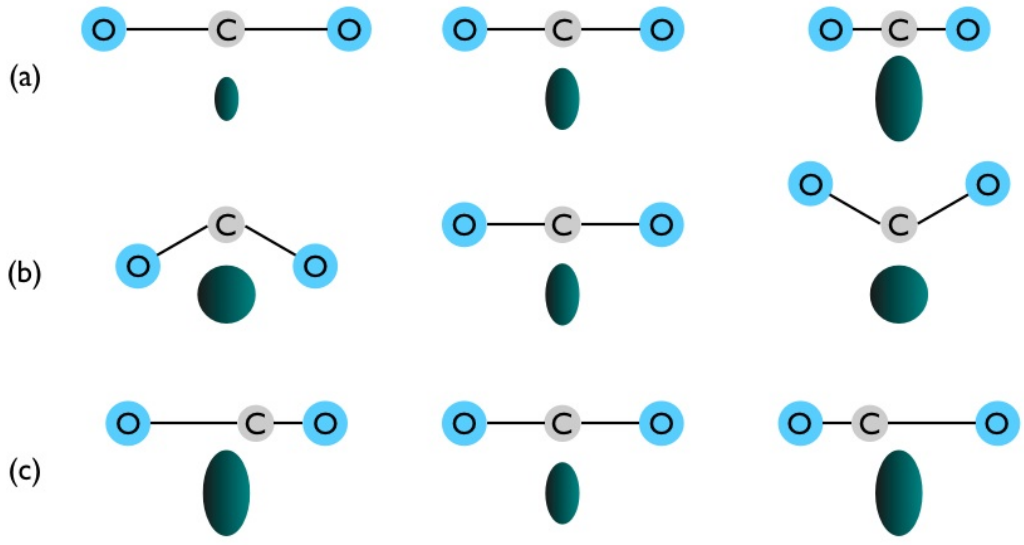

Figure 2.3: Changes in polarizability ellipsoids during normal mode vibrations of CO_2: (a) symmetric stretch is Raman-active, (b) bending or deformation is Raman-inactive, and (c) antisymmetric stretch is Raman-inactive.

The symmetric stretching mode of CO_2 (figure 2.3a) is Raman-active, as the size of the polarizability ellipsoid is changing at the equilibrium position (getting larger or smaller); therefore $(\delta\alpha/\delta q_i)_0 \neq 0$. The bending or deformation mode (figure 2.3b), however, is Raman-inactive because the shape of the ellipsoid is the same at each of the vibrational extremes. Therefore, considering only small displacements at the equilibrium, $(\delta\alpha/\delta q_i)_0 = 0$. For the antisymmetric stretching mode (figure 2.3c), even though the size of the ellipsoid changes, the vibration is Raman-inactive for the same reason as for the bending or deformation mode.

Although useful for simple molecules, this method of determining Raman-activity by inspection of the normal modes is difficult to apply to large or complex molecules. A more rigorous approach requires the application of group theory and quantum chemistry, which leads to a set of *selection rules* that determine whether a given vibration will be Raman-active or not. The details and derivations of these rules are beyond the scope of this thesis and are presented elsewhere [62, 64, 65].

2.3 Raman spectroscopy instrumentation

2.3.1 Raman shift

When measuring frequencies of the Raman scattered light, it is a universal convention to record the *wavenumber*, $\bar{v}$, rather than the frequency, v. The wavenumber is the reciprocal of the wavelength, and is commonly expressed in units of cm^{-1}. Since in Raman spectroscopy it is the *change* in wavenumber from that of the excitation source that is of interest, the measured Raman signal is expressed as a *Raman shift*, given by

$$\text{Raman shift} = \frac{1}{\lambda_0} - \frac{1}{\lambda} = \frac{v_0}{c} - \frac{v}{c} = \bar{v_0} - \bar{v} \quad (\text{cm}^{-1}) \tag{2.11}$$

where λ_0, v_0, and $\bar{v_0}$ correspond to the incident light and λ, v, and $\bar{v}$ correspond to the Raman scattered light. Since $\Delta E = h\Delta v$, equation 2.11 shows that the Raman shift is proportional to the change in energy between the incident and Raman scattered light,

and is thus proportional to the vibrational energy of the molecule. When creating a Raman spectrum, the Raman scattered light is dispersed by a spectrometer and captured on a CCD, and the measured intensities are plotted against the Raman shift in wavenumbers.

2.3.2 Raman spectroscopy apparatus

The basic equipment and set-up of a typical Raman spectroscopy apparatus is shown in figure 2.4. The laser beam irradiates the sample and the Raman scattered light is collected and collimated by an objective lens. The Raman light is focused into a spectrometer which disperses the light and focuses it onto a CCD detector. The details of light dispersion in the spectrometer and light collection at the CCD are discussed in sections 2.3.3 and 2.3.4, respectively.

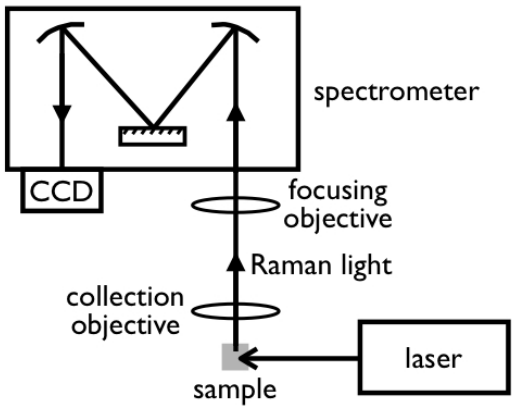

Figure 2.4: General schematic of the light path for a typical Raman spectroscopy system.

2.3.3 Light dispersion

Once the Raman scattered light has been collected from the sample, the different scattered wavenumbers must be separated to record the full spectrum of information. In most modern Raman spectroscopy systems, this is done using a dispersive spectrometer with a diffraction grating. There are many different spectrometer designs in use, depending on the excitation wavelength and the type of Raman spectroscopy being performed. The Czerny-Turner spectrometer shown in figure 2.5 is a common design,

and is the spectrometer used in this work. The Raman collected light, composed of a variety of wavelengths, is passed through the entrance slit of the spectrometer and is reflected off a curved collimating mirror onto a diffraction grating. The diffraction grating reflects the light at different angles depending on the wavelength, and the dispersed light is focused onto the exit focal plane by another curved mirror.

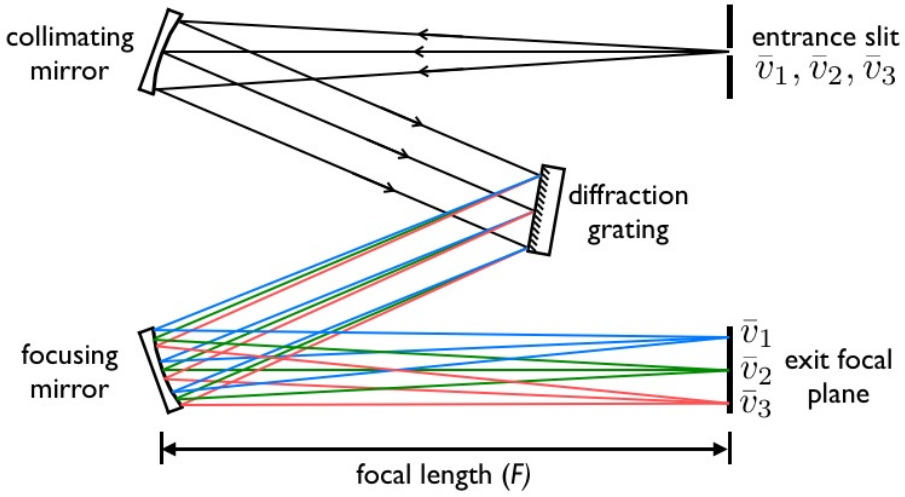

Figure 2.5: Design of a Czerny-Turner dispersive spectrometer. Light rays composed of a mixture of wavenumbers are dispersed by a diffraction grating and focused onto the exit focal plane.

The extent to which the light is spread across the exit focal plane of a spectrometer is described by the *reciprocal linear dispersion*, defined as the range of wavelengths or wavenumbers contained within a unit length of the focal plane. Reciprocal linear dispersion is commonly expressed in units of nm/mm if using wavelength, or cm^{-1}/mm if using wavenumber. In terms of wavelength, the reciprocal linear dispersion is given by

$$\frac{d\lambda}{dx} = \frac{10^6 \cdot \cos\theta}{n \cdot g \cdot F} \tag{2.12}$$

where n is the diffraction order, g is the groove density of the grating in grooves per mm (g/mm), F is the exit focal length of the spectrometer in mm, and θ is the angle of the diffracted light leaving the grating [66]. Equation 2.12 can be expressed in

terms of wavenumber by using

$$\frac{d\lambda}{dx} = \frac{d(1/\bar{v})}{dx} = \frac{-1}{\bar{v}^2} \cdot \frac{d\bar{v}}{dx} \tag{2.13}$$

and therefore

$$\frac{d\bar{v}}{dx} = -\bar{v}^2 \cdot \frac{d\lambda}{dx} = -\frac{10^6 \cdot \cos\theta \cdot \bar{v}^2}{n \cdot g \cdot F} \tag{2.14}$$

Therefore, the reciprocal linear dispersion in $\mathrm{cm}^{-1}/\mathrm{mm}$ varies with the square of the wavenumber of the scattered Raman light, which leads to a non-linear relationship between wavenumber and unit length at the focal plane.

An instrument with a higher *linear dispersion* (or conversely a lower reciprocal linear dispersion $d\bar{v}/dx$) will spread a given wavenumber range over a greater length of the focal plane, and will therefore more easily resolve fine spectral details. Such an instrument will therefore have better *spectral resolution* than an instrument with low linear dispersion (high $d\bar{v}/dx$). A definition for the spectral resolution of a Raman system, and the procedure required to determine its value, is presented in chapter 3.

In all Raman systems there is a practical limitation to the size of the focal plane. Therefore, there is a limited wavenumber range, or *spectral window*, that can be measured in a single acquisition. The size of the spectral window can be increased at the expense of the linear dispersion by decreasing either the grating groove density g or the focal length F (equations 2.12 and 2.14), but this is generally undesirable due to the decreased ability to resolve spectral details. The most common technique used to avoid this limitation is to select for a desired spectral window by rotating the diffraction grating such that only the diffracted light from the desired window is incident on the focal plane of the spectrometer. This method requires the collection of multiple spectra at different grating angles to cover a larger wavenumber range, but does not sacrifice the spectral resolution of the system.

2.3.4 Light detection

The current method for detecting the dispersed light output from the spectrometer is to use a charge-coupled device (CCD). CCDs are two-dimensional (2D) optical arrays of photosensitive diodes, usually composed of a silicon-metal-oxide semiconductor [59, 60]. Small metal pads are deposited on each photosensitive "pixel" (array element) and kept at a positive potential; each is connected via a diode to a grid circuit that defines the CCD array dimensions. When photons are incident on a photosensitive element, photoelectrons are produced and are attracted to the nearest metal pad. The number of photoelectrons collected at the pad is therefore proportional to both the intensity of the incoming light and the acquisition time, the amount of time the photosensitive element is exposed. After each acquisition, the charge collected (i.e. the accumulation of photoelectrons) at each pad is read out pixel-by-pixel by sequentially shifting the charges from one row (or column) to the next as the charges from the row (or column) at the edge of the array are read out. The charge measured at each pixel is converted to an analog voltage, passed through an amplifier, and digitized by an analog-to-digital converter. The digital output allows a 2D image to be created where each pixel value is proportional to the light intensity incident on the corresponding CCD element.

In modern Raman spectroscopy systems, a CCD array is placed at the focal plane of the spectrometer (figure 2.5) such that one axis of the CCD (usually the long axis, if there is one) is parallel with the direction of linear dispersion. A typical arrangement is depicted in figure 2.6, using the three wavenumbers $\bar{v}_1$, $\bar{v}_2$, and $\bar{v}_3$ shown in figure 2.5. In most modern systems the height of the dispersed focal spot on the CCD, in the direction perpendicular to the dispersion axis, is greater than the dimensions of a single pixel. This is illustrated in figure 2.6, where each wavenumber, represented by a single distinct color, is incident on six vertical pixels in each column. To generate a Raman spectrum of maximum signal intensity, the signal from the six pixels in each

column are summated, or "binned", into a single measurement of intensity for that wavenumber.

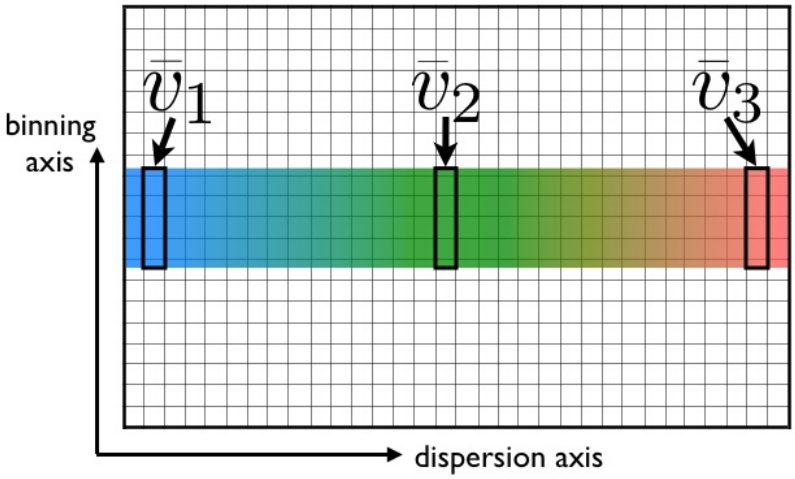

Figure 2.6: The arrangement of a CCD detector array placed at the focal plane of the spectrometer shown in figure 2.5, showing the alignment of the dispersion and binning axes with the CCD grid.

There are two primary sources of CCD noise that contribute to the measured signal. Heat produces electrons in the photosensitive element that are indistinguishable from the photoelectrons produced by incident light, thus creating *thermal noise*, or *dark current*. Thermal noise can be very problematic for long acquisition times, but can generally be reduced to a negligible level by cooling the CCD detector to temperatures well below freezing (e.g. -60 °C to -120 °C). Reading out the collected charges from the CCD also contributes noise as a result of electrons produced while shifting charges from pixel-to-pixel and noise introduced during amplification and digitization. This *readout noise* is independent of acquisition time, and for most Raman applications the signals detected are of much higher intensity than the readout noise level. Readout noise is generally much stronger than thermal noise for sufficiently cooled modern Raman systems, and can become problematic if the Raman signals are very weak. If necessary, post-processing techniques such as averaging and smoothing can be applied to reduce CCD noise.

2.4 Raman microscopy instrumentation

The most important difference between Raman microscopy (RM) and conventional Raman spectroscopy is the addition of a very high degree of spatial localization of the Raman signal. In practice, however, this is rather difficult, as the dimensions of the sample can be as small as a few microns across and less than a micron thick. The weakness of the Raman signal requires the use of a high-powered microscope objective to focus the incident laser beam to a very small spot in order to ensure efficient production and collection of the Raman signal. In addition, to properly localize the point of Raman collection, a precisely controlled microscope stage with micron-scale stepping resolution must be used. The objective and the microscope stage are the two most important features that separate RM from conventional Raman spectroscopy.

Most RM systems couple the excitation laser into an upright microscope and collect the Raman scattered photons with the same objective that focuses the laser onto the sample in a 180° *backscatter* orientation (figure 2.7). This geometry is the most efficient method of Raman collection for thin, solid samples, as it minimizes the loss of signal due to attenuation in the sample or substrate. It also allows the use of high-power objectives which must be brought very close to the sample for proper focus. In this geometry, the Raman and Rayleigh backscattered light follow the same beam path as the incident laser. Optical filters remove the Rayleigh scattered light and pass the Raman scattered light to the spectrometer (figure 2.7).

Correct microscope objective choice is essential for RM. Modern objectives used in most RM systems are *infinity-corrected* so that a perfectly collimated light source (i.e. an ideal laser, focused at infinity) incident on the back aperture of the objective will be focused to a diffraction limited spot. The dimensions of the focused laser spot greatly affect the collection efficiency and spatial resolution of the system, and depend on the characteristics of both the incident laser and the objective.

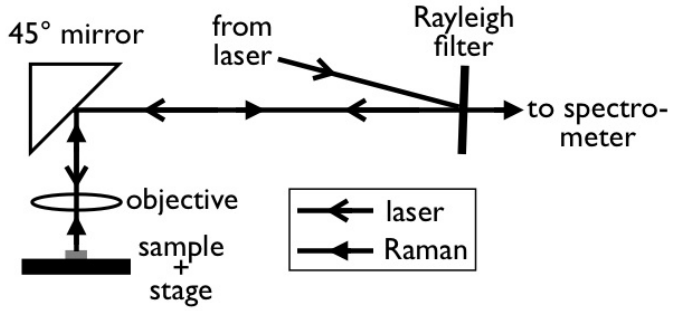

Figure 2.7: General schematic of the light path for a typical RM system using 180° backscatter collection geometry.

The most important specification of an objective for RM is the *numerical aperture* (NA), which is defined as

$$\mathrm{NA} = n \cdot \sin \alpha \tag{2.15}$$

where n is the refractive index of the immersion medium (1.00 for air, 1.33 for water, ∼1.5 for oil), and α is the half-angle of the maximum light cone collected by the objective (figure 2.8). Since $\alpha_{max} = 90°$, NA is always < 1 for dry objectives (no immersion). The NA of an objective determines its collection efficiency. Raman

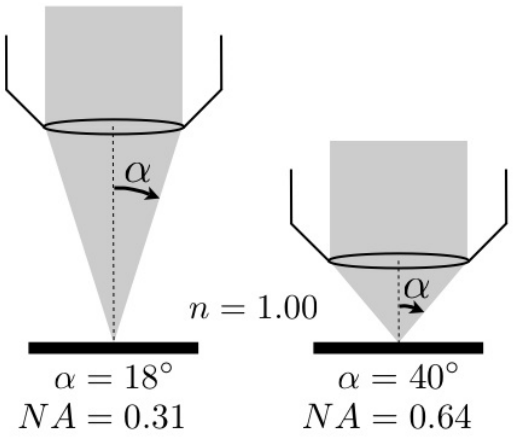

Figure 2.8: Example of numerical apertures (NA) calculated for two microscope objectives, using equation 2.15, in air ($n = 1.00$).

scattering is isotropic, and therefore the collection efficiency can be determined from

the solid angle Ω intercepted by the objective, given by

$$\Omega = 2\pi(1 - \cos\alpha) \tag{2.16}$$

Since the maximum value for α is 90°, the maximum solid angle Ω is 2π, resulting in a maximum efficiency of 50% ($2\pi/4\pi$, where 4π is the solid angle subtended by a complete sphere). A higher NA objective will be more efficient at collecting Raman scattering but will also excite a smaller volume of the sample (as shown below). Therefore, optimizing the signal strength will depend on both the objective and the state of the sample. A higher magnification objective will likely have a higher NA, but some manufacturers offer wide-field, low magnification objectives with high NAs as well.

The minimum width of the focused laser spot s (also referred to as the *beam waist*) depends on the NA of the focusing objective and the laser wavelength, and can be approximated using the formula [67]

$$s = \frac{0.61 \cdot \lambda}{\mathrm{NA}} \tag{2.17}$$

The height of the laser spot along the beam axis is often called the depth-of-focus (DOF), and is rather arbitrary since it depends on the choice of where the laser transitions from focused to defocused. Nevertheless, for high NA objectives a good approximation for the DOF is given by

$$DOF = \frac{n \cdot \lambda}{\mathrm{NA}^2} \tag{2.18}$$

Equations 2.17 and 2.18 are working formulas derived using wave optics [67], and are only valid for perfectly collimated lasers that are perfectly aligned with the back aperture of a high NA objective. This scenario is never achieved in practice due

to laser beam divergence or optical misalignments, but the formulas are useful to demonstrate how the choice of microscope objective affects the size of the Raman excitation and collection volume. Maximum spatial resolution will be achieved with the smallest possible focused spot, and therefore will be achieved using a high NA objective and a short wavelength laser.

Another important aspect of a RM system is *confocal* discrimination. The term confocal refers to the principle axis of an imaging system, which for RM is the axis along which both the incident laser and the collected signal traverse (recall figure 2.7). Confocal microscopy involves placing a small spatial aperture (such as a pin-hole) at the focus of any conjugate image plane on the principle axis, somewhere after the signal has been collected but before the signal is recorded (figure 2.9). In RM the *confocal aperture* is usually placed after the Rayleigh filter and before the spectrometer. The confocal aperture serves to reject signals originating from an out-of-focus or off-axis region of the sample or RM system. Such unwanted signals could be stray light, scattered signals from outside the focal volume, or signals from a sample substrate. A smaller confocal aperture will increase the confocal resolution (i.e. the depth selectivity in the sample) and reduce unwanted signals, but if the aperture is too small it can decrease the amount of Raman signal collected from the desired target. Modern RM systems employ confocal apertures ranging from 10-200 μm in diameter.

2.5 Raman microscopy of biological materials

A number of considerations pertaining to RM of cells and tissues must be addressed. The most important considerations are the choice of laser wavelength and power, the spatial and confocal resolution requirements, the spectral resolution requirements and spectral window(s) of interest, and the choice of substrate material.

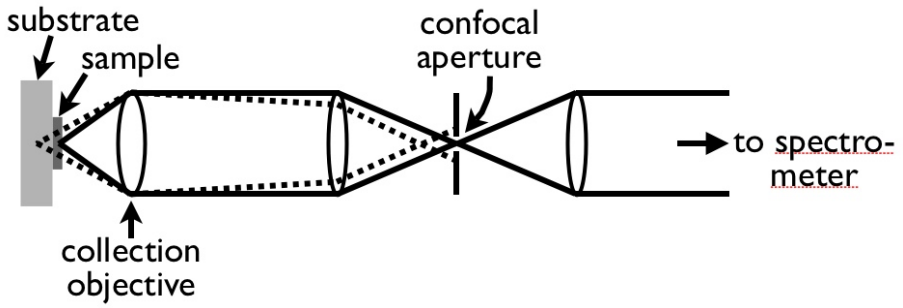

Figure 2.9: Principle of confocal Raman microscopy. Signals originating from an out-of-focus or off-axis position such as a substrate (dotted rays) are rejected by the confocal aperture, whereas signals from the desired sampling volume (solid rays) pass through the aperture to the spectrometer.

2.5.1 Laser wavelength and laser power

The choice of laser wavelength and power is vital when performing RM analysis of cells. A higher laser power yields a higher laser intensity at the sample and, recalling section 2.2.1, equation 2.10, the intensity of Raman scattering is proportional to both the intensity of the laser and the fourth power of the laser frequency. Therefore, a high power, short wavelength laser will generate the strongest Raman scattering effect. However, two factors that mediate the choice of wavelength and power are biological fluorescence and laser-induced damage to the cell.

Biological fluorescence, which can mask weak Raman signals, is reduced as the wavelength of the laser is increased [62, 68]. The least amount of fluorescence induced by laser light in the visible spectrum occurs for near-infrared wavelengths (i.e., > 700 nm). The reduction in fluorescence at these wavelengths comes with an undesirable reduction in Raman scattering intensity compared to shorter wavelengths (i.e., 450 - 650 nm), but allows for longer acquisition times and the detection of weaker Raman signals.

Damage to the cell induced by the laser can be determined experimentally by observing a changing Raman signal as a function of irradiation time. Several studies have shown that for short visible wavelengths such as 488 nm and 514 nm, damage to

the cells and chromosomes is observed after only a few minutes for laser powers at the sample of < 10 mW [69–71]. This effect was attributed to photochemical reactions [69], as the powers used are much to low to induce any sample heating. The same effect is not observed for 660 nm, where cells were reported to survive up to 20 minutes at 25 mW laser power. However, it has been shown that even longer wavelengths allow the use of much higher powers and longer acquisition times, as cells examined at 785 nm exhibit no spectral changes even after 40 minutes at 115 mW laser power [70]. Cells have also been analyzed at 830 nm at powers greater than 100 mW for 20 seconds [36]. These results have shown that the best laser wavelength range available for single cell RM applications is 785 - 830 nm, which is also a desirable wavelength range for the reduction of biological fluorescence. It should also be noted that the power density at the sample is an important consideration, and local damage to the sample from heat may be caused if the power density is too high.

2.5.2 Spatial, confocal, and spectral requirements

The spatial and confocal requirements of the RM system are determined by the cell dimensions. Depending on the type of cell and the growth conditions, *adherent* cells (i.e. cells attached to a substrate) are typically 10-50 μm in diameter and 1-5 μm thick. Therefore, to investigate the interior structure of a cell the spatial resolution of the RM system must be on the order of 1 μm. Adherent cells are usually "splayed out" on the substrate, and therefore have very little structural variation with depth at a given point. As such, the confocal resolution of the RM system should be comparable to the thickness of the cell to maximize signal collection from the cell and minimize any background collection from the substrate.

The primary spectral window of interest for RM of cells is 600 - 1800 cm^{-1}, as this region contains spectral information from all cellular components: proteins, lipids, nucleic acids, and carbohydrates [27, 28, 30–33, 36, 41, 42]. The smallest spectral separation between two distinct Raman peaks in this window is 6 cm^{-1} [41].

Therefore, to facilitate the detection of every Raman peak within this window, the spectral resolution of the RM system must be < 6 cm^{-1}.

2.5.3 Substrate material

In order to acquire a stable Raman spectrum or image of a cell without using optical tweezer methods for imaging cells in liquid suspension [72, 73], the cell must be attached to a flat substrate. In order to culture the cell such that it will attach properly, the substrate material must be insoluble in water, growth media, buffer solutions, or any other chemicals required to culture the cells or clean the substrate for re-use. The material should also be transparent to the incident laser in order to minimize the contribution from reflected or scattered light originating from outside the desired focal volume.

A further consideration is that the substrate itself must be relatively Raman inert in the spectral window of interest (600 - 1800 cm^{-1}). Two common sources of substrate background signal are unwanted Raman signals, and fluorescence caused by the incident laser exciting the substrate material. Background signal from substrates is a recurring problem in Raman spectroscopy, and can be corrected for by various baseline subtraction methods [74] as long as the background features are broad and reproducible. However, as biological Raman signals are quite weak, a very low background signal from the substrate is required.

2.6 Advantages and disadvantages of Raman spectroscopy

Raman spectroscopy has proven useful in a wide variety of disciplines, some of which are mentioned in section 2.7. The main strength of Raman spectroscopy is the ability to obtain sensitive measurements of molecular composition, structure, and dynamics in a sample while working with optical wavelengths. Virtually any type of sample can be analyzed, whether it be solid, liquid, gas, or vapor. Aqueous molecules and biological specimens requiring water immersion can be analyzed with Raman spec-

troscopy due to the very weak Raman signals from water. The presence of water is a major drawback to infrared (IR) absorption spectroscopy (a common vibrational spectroscopy technique utilizing the resonant absorption of IR wavelengths) due to the high opacity of water in the IR spectrum. Raman spectroscopy is also non-invasive and non-destructive. Most samples will not be perturbed or damaged by Raman spectroscopy, provided that the laser wavelength and power is chosen with care, the sample illumination time is properly considered, and undue sample heating is avoided. In addition, Raman vibrations typically give sharp, discrete signals, allowing a high level of spectral resolution compared to IR spectroscopy.

The primary limitations to Raman spectroscopy arise from the inherently weak Raman effect, as compared to, for example, fluorescence. As such, many Raman experiments require long integration times to achieve a sufficient signal-to-noise ratio (SNR). The collection of Raman signal often competes with fluorescence or unwanted Raman signals from substrates, sample containers, or optical components in the Raman system. Fluorescence spectra are broad and continuous, and contain no information about the vibrational state of a molecule. As such, fluorescence can swamp Raman signals if the respective spectral windows overlap.

2.7 Some modern applications of Raman spectroscopy

The uses of Raman spectroscopy are too numerous to fully discuss here, and are addressed in detail in various Raman spectroscopy texts [61, 62]. There are, however, several major fields of application that deserve mention.

Raman spectroscopy has been used extensively in analyzing the structural chemistry of inorganic compounds, organic molecules, and minerals. A few examples include determining the structural forms of amorphous carbon and diamond [75], distinguishing between the A, B, and Z structural forms of double-stranded DNA [76], and identifying trace elements and minerals in urban dust [77]. Development of

fiber-optic and remote Raman collection techniques have enabled the non-destructive chemical analysis of priceless paintings, ancient dyes, and archeological artifacts [78]. A few major industrial applications of Raman spectroscopy include development and characterization of polymers and emulsions [79], quality control of the mechanical and structural properties of semiconductors used in electronic devices [80], and forensic identification of illicit drugs and explosives [81]. Raman spectroscopy is also routinely used in the pharmaceutical industry for drug screening and investigation of molecular polymorphism [82].

The use of Raman spectroscopy in the biological sciences has become incredibly widespread due to the advantages discussed in sections 1.3 and 2.6. A thorough review of the many biological applications of Raman spectroscopy can be found in various publications [83, 84]. The modern applications of RM in the analysis of single cells, which is pertinent to this work, were summarized in section 1.3.

Chapter 3

Materials & Methods

This chapter provides apparatus details and experimental procedures pertaining to this work. The first half of the chapter (section 3.1) presents the necessary details for general Raman microscopy (RM) analysis. An overview of the workings of the RM system is given (section 3.1.1), and various test samples used for the development and characterization of the RM system are described (section 3.1.2). In addition, the theory and methods are provided for quantitative determination and definition of the spatial, confocal and spectral resolution of the RM system (section 3.1.3). The data analysis process is discussed, and descriptions of the theories and algorithms used are provided (section 3.1.4). The second half of the chapter (section 3.2) deals with RM analysis of human tumor cells. The types of cells used in this work are presented and discussed (section 3.2.1), and the procedures for cell culturing and sample preparation are outlined (section 3.2.2). Finally, the acquisition protocols for RM of single cells, which are used for the results presented in chapter 5, are provided (section 3.2.3).

3.1 General Raman microscopy

3.1.1 System overview

A schematic of the Raman microscopy (RM) system developed for this work is shown in figure 3.1. The excitation beam is generated by a 785 nm continuous wave diode laser (Renishaw Inc., Illinois, IL, USA), which has a maximum power output of 300 mW. To control the final power of the excitation light at the sample, the laser beam first passes through a neutral density filter wheel, which allows for selectable attenuation of the laser beam. The shape of the beam directly output from the laser is a $\sim 5 \times 2$ mm rectangle, which should be expanded to a circular beam that fills the back aperture of the microscope objective (5 mm diameter). This is done using a beam expander (figure 3.1), which consists of a 10x focusing objective followed by a 4x collimating objective, each with a 9 mm diameter circular aperture. The resulting collimated beam exiting the 4x objective is therefore circular with a 9 mm diameter.

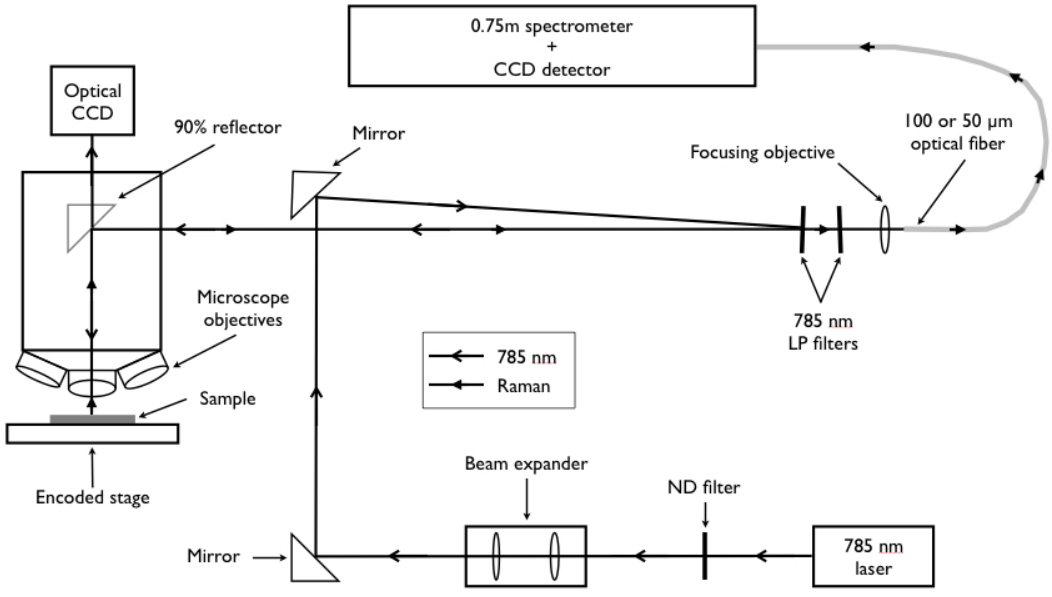

Figure 3.1: Schematic of the RM system developed for this work, showing the optical paths of the 785 nm excitation laser and the Raman scattered light.

The laser beam is reflected upwards by a 45° mirror, and then reflected off another

45° mirror which is angled slightly downward to direct the beam such that it is reflected off a 785 nm low-pass (LP) optical filter (Semrock, Rochester, NY, USA). The LP filters used in this experiment consist of hundreds of thin films deposited in such a way to reflect the 785 nm laser light, but pass light of any longer wavelength with a high transmission efficiency ($> 90\%$).

The laser light is directed into the side port of an upright microscope (Leica Microsystems, Wetzlar, Germany), and reflected downwards by a 90% reflectance 45° mirror onto the back aperture of the microscope objective. The microscope is equipped with 5x, 20x, 50x, and 100x objectives, but only the 50x and 100x objectives are suitable for RM, with NAs of 0.75 and 0.9, respectively. The laser light is focused by the objective onto the sample, which is mounted on a linearly encoded motorized stepper stage with a minimum step size of 0.1 μm and repeatability of ± 0.2 μm (Prior Scientific Inc., Rockland, MA, USA). The isotropically scattered light, consisting of both Rayleigh and Raman scattering, is collected and collimated by the microscope objective, with a collection efficiency determined by equation 2.16. The Rayleigh backscattered light is partially transmitted through the 90% reflector and is focused onto a 640×480 pixel CCD camera (Philips Electronics, Andover, MA, USA), allowing visualization of the focused laser spot on the sample. For white light imaging, the 90% reflector is replaced by a 50% beamsplitter, allowing use of the microscope eyepieces and enabling white-light imaging of the sample with the CCD.

The collected light that reflects off the 90% reflector follows the incident beam path back to the LP filters, where the Rayleigh light is reflected and the Raman light is transmitted. The second LP filter (figure 3.1) serves to further block the 785 nm light from reaching the spectrometer. The transmitted Raman light is focused by a 10x objective into either a 100 μm or a 50 μm diameter multi-mode optical fiber (PolyMicro Technologies Inc., Phoenix, AZ, USA). The entrance aperture of

the optical fiber serves as a confocal aperture, as depicted in figure 2.9, section 2.4.

The optical fiber transmits the Raman light to the entrance slit of a 0.75 m focal length Czerny-Turner spectrometer (Acton Research, Acton, MA, USA). It was found that the NA of the fiber optic is sufficiently well-matched with the entrance NA of the spectrometer, as all attempts to improve the light collection efficiency of the spectrometer using a lens-based fiber optic interface (Acton) showed no improvement.

The spectrometer is equipped with a rotating diffraction grating turret which allows the choice between two diffraction gratings of groove densities 600 g/mm or 1200 g/mm. The dispersed light is focused onto the exit focal plane of the spectrometer and is collected by a 1340×400 pixel CCD camera (Princeton Instruments Inc., Trenton, NJ, USA), where the long axis of the CCD is aligned with the dispersion axis of the spectrometer (recall figure 2.6, section 2.3). For all acquisitions, the CCD was Peltier cooled to -75 °C in order to minimize thermal noise.

The microscope stage, microscope optical CCD, and Raman detection CCD were controlled using the WiRE software package (Renishaw). The selection of both the diffraction grating and the grating angle was controlled using the SpectraPro software package (Acton). The laser power was measured using a Laser Power/Energy Meter (Coherent Inc., Santa Clara, CA, USA). Data analysis and processing (section 3.1.4) was performed with Matlab (The Mathworks, Natick, MA, USA).

3.1.2 Test samples for microscope development and characterization

For the initial qualitative development and testing of the RM system, presented in section 4.1, the test samples used are 5 μm diameter polystyrene microbeads (SPI Supplies, West Chapter, PA, USA) dispersed on a silicon substrate. Silicon has a very strong and sharp Raman peak at 522 cm^{-1}, and a broad weak signal between 935 and 1010 cm^{-1}. The strongest polystyrene peak occurs near 1000 cm^{-1} [46]. With this set-up, both X-Y spatial maps and depth (Z) profiles of the peak values of the polystyrene signal can be created to test spatial and confocal resolution, and

the peak values of the silicon signal itself can be used to further test the system's confocal discrimination (section 4.1).

For quantitative measurement of the spatial resolution of the RM system, the test sample used is a 300 nm wide wire of Raman inert metals, with a width accurate to ±2%, deposited on a flat silicon substrate (Institute of Materials Science NCSR "Demokritos", Athens, Greece). The confocal resolution is determined by scanning through the silicon surface adjacent to the wire, which is flat to within ±1 nm. The spectral resolution is determined using the measured spectral profile of the 522 cm^{-1} silicon peak obtained from the same silicon sample. The methods for determining spatial, confocal, and spectral resolution are described in section 3.1.3, and the results are presented in chapter 4, section 4.2.

3.1.3 Determining spatial, confocal, and spectral resolution

If one can directly measure the spatial line spread function (LSF) of an imaging system, then the *spatial resolution* can be determined as follows. The 1D Fourier transform of the LSF is the modulation transfer function (MTF). The MTF is the spatial frequency representation of the LSF, and shows how the relative amplitude of modulation between closely packed spatial features decreases with increased spatial frequency (i.e., decreased distance between features). Spatial frequency is expressed in line pairs per unit distance, where one line pair (l.p.) is composed of a "high-signal" feature next to a "zero-signal" feature of equal width. The modulation between spatial features can be resolved up to the spatial frequency corresponding to where the MTF has decreased to 3% of its maximum amplitude [85]. The 3% spatial frequency obtained from the MTF can be used to calculate the spatial resolution of the imaging system by inverting the spatial frequency and then dividing the resulting distance by 2 to get the minimum separation between like spatial features that can be clearly resolved, which is in fact a definition of spatial resolution itself.

If the line-phantom used to experimentally measure the spatial LSF has a non-

neglible width, then the measured profile can be corrected by deconvolution with a step function which has the same width as the line-phantom. In this work, Raman profiles are obtained across the 300 nm wide wire described in section 3.1.2 and deconvolved with a 300 nm wide step function. Deconvolution was performed in Matlab using the Lucy-Richardson deconvolution algorithm [86, 87] available in the Image Processing Toolbox (The Mathworks, Natick, MA, USA).

The *confocal resolution* can be obtained in the same manner as the spatial resolution, as described above, by measuring the LSF in the Z-axis. The silicon surface described in section 3.1.2, which is flat to within ±1 nm, serves as a suitable line phantom in the X-Z or Y-Z plane, without requiring any deconvolution. In this work the effect of the penetration depth of the laser into the silicon surface is not considered, but this would cause the measured confocal resolution to be poorer than the true value, if indeed there was any significant effect.

The system's *spectral resolution* can be obtained, in the same manner as the spatial and confocal resolution, by measuring the LSF in the spectral domain. The silicon 522 cm^{-1} peak is a strong, sharp signal with a natural width of 3.0 cm^{-1} at 23 °C [88]. The natural Raman profile is Lorentzian, therefore one can obtain the spectral LSF by deconvolving the measured silicon profile with a Lorentzian profile with a width of 3.0 cm^{-1} and centered at 522 cm^{-1}.

3.1.4 Data acquisition and processing

The raw data output from the Raman CCD detector is the total light intensity collected from 20 binned pixels from each column across the long axis (1340 pixels) of the CCD (recall figure 2.6, section 2.3.4). The steps taken to process the raw data are as follows:

- calibrate the X-axis to convert from CCD pixel to Raman shift,
- remove any spikes in the data due to cosmic rays,

- smooth the data with the two-point maximum entropy method (TPMEM),
- estimate and subtract a fluorescent baseline,
- if necessary, generate line profiles or 2D maps from a set of spectra.

Due to the large number of spectra acquired in this work, it was necessary to automate all data processing steps using Matlab. Each step is discussed below.

Calibration of the X-axis in Raman spectroscopy can be done using a sample which has well known Raman shifts. In this work, a solid tablet of Tylenol was used as the spectral standard, and its known Raman shifts were obtained from the McCreery Research Group's archive of Raman Shift Frequency Standards (University of Alberta, Edmonton, AB, Canada). For each spectral window used, a Tylenol spectrum was obtained and the CCD pixel values at each peak were recorded. Using the known Raman shifts for each peak, a calibration curve relating pixel to Raman shift was created by fitting the data with a quadratic function in Matlab. A quadratic function was used since the reciprocal linear dispersion across the CCD varies quadratically with wavenumber (recall equation 2.14, section 2.3.3). The calibration curve was then used to convert each CCD pixel to a Raman shift in wavenumbers.

Cosmic rays (CRs) show up in spectra as sharp spikes in the measured intensity, and typically span no more than a few pixels on the CCD. An automated CR removal program was written which is successful in removing CRs that have peak intensities greater that twice the average value of the spectrum in the local neighborhood of the CR. This is done by iterating over each point in the spectrum, and if the value at a tested point is greater than twice the mean value of a 5-pt window adjacent to the tested value (sampled from the data already tested), then the value is replaced by a new value taken from its local neighborhood. To ensure that the whole span of the CR is successfully removed, the values of the points within ± 2 indices from the tested value are also replaced with new values taken from their local neighborhood.

This algorithm was successful in removing all CRs detected during this work.

TPMEM smoothing is a regularization method that is useful for SNR enhancement of a variety of data types [89, 90], but has been particularly successful for use with Raman spectra [91, 92]. The basic theory of TPMEM is as follows. Two adjacent points in a recovered data set are considered to be a 2-point probability distribution. If the values of two adjacent points at indices i and $i+1$ are denoted x_i and x_{i+1}, then the fractional probability for each point is

$$p = \frac{x_i}{x_i + x_{i+1}}, \qquad q = \frac{x_{i+1}}{x_i + x_{i+1}} \tag{3.1}$$

such that $p + q = 1$. The two-point entropy function is defined as $-(p \ln p + q \ln q)$. TPMEM first generates the sum of the 2-point entropies, S, over all x_i. TPMEM then attempts to minimize the function $T = -S + \lambda\chi^2$, where λ is a Lagrange multiplier and χ^2 is the chi-square goodness-of-fit function. By minimizing T, TPMEM achieves a balance between smoothness of the recovered data (through S) and fidelity of the recovered data to the original data (through χ^2). Weighting between smoothness and fidelity is determined by choice of λ. A root-bisection algorithm is used to optimize λ subject to the expectation that $\chi^2 = X \cdot \mathrm{NP}$, where NP is the number of data points, and X is a user-defined parameter that biases the resulting data to either increased smoothness ($X > 1$) or increased fidelity ($X < 1$). An example of applying TPMEM to a sample Raman spectra acquired from a human cell, with X varying from 0.5 to 1.25, is shown in figure 3.2. For all cell spectra acquired in this work X was set to 0.75, as this was found to be the highest level of smoothing that doesn't sacrifice fidelity to the observed Raman peaks.

Baseline removal is a necessary step for comparing Raman peaks between different spectra, since the fluorescent baseline will not be consistent between spectra. It is the Raman peak height, or area, above the baseline that provides useful information

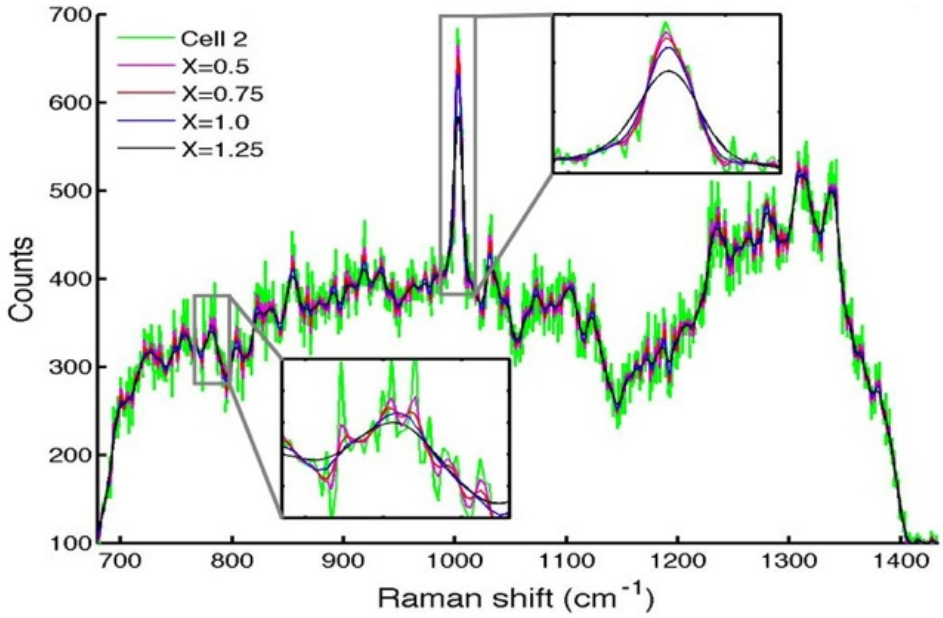

Figure 3.2: Example of applying TPMEM smoothing to a raw Raman spectrum acquired from a human cell (green trace), with the user-defined parameter X varying from 0.5 to 1.25.

about Raman scattering. The algorithm used in this work is a modified version of the signal removal method (SRM) as described by Schulze et al. [74]. An initial crude estimate of the baseline is generated by applying a first-order Savitsky-Golay (SG) filter [93] to the original data, using a window size of 4-6% of the range of the data (1340 points). This initial estimate provides a threshold which separates signal (data above the threshold) from baseline (data below the threshold). The original data is then modified by replacing any data above the threshold with the value of the threshold at that point (i.e., the signal is removed). The SG filter is applied to the modified data set, providing a second estimate of the baseline. The signal removal step is repeated using the SG filter output as the new threshold, and the SG filter is applied again to the modified data set. The process is repeated until a stopping criterion is reached, or a fixed number of iterations is completed. In this work, fixing the number of iterations to 20 proved to be sufficient. The most important parameter in the algorithm was found to be the window size of the SG filter. Smaller window

sizes (e.g. 4% of the data range) allowed more variation in the baseline estimate, whereas larger window sizes (e.g. 6%) yielded less variation. An example of applying the method to a sample Raman spectra acquired from a human cell, with varying SG filter window sizes (W), is shown in figure 3.3. For cell spectral analysis in this work a 71 point window was used for the spectral window shown in figure 3.3, which contains several broad Raman features, whereas a 51 point window was used for the spectral window shown in figure 3.2, in which the Raman features are fairly narrow. Before the generation of spatial Raman profiles or 2D maps, the estimated baseline was subtracted from the TPMEM smoothed data.

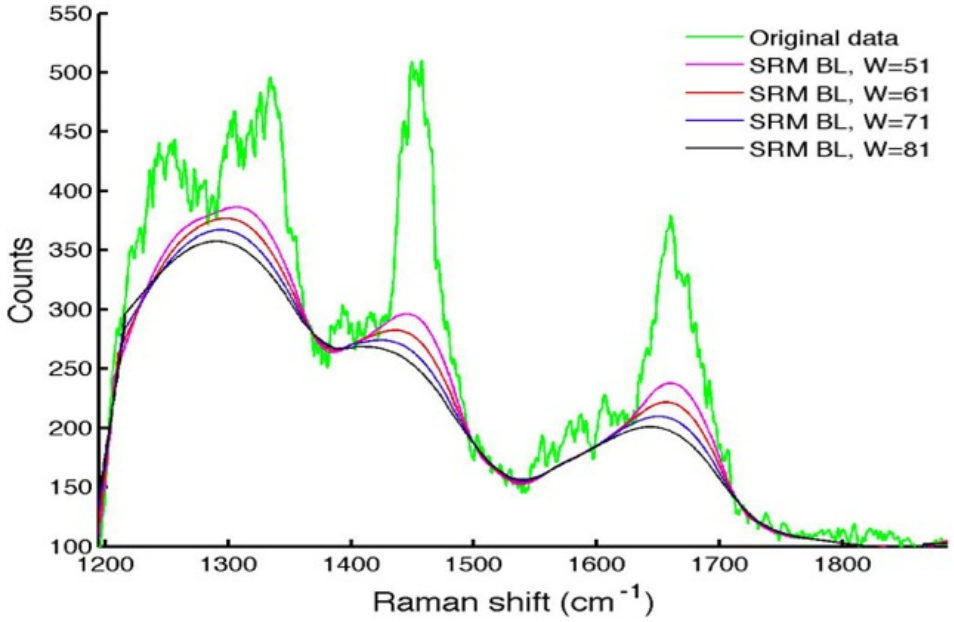

Figure 3.3: Example of applying the signal removal method (SRM) for baseline (BL) estimation of a TPMEM smoothed Raman spectrum acquired from a human cell (green trace), with the Savitsky-Golay (SG) filter window size W varying from 51 to 81 points.

To create a spatial Raman profile or 2D map, spectra are acquired at a known set of points on the sample. The Raman intensities for a given peak are then plotted as a function of position. In this work, the maximum value attained by the peak was used as the indicator of Raman intensity.

3.2 Raman microscopy of human tumor cells

3.2.1 Human tumor cell lines

Two different human tumor cell types, or "lines", were analyzed in this work. Optical images of cells from each line are shown in figure 3.4. The first cell line, designated "A549" (figure 3.4a), is derived from an epithelial lung tumor. The second cell line, designated "DU145" (figure 3.4b), is derived from an epithelial prostate tumor. Original cell stocks were obtained from American Type Culture Collection (ATCC, Manassas, VA, USA). These two cell lines were chosen for several reasons. They are both *adherent* cell lines, meaning they will attach to a surface, which is a necessary requirement for normal RM. They are also both fairly robust and hardy cell lines, allowing for relatively simple handling and preparation procedures in the lab. Furthermore, the Raman spectra of both these cell lines have been recently published by other groups [36, 41, 42]. Finally, for the introductory RM studies performed in this work it was decided that analyzing cell lines of different size and shape would be beneficial. The A549 cells are quite large (20-50 μm in diameter), and tend to splay themselves out when adhering to the growth substrate (figure 3.4a). The DU145 cells are smaller (10-20 μm in diameter) and tend to retain a more compact round shape when adhering (figure 3.4b).

3.2.2 Cell culturing and preparation

To maintain a safe and sterile environment, all cell culture work was done in laminar flow biological safety cabinets at the Deeley Research Centre (DRC) in the BC Cancer Agency Vancouver Island Centre (BCCA-VIC). The cells were cultured in T-25 (25 cm^2 surface area) tissue culture flasks in 15 mL of growth media, supplemented with 10% fetal bovine serum (FBS) (Invitrogen Corp., Carlsbad, CA, USA). Ham's F12 media (Invitrogen) was used for the A549 cells, and Dulbecco's Modified Eagle Medium (DMEM) media (Invitrogen) was used for the DU145 cells. To promote

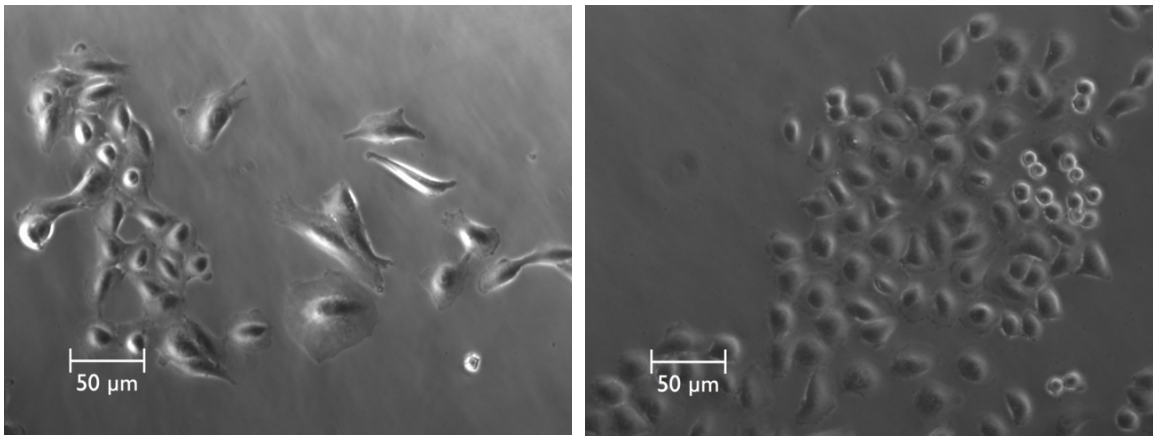

(a) (b)

Figure 3.4: Optical images of (a) A549 and (b) DU145 human tumor cells adhered to the growth substrate. Field of view is $\sim 385 \times 290$ μm.

growth, cells were kept in an incubator at 5% CO_2 and 37 °C.

Every 4-5 days, or when the cells grew to 70-80% confluency within the flask, thus restricting their growth, the cell cultures were harvested and diluted into fresh media to allow the cells to continue healthy growth. The cells were harvested by first discarding the old media and rinsing the cells in phosphate buffered saline (PBS), an ionic buffer solution which maintains osmotic pressure within the cells. About 2.5 mL of trypsin (Invitrogen), an enzyme that causes cells to detach from the growth substrate, was added to the flask and the cells were incubated for ∼5 minutes, or until the cells were seen to fully detach from the flask. The trypsin was de-activated with FBS by adding 5 mL of fresh growth media, and the cell solution was centrifuged at 1200 revolutions per minute for 5 minutes. The supernatant was discarded and the cells were resuspended in 1 mL of fresh growth media. Depending on the level of dilution desired, a small volume of the suspended cells (e.g. 100 μL for a 1:10 dilution) was transferred to a new flask with fresh culture media, and the flask was returned to the incubator.

Prior to performing RM, a small amount (10-20 μL out of the 1 mL suspension) of the harvested cells were transferred to a quartz disc (1 inch in diameter and 1-2

mm thick, described in section 4.3.3) which was immersed in 3 mL of fresh growth media. The cells were then incubated for 24 hours to allow the cells to attach to the disc surface.

There are several ways to perform RM of single cells. Live cells must be kept in an aqueous environment if they are to survive long enough for RM analysis. If water immersion microscope objectives are available, the cells can be analyzed directly in the growth media or in a buffer solution such as PBS. Alternatively, if oil immersion objectives are used, the cells can be analyzed in media or buffer solution under a cover slip to prevent desiccation. If standard dry objectives are used, such as those used in this work, the cells must be *fixed* and dried prior to acquisition. The fixing procedure kills the cells, but preserves the internal structure and chemical composition of the cells after they are dried. There are a variety of cell fixation methods, but a recent comparative study [94] has shown that fixing cells by immersion in a formalin buffer solution is the best method for preserving the internal biomolecular composition of the cell. Since RM is sensitive to biomolecular concentration, formalin fixing was used in this work.

Once the cells had attached to the quartz discs they were removed from the incubator, rinsed with PBS, and immersed in a 10% formalin PBS solution for 15 minutes. The cells were then rinsed with PBS, rinsed with deionized water to remove salts, and quick-dried under compressed air. Formalin fixing can be undone by extended exposure to water [94], so the fixed cells were rinsed with deionized water for only a few seconds and the dried cells were stored in a desiccator until RM analysis.

3.2.3 Raman microscopy of cells

All RM analysis of cells was performed using the 100x objective with the 50 μm diameter optical fiber for the confocal aperture. All cell spectra were obtained with a 2-minute acquisition time and a laser power of $\sim$50 mW at the sample. The lower groove density diffraction grating (600 g/mm) was used in order to acquire as wide

a spectral window as possible. The spectral window covered in this work is 700-1850 cm^{-1}. The region between 600-700 cm^{-1}, which contains a few weak biological Raman features, was not collected in this work. To cover the full spectral window, two diffraction grating angles were required. The first grating angle covered the low-wavenumber range, 700-1350 cm^{-1}, and the second grating angle covered the high-wavenumber range, 1200-1850 cm^{-1}. Therefore, every cell acquisition in this work required two acquisitions, one for each grating angle.

Single-point Raman spectra were acquired at the centre of a cell, which was determined optically using the CCD camera mounted to the top of the microscope (figure 3.1). Four acquisitions of 2 minutes each were obtained, and the four spectra were averaged to improve the SNR. Cosmic rays were removed and the averaged spectra were smoothed with TPMEM, as described in section 3.1.4.

Raman line profiles were obtained by acquiring 16 spectra, separated by 2 μm each, in a horizontal line scan across the centre of a cell. No averaging was performed. The CCD acquisitions and movements of the microscope stage were automated, with the grating angle fixed, for each line scan. Once the first line scan was complete, the grating was rotated to the second angle and the scan was repeated. The spectra were fully processed, and Raman profiles were created, as described in section 3.1.4.

Two-dimensional Raman maps were obtained by defining a grid of points separated by 1 μm, within the WiRE software, where acquisitions would be performed. The stage was then scanned over the grid and 2-minute acquisitions were obtained at each point. Once the scan was complete, the grating was rotated to the second angle and the scan was repeated. The spectra were fully processed, and Raman maps were created, as described in section 3.1.4.

Chapter 4

Results and Discussion I: Raman microscope development and characterization

Three key requirements to perform high-resolution confocal Raman microscopy (RM) of structures on the order of 10 microns or less are: (i) a computer controlled stepper-stage with sub-micron resolution, (ii) a high numerical aperture (NA) microscope objective, and (iii) a suitable diameter confocal collection aperture (recall section 2.4). As described in section 3.1.1, the RM system is equipped with a linearly encoded motorized stepper stage with a minimum step size of 0.1 μm and repeatability of $\pm$0.2 μm. The microscope is also equipped with two objectives suitable for high-resolution microscopy, namely the 50x (NA = 0.75) and 100x (NA = 0.9) objectives. For the confocal collection aperture, 100 μm and 50 μm diameter optical fibers are available.

The purpose of this chapter is threefold. Firstly, the performance of the RM system using different stage step-sizes, different objectives, and different confocal aperture sizes will be qualitatively examined (section 4.1). These results allow the optimum parameters to be determined (in terms of step-size, objective, and aperture size) for RM of cells and sub-cellular structures. Secondly, quantitative measurements of the spatial, confocal, and spectral resolution of the RM system are presented

(section 4.2). Thirdly, a spectral comparison and discussion of several microscope slide materials is presented, and an optimal slide material is chosen for minimizing background signals when attempting cellular imaging (section 4.3). The chapter concludes with a brief summary of the most important results presented (section 4.4).

4.1 Qualitative investigation of optimum parameters for cellular imaging

4.1.1 Laser spot characterization

Using the optical CCD camera mounted to the top of the upright microscope (recall figure 3.1, section 3.1.1), images of the laser spot can be obtained when it is focused onto a flat, diffusive surface, such as a silicon substrate. Images of the focused laser spot for the 50x and 100x objectives are shown in figures 4.1a and 4.1b, respectively.

Due to the initial rectangular geometry of the laser beam and some slight divergence of the beam in the Y-axis, the beam is not focused to a perfect circular spot, but rather to an elliptical spot with its major axis aligned in the Y direction. For measurement of the full-width at half-maximum (FWHM) along each axis, the X and Y profiles through the centre of the spot have been plotted, for both objectives, in figures 4.1c and 4.1d. For the 50x objective, the X-axis FWHM is measured to be 1.8 μm and the Y-axis FWHM is measured to be 5.0 μm. For the 100x objective, the X-axis FWHM is 0.9 μm and the Y-axis FWHM is 2.2 μm. It is important to note from the profiles (figures 4.1c and 4.1d) that the optical CCD becomes saturated at the centre of the laser spot image (especially with the 50x objective). Thus, the FWHM values measured and quoted here are actually larger than the true FWHM of the focused laser spot. Unfortunately, the current equipment does not allow for a smaller incident laser power, and both the CCD camera exposure time and CCD gain were set to their minimum values. As such, the CCD saturation is currently

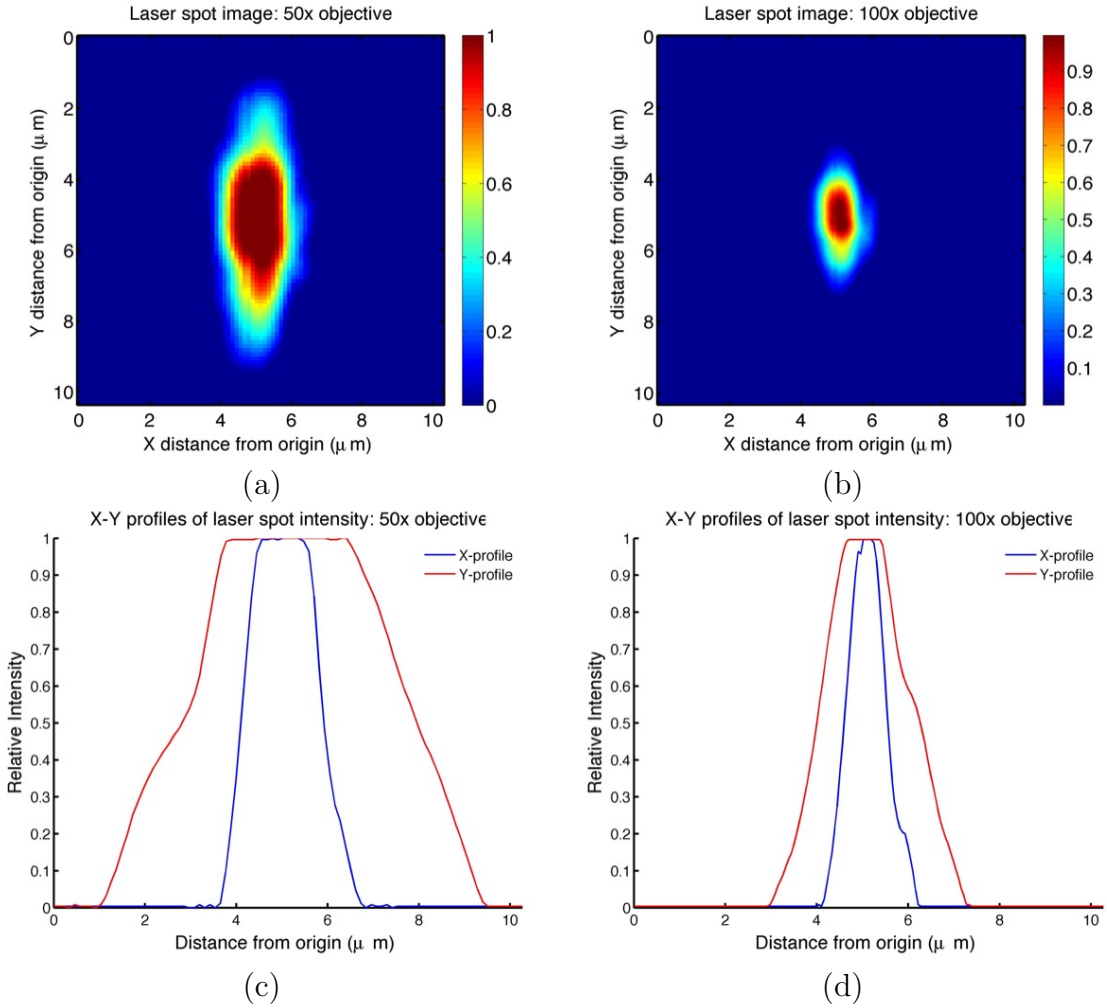

Figure 4.1: Relative (a,b) optical images and (c,d) X-Y profiles of the focused laser spot for the (a,c) 50x and (b,d) 100x objectives. The laser is focused onto a flat silicon surface and images are obtained with an optical CCD camera mounted to the optical microscope. CCD saturation results in the truncated intensity values at the centres of the laser spot images and profiles.

unavoidable, and the FWHM values quoted serve as a suitable upper bound for the true FWHM of the focused laser spot.

4.1.2 Test samples: microbeads on silicon

The test samples used for qualitatively evaluating the performance of the RM system are 5 μm diameter polystyrene microbeads resting on a silicon substrate (recall section 3.1.2). A sample Raman spectrum obtained using a 5 second acquisition at the centre of a microbead is shown in figure 4.2. Note that a constant baseline offset of ∼600 counts is applied by the CCD during acquisition and readout. All Raman profiles and maps shown in this work were created after subtraction of this baseline, and the maximum value obtained by the peak above the baseline is used as the indicator of Raman intensity.

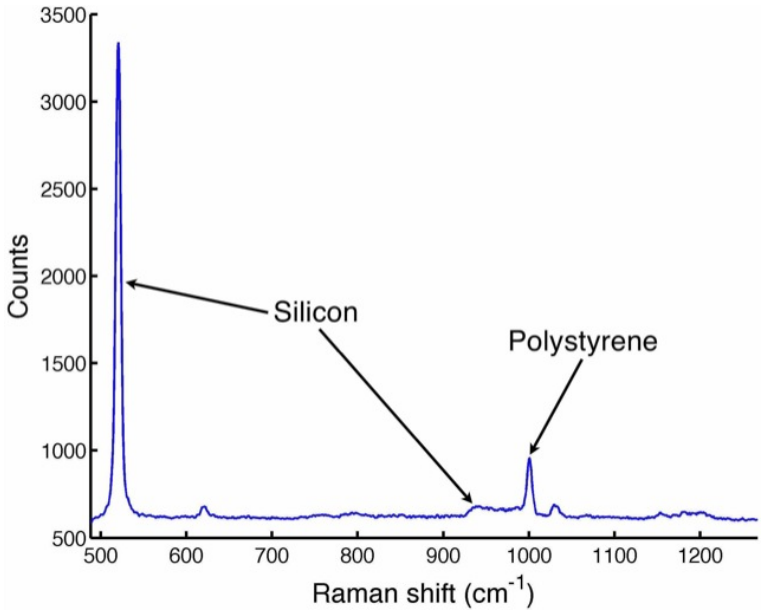

Figure 4.2: Sample Raman spectrum obtained from the centre of a polystyrene microbead resting on a silicon substrate. Acquisition time = 2 sec, laser power ∼10 mW at the sample.

Microbeads were dispersed randomly on the silicon substrate, and two regions of interest (ROIs) were chosen. One ROI contains an isolated single bead, and the other contains three beads in a closely packed triangular geometry. Figures 4.3a and 4.3b show optical microscope images of the two bead arrangements. These two ROIs are

hereafter referred to as the single bead and triple bead patterns, respectively. Spatial maps and profiles, of both polystyrene and silicon signals, are obtained from these bead patterns to evaluate the spatial and confocal performance of the RM system with varying parameters (sections 4.1.3, 4.1.5, and 4.1.6). In addition, depth profiles of the polystyrene signal, through the vertical axis of the beads, are used to further evaluate the RM system's confocal discrimination (section 4.1.4).

(a) (b)

Figure 4.3: Optical microscope images of 5 μm diameter polystyrene beads on silicon, in (a) single bead and (b) triple bead patterns, showing the 8×8 μm ROIs used. Images obtained with 100x objective. Field of view is 36.5×27.5 μm.

4.1.3 Varying stage step-size

The minimum repeatable step size for the sample stage is 0.2 μm. However, scanning a large field of view with this step size may not be practical due to time constraints. To quantify the effect of varying step size, scans were obtained from the single bead and triple bead patterns, using the 100x objective with the 50 μm aperture, for step sizes of 0.8 μm, 0.4 μm, and 0.2 μm. The spatial maps of the polystyrene signal from the bead(s) are shown in figures 4.4a-f.

Horizontal profiles have been extracted from the centres of the single bead maps from figures 4.4a, 4.4c, and 4.4e, and are shown as normalized profiles in figure 4.5a. In an effort to increase the SNR in the profiles, all rows from 3.4 μm to

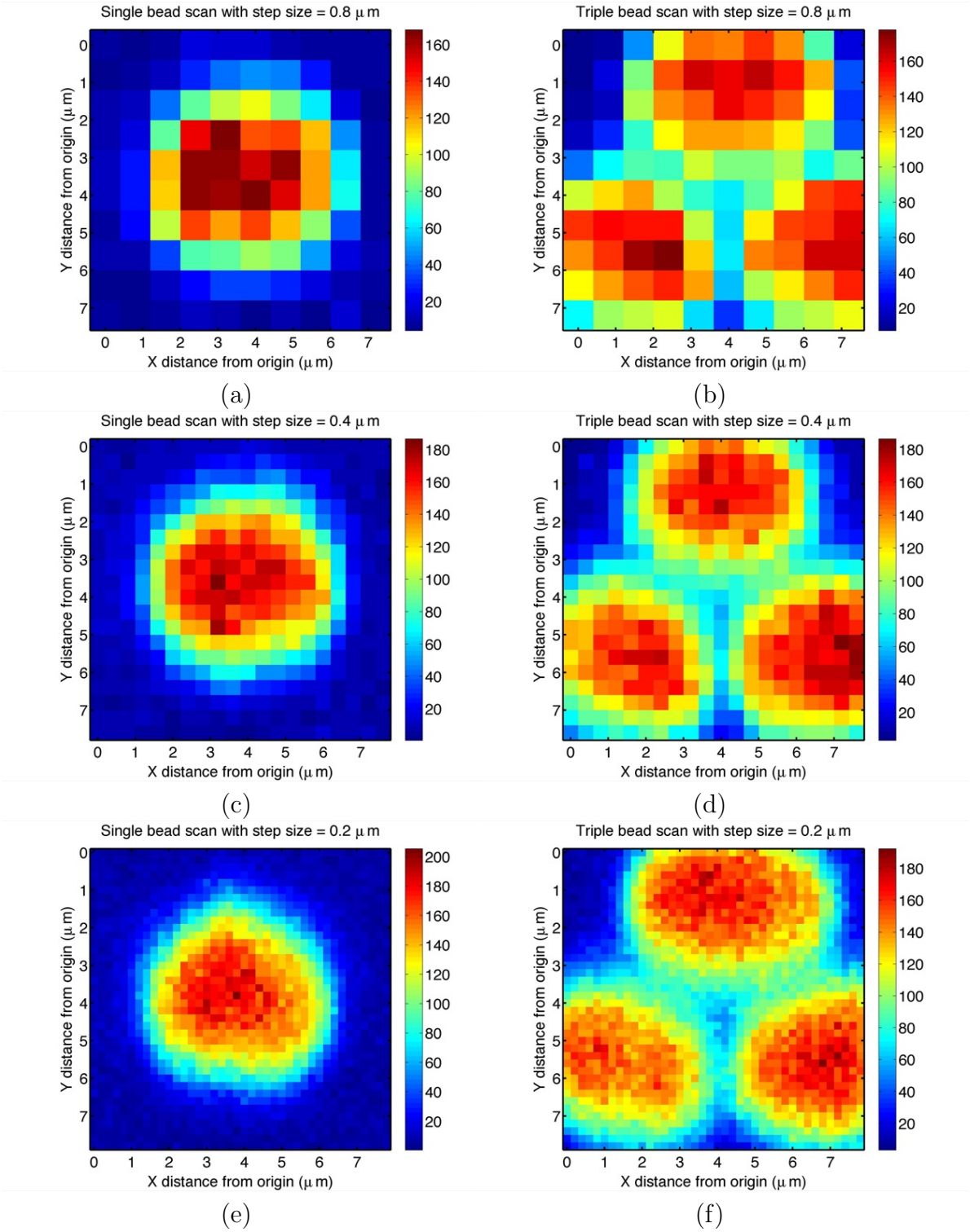

Figure 4.4: Spatial maps of the polystyrene signal from the single and triple bead patterns, for step sizes of (a,b) 0.8 μm, (c,d) 0.4 μm, and (e,f) 0.2 μm, using the 100x objective and 50 μm confocal aperture. Acquisition time = 2 sec / pixel, laser power ~10 mW at the sample.

4.0 μm have been averaged together before normalization to generate an averaged profile. Horizontal profiles have also been extracted from the centre of the bottom two beads in the triple bead pattern scans (figures 4.4b, 4.4d, & 4.4f), and are shown as normalized profiles in figure 4.5b. For these profiles, the rows from 5.4 μm to 6.0 μm were averaged together before normalization.

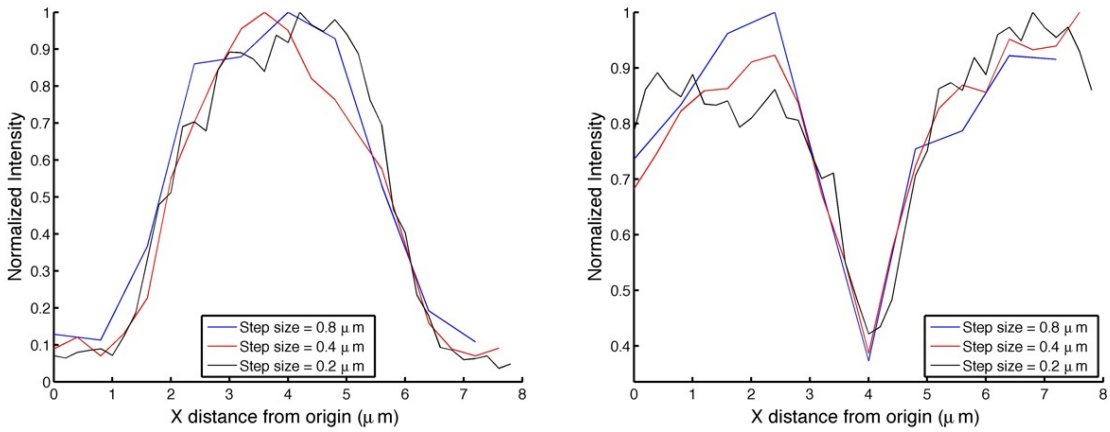

Figure 4.5: Horizontal averaged profiles extracted (a) from rows in the range from 3.4 μm to 4.0 μm of the single bead maps in figures 4.4a, 4.4c, and 4.4e, and (b) from the rows in the range from 5.4 μm to 6.0 μm in the triple bead maps in figures 4.4b, 4.4d, and 4.4f.

From figures 4.4a-f, it is clear that decreasing the step size results in improved image quality and an overall improvement in the ability to resolve the true spherical nature of the beads. However, it is important to note that decreasing the step size by a factor of 2 causes the total scan time to increase by a factor of 4. For these 8×8 μm fields with an acquisition time of 2 seconds per pixel, the total scan times were $\sim$10 minutes for the 0.8 μm step size, $\sim$40 minutes for the 0.4 μm step size, and $\sim$2.5 hours for the 0.2 μm step size. For a small 8×8 μm field, a 0.2 μm step size is reasonably practical given the improvement in image quality. However for a 16×16 μm field, the required scan time (for 2 second acquisitions per pixel) would be $\sim$10.5 hours, which would likely be impractical for cellular imaging (longer scan times result in higher incidences of motion artifacts and thermal instabilities, as well

as the possibility of instability in the biological sample itself). For fields larger than $8 \times 8 - 10 \times 10$ μm, with this acquisition time, a step size of 0.4 μm would likely be a better choice if imaging the entire field is required. From the profiles shown in figures 4.5a and 4.5b, there is no obvious loss in intrinsic spatial resolution when increasing the step size above 0.2 μm, although from figures 4.4a and 4.4b, a step size of 0.8 μm gives a clearly undesirable loss in image quality for small fields (i.e. $< 10 \times 10$ μm).

4.1.4 Confocal tests: Microbead depth profiles

Depth profiles (or 'Z-scans') were obtained through the vertical axis of the single bead (figure 4.3a), and through the vertical axis of the top bead in the triple bead pattern (figure 4.3b). Data was collected from 20 μm below the silicon surface to 20 μm above the silicon surface in increments of 1.0 μm, with an acquisition time of 5 seconds per step. The location of the silicon surface was determined by focusing the laser on the surface adjacent to the microbead, and was reproducible to within 0.5 μm. Normalized depth profiles of the polystyrene peak intensity from the single and triple bead patterns for the 50x and 100x objectives and the 50 μm and 100 μm confocal apertures are shown in figures 4.6a-d. Data is missing for the single bead, 50x objective, 100 μm aperture case because the optical fiber was switched from 100 μm to 50 μm before it was realized that there was a significant difference in the depth profiles between the single bead and triple bead patterns. It was not deemed necessary to switch the optical fiber back to 100 μm simply to obtain this data set.

A simple comparison of figures 4.6a-d shows that the confocal performance is greatly improved by switching from the 50x to the 100x objective. For example, the FWHM of the single bead depth profile with the 50 μm aperture decreases from 10.6 μm for the 50x objective to 6.9 μm for the 100x objective. This is a direct result of the increased NA and smaller depth of focus of the 100x objective (recall equation 2.18, section 2.4). However, it is also interesting to note that the confocal performance is degraded for both objectives when scanning through a bead that has

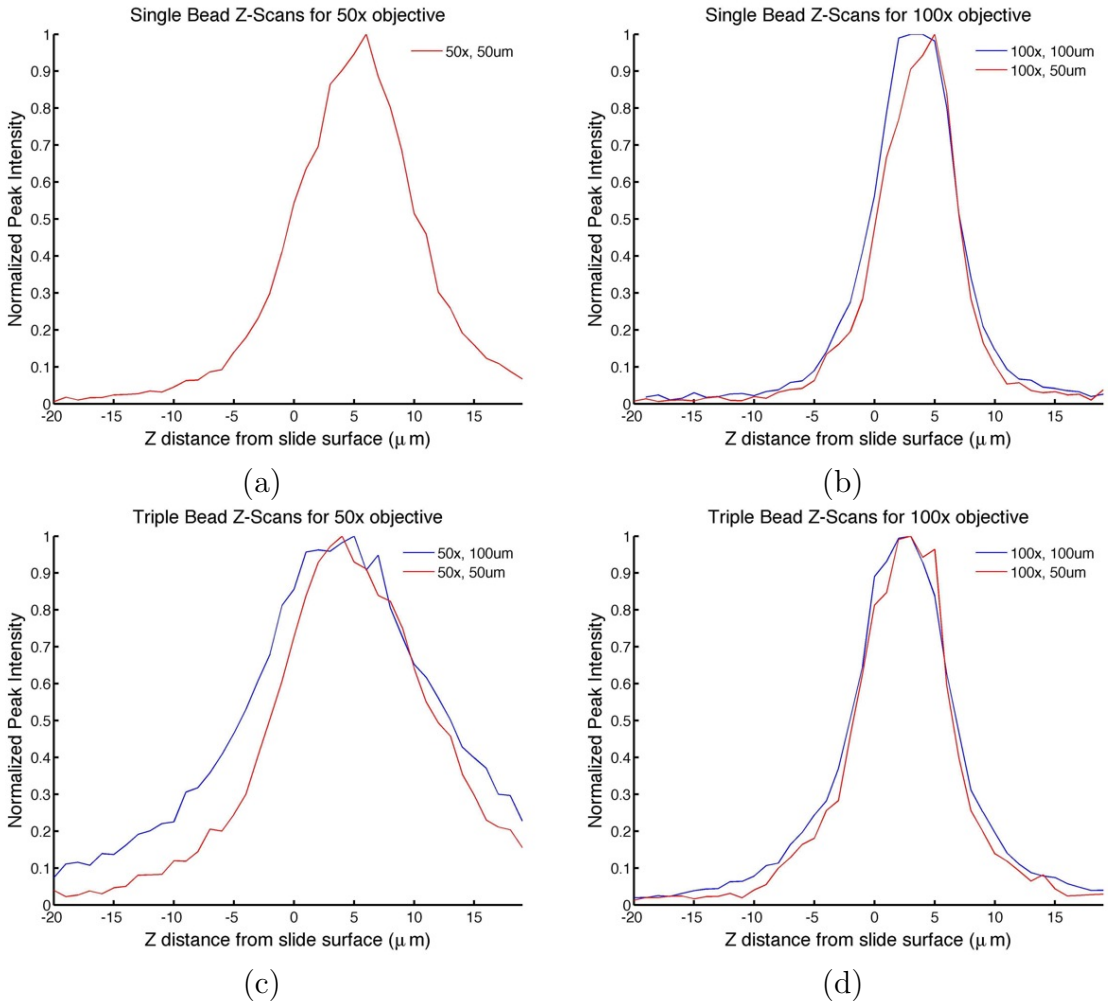

Figure 4.6: Normalized depth profiles from the (a,b) single and (c,d) triple bead patterns for the (a,c) 50x and (b,d) 100x objectives and 50 μm and 100 μm confocal apertures. Step size = 1.0 μm, acquisition time = 5 sec / step, laser power $\sim$10 mW at the sample.

other beads adjacent to it (as in the triple bead pattern Z-scans in figures 4.6c and 4.6d). This is indicative of increased scattered signal being collected due to the transparency of the polystyrene beads themselves. This effect is more problematic with the 50x objective than the 100x objective due to the larger sampling volume of the 50x objective. However, for both objectives, switching from the 100 μm to the 50 μm confocal aperture helps reduce the scattered component, evident from the lower amounts of signal collected in the regions outside of the bead's known physical diameter ($Z < 0$ μm or $Z > 5$ μm). In addition, there is a noticeable decrease in the FWHM of the intensity profile when switching from the 100 μm to the 50 μm aperture. These two effects are very pronounced for the 50x objective, but are also evident in the 100x objective for both the single and triple bead scans. These results suggest that the optimum confocal performance for this system is achieved with the 100x objective and the 50 μm confocal aperture.

4.1.5 Spatial mapping: Single bead scans

Spatial maps of the polystyrene signal from the single bead, for both objectives and both confocal apertures, are shown in figures 4.7a-d. The step size for all cases is 0.2 μm, with a field of view of 8×8 μm (40×40 pixels) and an acquisition time of 2 seconds per pixel. All maps were obtained through the central plane of the bead (in the Z-axis), determined by focusing the laser on the silicon surface adjacent to the bead and moving the stage down by 2.5 μm. Corresponding maps of the silicon signal (generated from the same data set) are shown in figures 4.8a-d.

The single bead images in figures 4.7a-d show significantly increased spatial resolution when switching from the 50x to the 100x objective, based simply on the improved ability to reproduce the known shape of the bead and reject signal from outside the known area of the bead (i.e., cross-section of a sphere with diameter 5 μm). Furthermore, it is evident that for the 50x objective the spatial resolution in the X direction is better than in the Y direction, since the edges of the beads appear

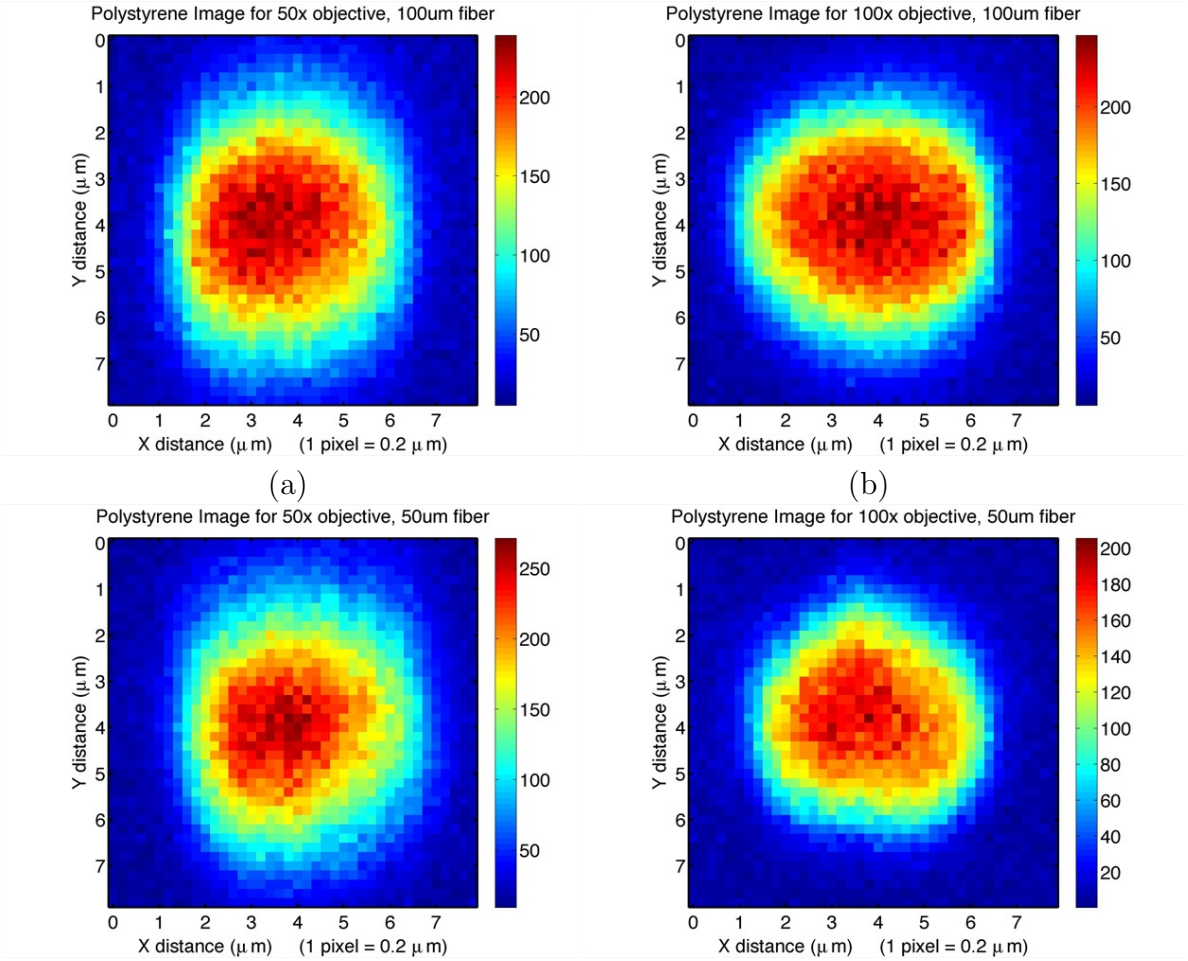

Figure 4.7: Spatial maps of the polystyrene signal from single bead scans, for the 50x and 100x objectives and the 50 μm and 100 μm confocal apertures. Step size = 0.2 μm, acquisition time = 2 sec / pixel, laser power $\sim$10 mW at the sample.

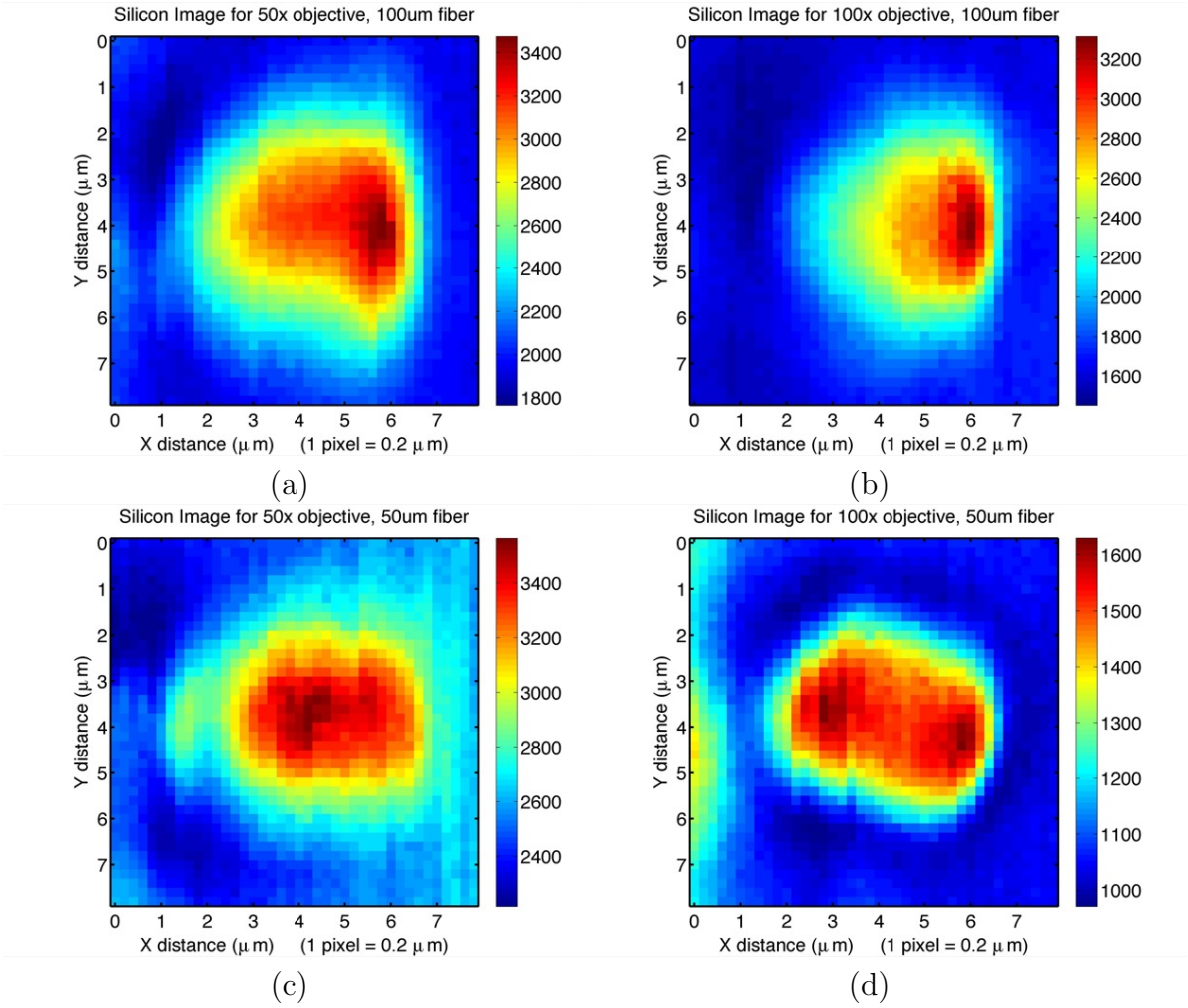

Figure 4.8: Spatial maps of the silicon signal from the single bead scans shown in figures 4.7a-d. Colorbar intensities in each panel indicate the different amounts of silicon signal collected in each case. Step size = 0.2 μm, acquisition time = 2 sec / pixel, laser power $\sim$10 mW at the sample.

significantly blurred in the Y direction when compared to the X direction. This effect is only slightly noticeable for the 100x objective. The cause of this non-symmetry is due the laser not focusing to a perfect circular spot, but rather to an elliptical spot with its major axis aligned in the Y-direction (see figures 4.1a-d).

The increased spatial resolution in switching to a higher magnification (and thus a higher NA) objective are direct results of the smaller focused spot size and increased confocality (as discussed in section 4.1.4). However, the advantages in switching from the 100 μm to the 50 μm confocal aperture are more subtle. In section 4.1.4 it was shown that the smaller aperture increased the rejection of signals scattered from outside of the laser focal volume. However, for the 50x objective and 50 μm aperture, figure 4.14 in section 4.2.2 below shows that the confocal resolution is worse than 5 μm (experimentally determined to be 5.7 μm in section 4.2.2). Thus, for the 50x objective scans on a 5 μm diameter bead, one would expect very little change in the amount of polystyrene signal collected, or in the spatial resolution of the bead, when switching to a smaller aperture. However, for the 100x objective and 50 μm aperture, figure 4.14 in section 4.2.2 shows that the confocal resolution is better than 3.5 μm (experimentally determined to be 3.0 μm in section 4.2.2), which is less than the total diameter of a 5 μm bead. Since it was shown in section 4.1.4 that the 50 μm aperture reduces the collection of signals scattered from outside the laser focal volume, then one would expect to see both a reduction in polystyrene signal collected, and an improvement in spatial resolution of the bead, when switching to the smaller aperture with the 100x objective. This is indeed evident when comparing figures 4.7b and 4.7d; the 50 μm aperture image shows both a $\sim$20% loss in the maximum signal collected, and a noticeable reduction in the apparent bead diameter, which brings the observed diameter closer to the true value of 5 μm. These two changes can be attributed to the 50 μm aperture (with the 100x objective) collecting signal from a smaller volume of the bead than when the 100 μm aperture is used with the same

objective.

The inferences discussed above are strongly supported by the images of the silicon signal extracted from the single bead scans (figures 4.8a-d). The silicon surface is positioned 2.5 μm below the focal plane of the scan, which is set at the centre of the 5 μm bead; therefore, a highly confocal RM system will exhibit minimal silicon signal. There are three important observations to be made from figures 4.8a-d. The first observation is that the silicon signal is strongly focused through the transparent bead itself, since the silicon signal increases dramatically when signal is collected from within the bead. The second observation is that for the 50x objective (figures 4.8a & 4.8c), the maximum amount of silicon signal collected within the bead is roughly the same for both the 100 and the 50 μm apertures (note the color bar scale in the figures). The third observation is that for the 100x objective (figures 4.8b & 4.8d), the maximum amount of silicon signal collected within the bead is $\sim$50% less with the 50 μm aperture than with the 100 μm aperture. The last two observations strongly support the results discussed in the previous paragraph.

4.1.6 Spatial mapping: Triple bead scans

Spatial maps of the polystyrene signal from the triple bead pattern, for both objectives and both confocal apertures, are shown in figures 4.9a-c. The step size for all cases is 0.2 μm, with a field of view of 8×8 μm (40×40 pixels) and an acquisition time of 2 seconds per pixel. The corresponding maps of the silicon signal (generated from the same data set) are shown in figures 4.10a-c. The 50x objective with the 50 μm aperture data is not shown as it was not deemed necessary to collect this data in light of the results already obtained.

Horizontal profiles through the middle region of the bottom two beads (5.4 μm to 6.0 μm) have been extracted from the polystyrene maps from figures 4.9a-c, and are shown as normalized profiles in figure 4.11. As was done with the previous triple bead profiles (figure 4.5b), the rows from 5.4 μm to 6.0 μm have been averaged together

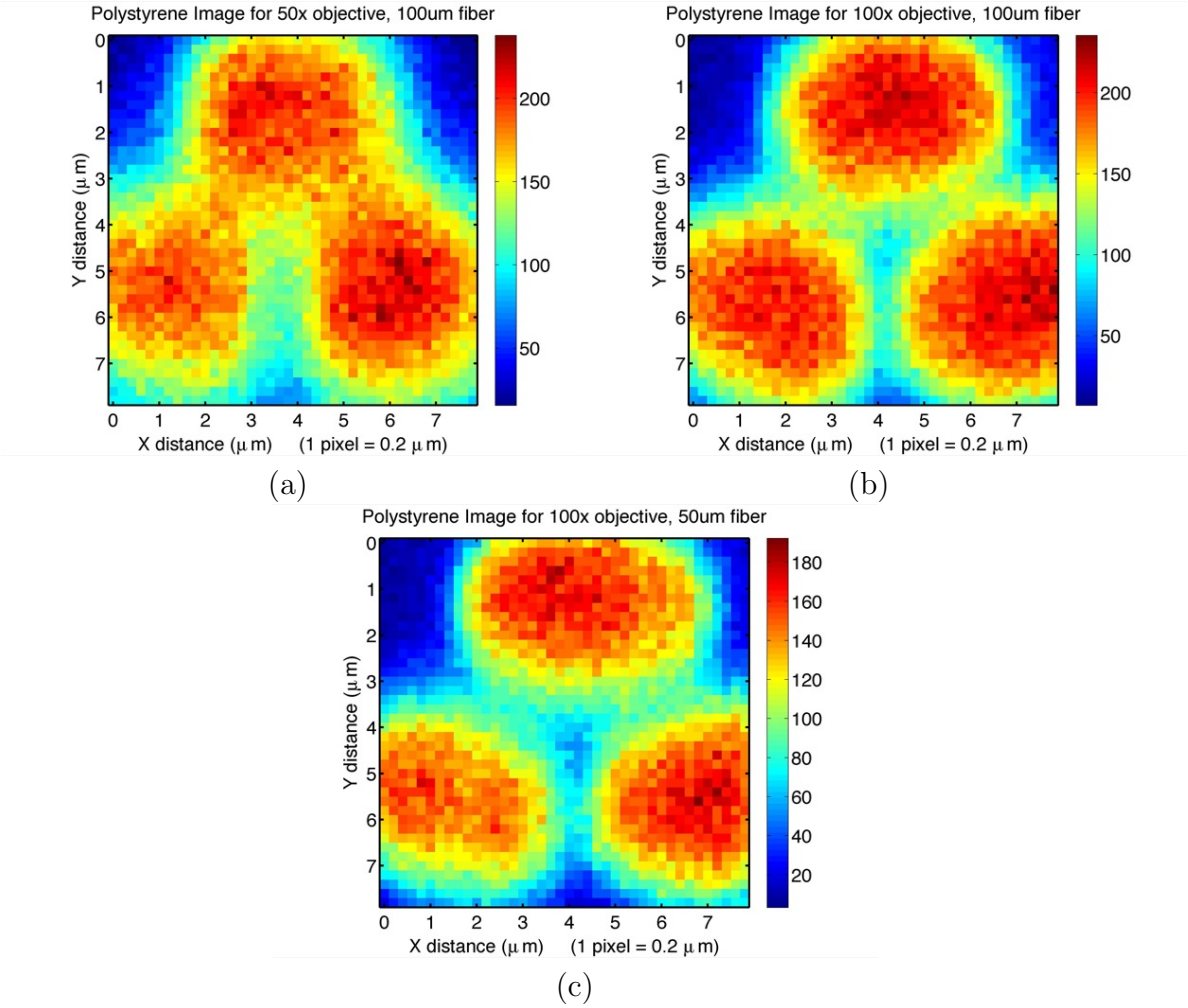

Figure 4.9: Spatial maps of the polystyrene signal from the triple bead pattern scans, for 50x and 100x objectives and for 50 μm and 100 μm apertures. Step size = 0.2 μm, acquisition time = 2 sec / pixel, laser power $\sim$10 mW at the sample.

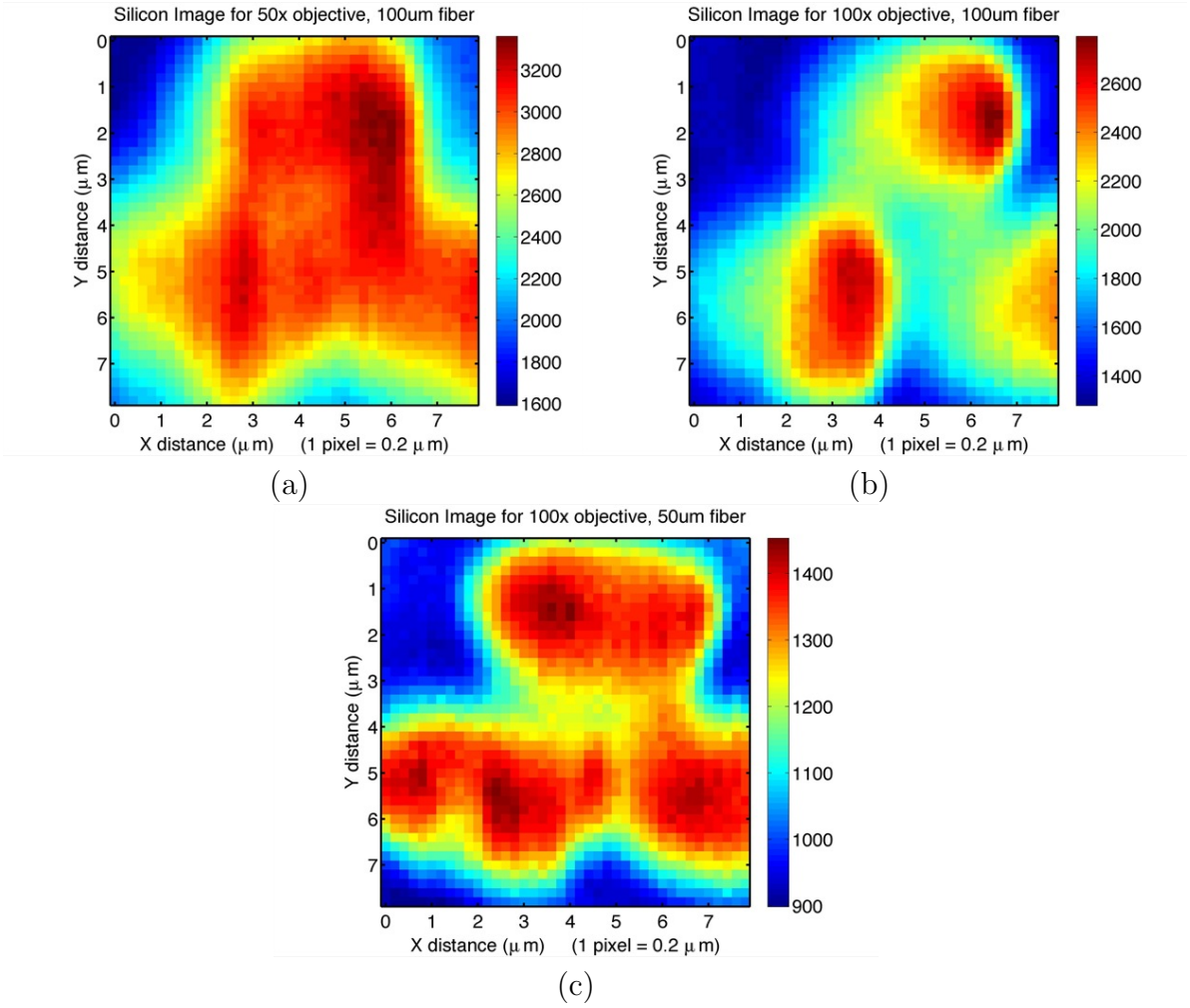

Figure 4.10: Spatial maps of the silicon signal from the triple bead pattern scans shown in figures 4.9a-c. Colorbar intensities in each panel indicate the different amounts of silicon signal collected in each case. Step size = 0.2 μm, acquisition time = 2 sec / pixel, laser power $\sim$10 mW at the sample.

before normalization to generate an averaged profile.

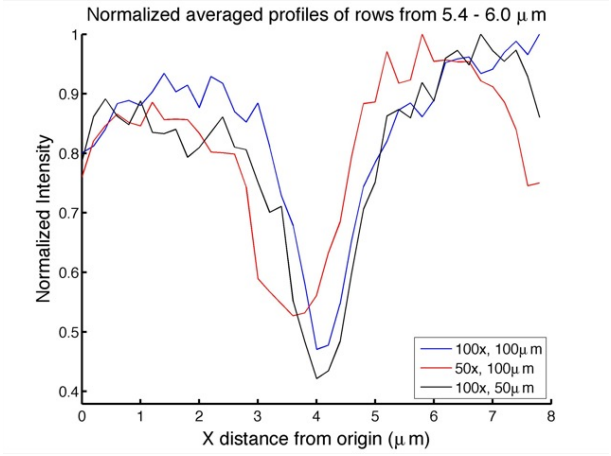

Figure 4.11: Horizontal profiles through the middle region of the bottom two beads, extracted from the polystyrene bead maps shown in figures 4.9a-c. Profiles shown are the normalized average of the 4 rows forming the middle region of the two bottom beads.

The results from the triple bead scans (figures 4.9a-c) corroborate the results of the single bead scans. There is a significant improvement in resolving the beads when switching from the 50x to the 100x objective (with the 100 μm aperture). The poorer spatial resolution in the Y direction is quite evident in the 50x scan (figure 4.9a), as it was in the single bead 50x scans (figures 4.7a & 4.7c), but is also now evident in the triple bead 100x scans (figures 4.9b & 4.9c), as the gaps between the bottom beads and the top bead are less resolved than the gap between the the bottom two beads. However, this effect is the least noticeable in the 100x objective, 50 μm aperture case; indeed the 100x objective, 50 μm aperture case provides the most clearly resolved triple bead pattern. Since all three beads are indeed clearly resolved, and since it is known that the physical distance between the beads is less than 1 μm (figure 4.3b), one can conclude that with the 100x objective and the 50 μm confocal aperture, a spatial resolution on the order of 1 μm is obtained.

The silicon images in figures 4.10a-c show the same improvement in confocal discrimination when switching to the 50 μm aperture with the 100x objective as was observed with the single bead images. In addition, the horizontal profiles through the

bottom two beads, shown in figure 4.11, also show that the best resolution of the two bottom beads is obtained with the 100x objective and the 50 μm aperture. These results support the previous inferences of the advantages of the 50 μm aperture with the 100x objective discussed in the previous two sections.

4.1.7 Summary of optimum parameters

Using 5 μm diameter polystyrene microbeads on a silicon substrate, it was found that the best spatial resolution and confocal discrimination of the RM system is obtained with the 100x objective and the 50 μm confocal aperture. Furthermore, the best image quality is obtained using a 0.2 μm step size. With this set-up, spatial scans of the triple bead pattern show that the overall spatial resolution is on the order of 1 μm. Quantitative measurements of the spatial and confocal resolution of the RM system are presented in sections 4.2.1 and 4.2.2 below.

4.2 Spatial, confocal, and spectral resolution

4.2.1 Quantification of the X and Y spatial resolution using a 300 nm wide wire on silicon

Using the method described in section 3.1.3 for determining spatial resolution, line spread functions (LSFs) for the RM system with the 100x objective and the 50 μm aperture, for both the X and Y axis, have been obtained by using a 300 nm wide wire of Raman inert metals deposited on a silicon substrate. Optical images of this wire in horizontal and vertical orientations, obtained with the 100x objective, are shown in figures 4.12a and 4.12b, respectively.

By scanning across the wire in 0.2 μm increments and recording the decrease in silicon signal over the wire, then inverting and normalizing the original profiles, the raw profiles through the wire feature, for each axis, are obtained. The true LSF is approximated by deconvolving the profiles by a 300 nm wide step function, which accounts for the non-negligible width of the wire itself. The raw and deconvolved

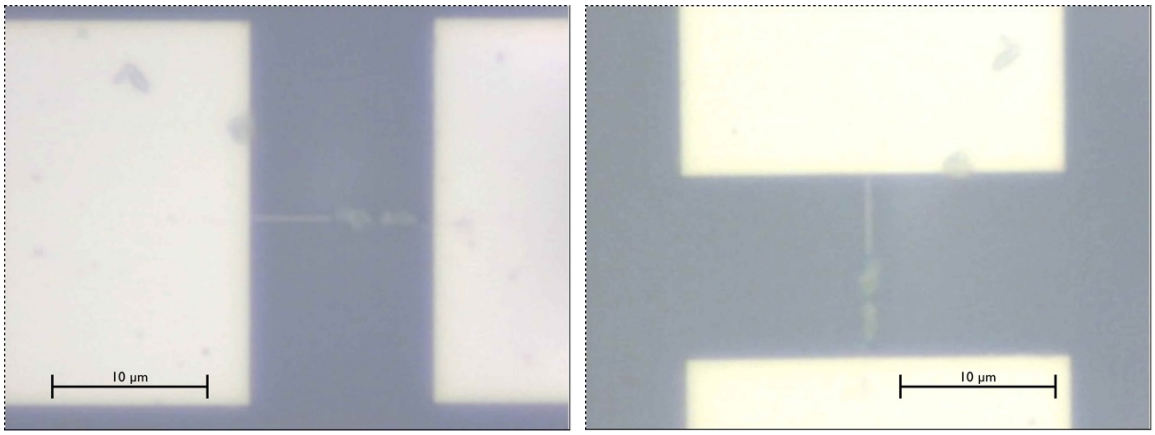

(a) (b)

Figure 4.12: Optical images of 300 nm wide wire in (a) horizontal and (b) vertical orientations, obtained with the 100x objective. Field of view is 36.5 × 27.5 μm.

LSFs for each axis are shown in figure 4.13a. The normalized modulation transfer functions (MTFs) for the raw and the deconvolved data, for each axis, are shown in figure 4.13b.

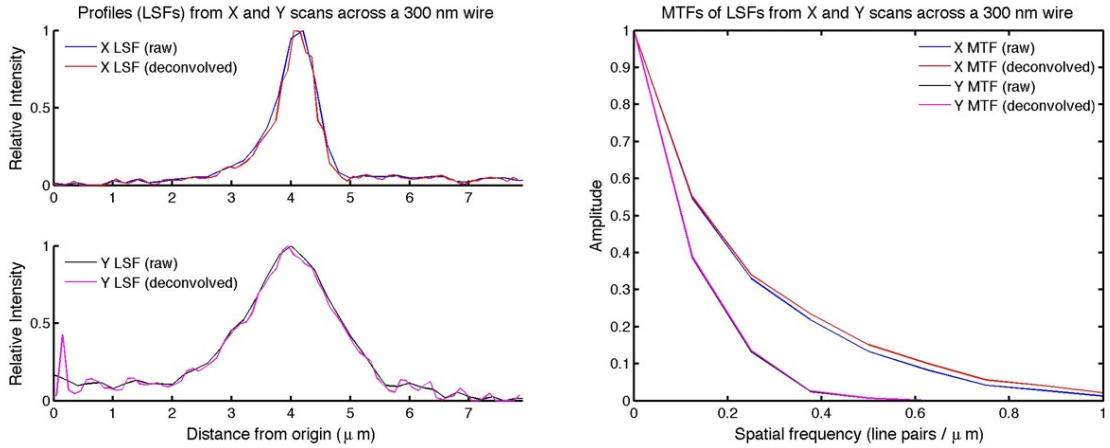

(a) (b)

Figure 4.13: (a) Raw and deconvolved LSFs obtained from scanning across a 300 nm wire on a silicon substrate and deconvolving the raw profiles with a 300 nm step function, and (b) the corresponding MTFs for each case. Step size = 0.2 μm, acquisition time = 2 sec / pixel, laser power ∼10 mW at the sample.

From the MTFs shown in figure 4.13b, the spatial frequencies at the 3% amplitude level for the raw scans are 0.852 l.p./μm for the X-axis, and 0.369 l.p./μm for the Y-axis. This corresponds to spatial resolutions of 0.59 μm for the X-axis and 1.4 μm

for the Y-axis. Using the deconvolved scans, the spatial frequencies increase slightly to 0.943 l.p./μm for the X-axis and 0.372 l.p./μm for the Y-axis, corresponding to spatial resolutions of 0.53 μm for the X-axis and 1.3 μm for the Y-axis.

4.2.2 Determining the confocal resolution using silicon surface depth profiles

Using the method described in section 3.1.3 for determining confocal resolution, confocal LSFs for the 50x and 100x objectives with the 50 μm aperture are shown in figure 4.14a. The step size was set to 0.5 μm, and data was obtained by scanning along the Z-axis from 10 μm below to 10 μm above the silicon surface. The corresponding MTFs are shown in figure 4.14b. For the 50x objective MTF, the spatial frequency at the 3% amplitude level is 0.088 l.p./μm, corresponding to a confocal resolution of 5.7 μm. For the 100x objective MTF, the spatial frequency at the 3% amplitude level is 0.165 l.p./μm, corresponding to a confocal resolution of 3.0 μm.

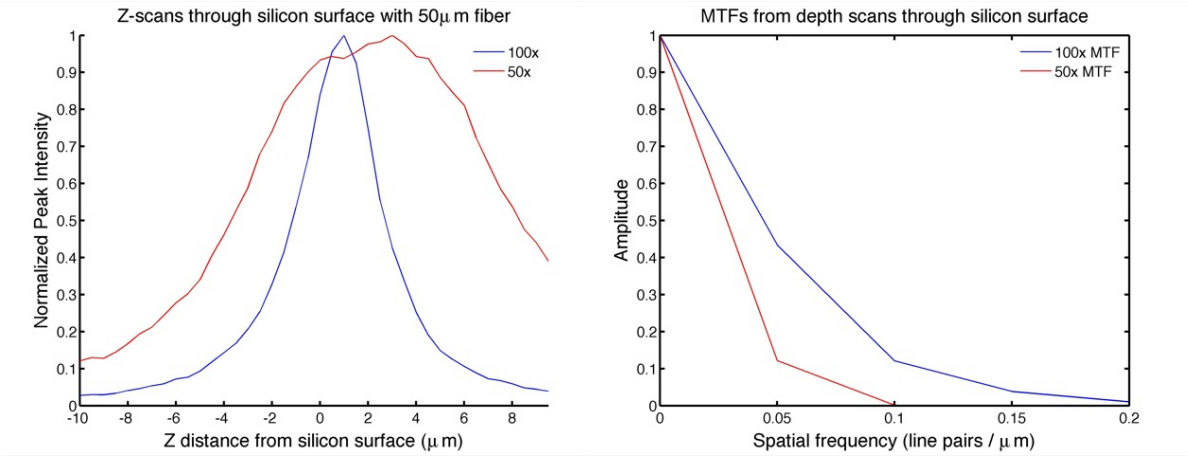

(a) (b)

Figure 4.14: (a) Line spread functions and (b) corresponding MTFs, obtained from depth profiles through the silicon surface for the 50x and 100x objectives with the 50 μm aperture. Step size = 0.5 μm, acquisition time = 5 sec / pixel, laser power ~10 mW at the sample.

4.2.3 Determining the spectral resolution using the silicon 522 cm^{-1} line

Using the method described in section 3.1.3 for determining spectral resolution, spectral LSFs have been obtained for both the 600 g/mm and the 1200 g/mm diffraction gratings, with the grating angle set so that the silicon peak at 522 cm^{-1} is centered on the CCD camera. The raw measured, theoretical, and deconvolved silicon spectra for the 600 g/mm and 1200 g/mm gratings are shown in figures 4.15a and 4.15b, respectively, and the corresponding MTFs of the raw measured and deconvolved spectra for each grating are shown in figures 4.15c and 4.15d.

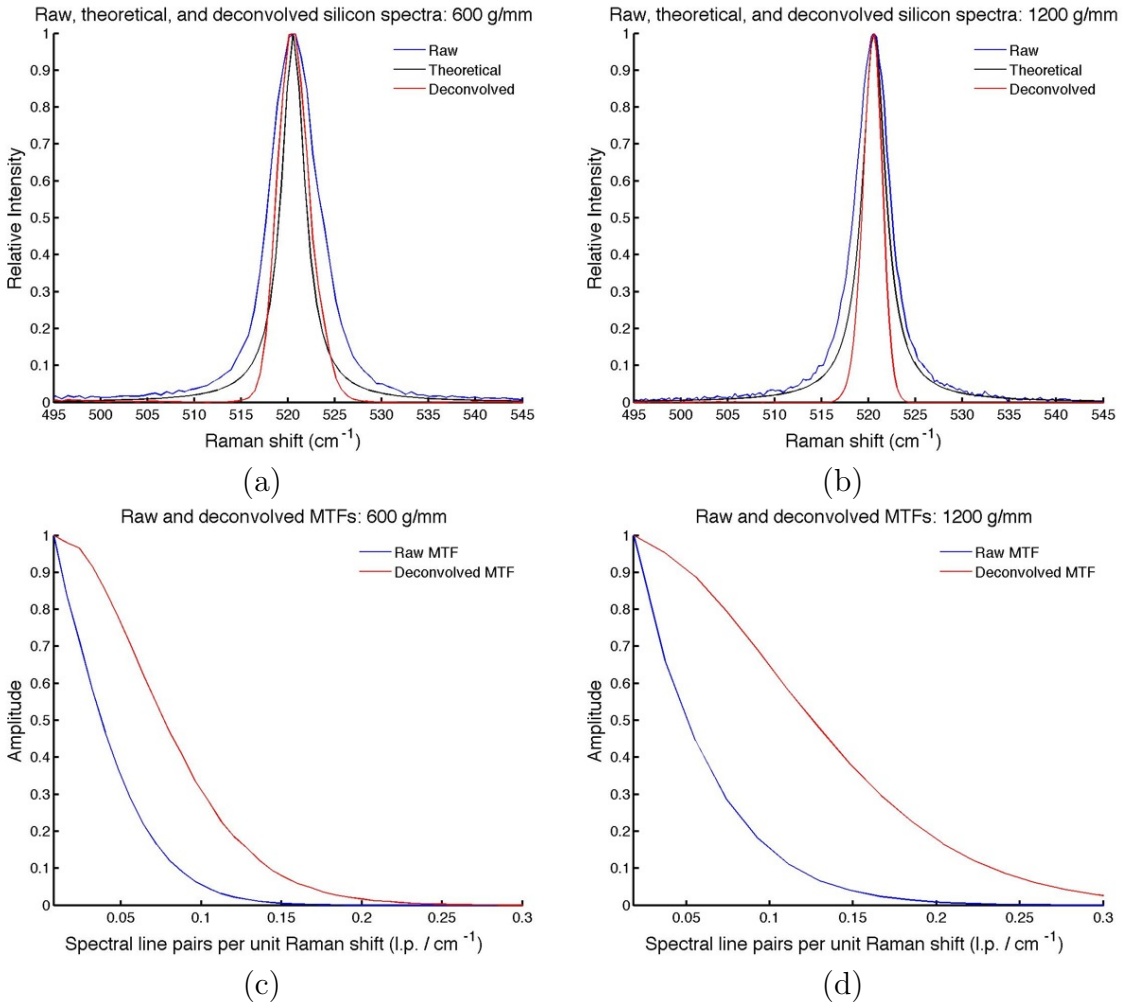

Figure 4.15: (a,b) Raw measured, theoretical, and deconvolved silicon spectra for the (a) 600 g/mm and (b) 1200 g/mm gratings, with (c,d) the corresponding MTFs of the raw measured and deconvolved spectra for each grating.

From the MTFs shown in figures 4.15c and 4.15d, the spectral frequencies at the 3% amplitude level, for the raw spectra, are 0.114 l.p./cm^{-1} for the 600 g/mm grating, and 0.160 l.p./cm^{-1} for the 1200 g/mm grating. This corresponds to spectral resolutions of 4.4 cm^{-1} for the 600 g/mm grating and 3.1 cm^{-1} for the 1200 g/mm grating. Using the deconvolved spectra, the spectral frequencies increase to 0.181 l.p./cm^{-1} for the 600 g/mm grating and 0.294 l.p./cm^{-1} for the 1200 g/mm grating, corresponding to spectral resolutions of 2.8 cm^{-1} for the 600 g/mm grating and 1.7 cm^{-1} for the 1200 g/mm grating.

4.3 Substrate materials for biological Raman microscopy

The general criteria for choosing a suitable substrate for RM of cells were discussed in section 2.5.3. To summarize, the most important characteristics are durability during sample preparation, transparency to the incident laser, and Raman inactivity in the spectral window of interest (600 - 1800 cm^{-1}).

4.3.1 Common cell substrates

Cell cultures for biological sciences are commonly seeded on either a glass slide or a plastic culture dish. However, glass typically contains a high level of mineral impurities, causing many types of glass to be highly fluorescent. Plastics (such as polystyrene or acrylic) are not fluorescent, but contain many active Raman signals due to their polymer structure. Raman spectra have been acquired from a glass slide, a polystyrene culture dish, and an acrylic slide, and are shown in figure 4.16. For reference, a Raman spectrum with nothing present in the sampling volume was also collected, and is presented in order to show the desired baseline starting point. The glass spectrum is highly dominated by fluorescence, and both the acrylic slide and polystyrene culture dish contain Raman features throughout the spectral window. To cover the spectral window shown (200 - 1800 cm^{-1}), spectra were acquired at 3 different grating angles. All spectra in figure 4.16 were acquired for 30 seconds with

the 100x objective focused on the surface of the material, and all spectra shown in the following sections were acquired in the same way.

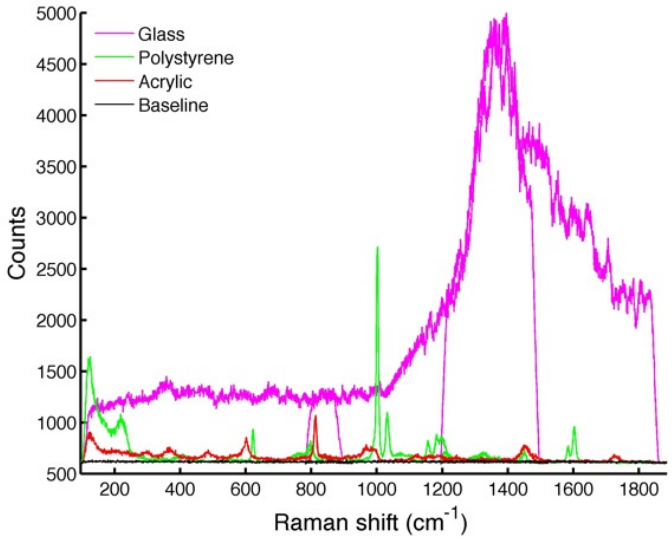

Figure 4.16: Raman spectra of common substrate materials for cell culture that are unsuitable for Raman imaging due to strong background components. The baseline Raman spectra, acquired with no sample present, is also shown. Acquisition time = 30 sec, laser power ∼10 mW at the sample.

4.3.2 Substrate candidate #1: Calcium fluoride (CaF_2)

Calcium fluoride (CaF_2) spectroscopic windows (thin disks typically 1-2 cm in diameter and 1-2 mm thick) have been used as substrates for biological RM [27, 28, 31–33, 36, 42]. The Raman spectra of CaF_2 exhibits a single peak at 322 cm^{-}1 [95], and pure CaF_2 does not fluoresce with infrared irradiation [27]; therefore CaF_2 is a seemingly ideal candidate for cellular RM studies. Although somewhat expensive ($20-$80 per disk), there are many suppliers of CaF_2 windows for spectroscopic purposes across North America.

Initially, eight windows were obtained (CASIX, Fuzhou, Fujian, China), and Raman spectra of the first two windows tested are shown in figure 4.17a. The 322 cm^{-1} CaF_2 peak was measured, but a large unknown signal between 800 and 1800 cm^{-1} was also observed. The spectra of all eight of these windows are shown in figure

4.17b, showing only the dominant unknown features.

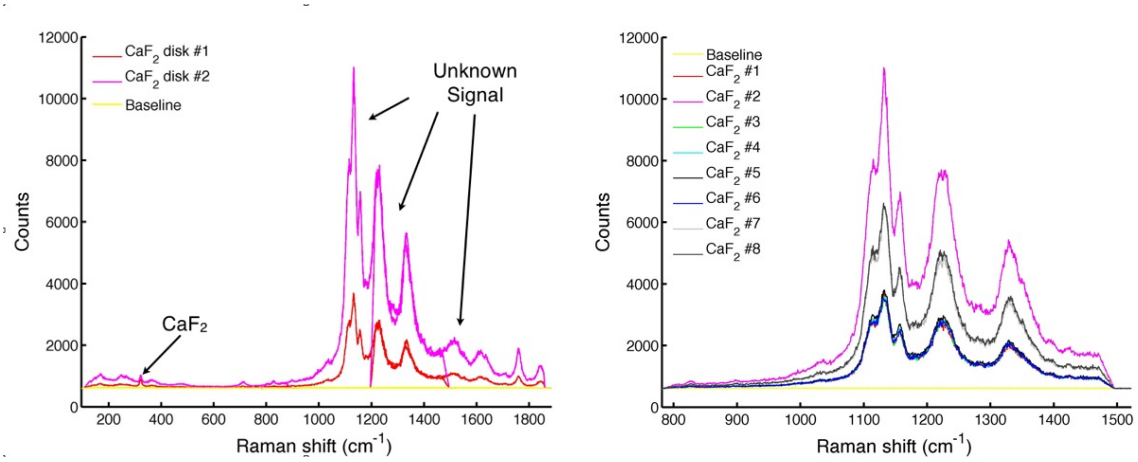

Figure 4.17: Raman spectra of the first group of CaF_2 disks obtained (CASIX, Fuzhou, Fujian, China). Shown are (a) spectra of the first two disks tested, showing the CaF_2 peak and the unknown signals, and (b) spectra of all eight discs obtained, showing the dominant unknown features. Acquisition time = 30 sec, laser power ∼10 mW at the sample.

The unknown features obtained (figure 4.17) were initially suspected to be due to an anti-reflective coating, which is commonly added to many types of spectroscopic windows (it was later found out that CaF_2 doesn't need such coatings). To investigate this possibility, depth profiles through the surface of a disc were obtained, the results of which are shown in figure 4.18. Data was obtained in 2 μm increments to a depth of 60 μm into the disc, with no appreciable loss of the unknown signal (the steady decline of both the unknown and the CaF_2 signal with depth is due to optical attenuation through the disk itself). Spectra were also collected at depths of 100 μm and 150 μm (not shown), and also gave a very high level of the unknown signal.

It was concluded that the unknown signal must arise from impurities impregnated throughout the material, and perhaps a different supplier would yield better results. Four more disks were ordered from a second supplier (Spectral Systems, Hopewell Junction, NY, USA), and the spectra of the four disks obtained are shown in figure 4.19.

Figures 4.17 and 4.19 show that the amount of the unknown signal from a CaF_2

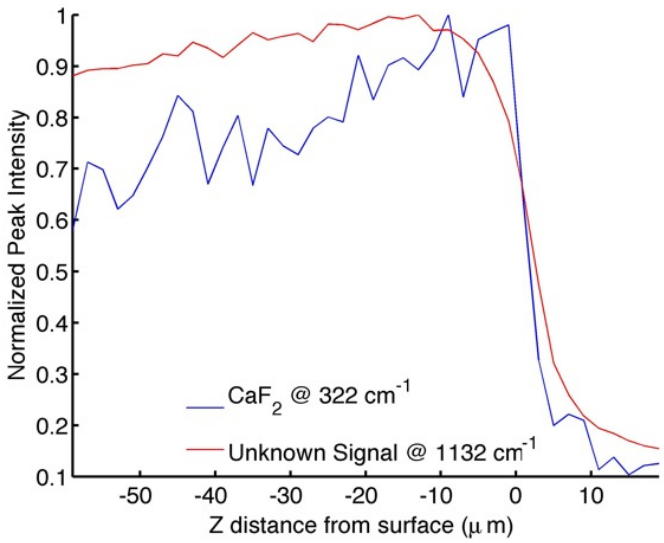

Figure 4.18: Depth profiles through the surface of a CaF_2 disc, with values obtained from the maximum value of the peaks shown in figure 4.17. Step size = 2 μm, acquisition time = 30 sec / step, laser power ~10 mW at the sample.

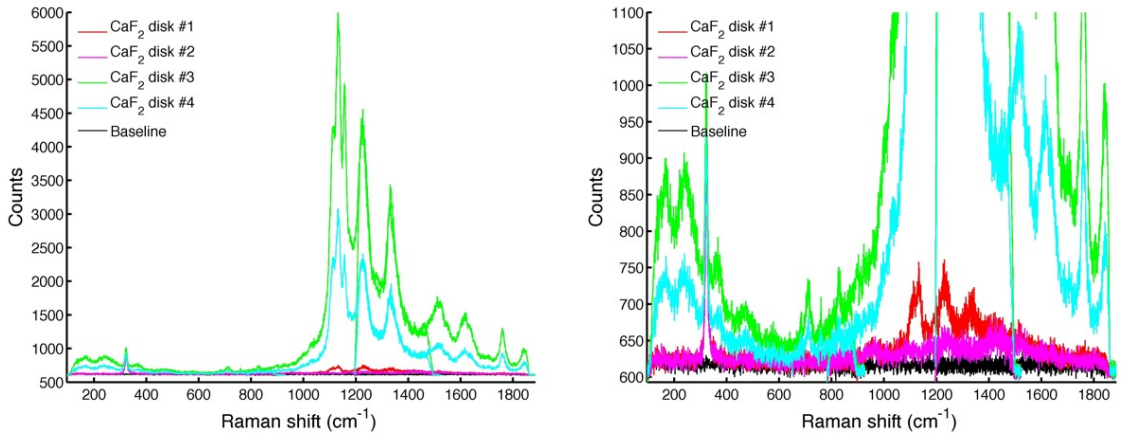

(a) (b)

Figure 4.19: Raman spectra of the second group of CaF_2 disks obtained (Spectral Systems, Hopewell Junction, NY, USA). Shown are (a) full spectra of all 4 disks, and (b) a magnified view of the data in (a), showing more clearly the spectra of disks 1 and 2. Acquisition time = 30 sec, laser power ~10 mW at the sample.

disk is highly dependent on the impurity content within the CaF_2 disc. Through personal correspondence with other groups who have used CaF_2 [32], it was found that some groups have had similar problems obtaining impurity-free CaF_2 windows. Since out of 12 windows tested (at significant expense), only one disk (disk #2 from the second supplier, figure 4.19b) was acceptable for biological Raman use, it was deemed that CaF_2 is not a practical substrate material. Furthermore, it was found that CaF_2 is slightly soluble in phosphate buffered saline (PBS), which is used as an isotonic solution for rinsing cell cultures during sample preparation. Therefore, CaF_2 disks are not completely robust to the cell culture environment, and would slowly deteriorate with repeated use. In light of these drawbacks, other substrate materials were investigated.

4.3.3 Substrate candidate #2: Low-fluorescence quartz

Upon further investigation, it was found that quartz disks and slides can be obtained in very high purity in order to maximize transmittance properties. Standard high purity lab quartz (GE 124) is readily available from many distributors. However, even higher purity quartz (Corning 7980 synthetic flame fused silica) is available from some distributors at higher cost, but with a far lower impurity content. In addition, both types of quartz are cheaper than the CaF_2 disks obtained in the earlier studies. Quartz disks of both types were obtained (Structure Probe Inc., West Chester, PA, USA), and the resulting spectra are shown in figure 4.20.

The spectra of all the quartz slides tested (figure 4.20) are far better than even the best CaF_2 spectra obtained (figure 4.19b). In the spectral window of interest for RM of cells (600 - 1800 cm^{-1}), the quartz spectra is almost completely featureless, with a small broad feature near 800 cm^{-1}. Furthermore, the Corning quartz has even lower background level above 1000 cm^{-1} than the GE 124 quartz, which is indicative of lower fluorescence due to a lower impurity content.

In addition to the low background level relative to CaF_2, quartz is attractive due

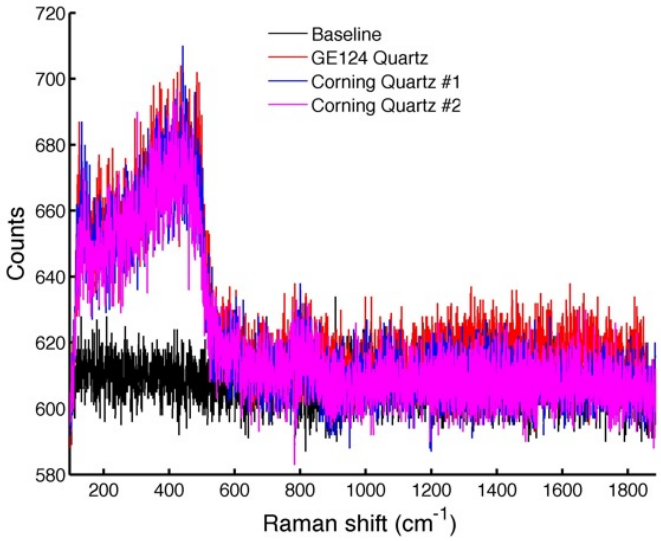

Figure 4.20: Raman spectra of GE 124 type and Corning 7980 type low-fluorescence quartz (Structure Probe Inc., West Chester, PA, USA). The baseline Raman spectra, acquired with no sample present, is also shown. Acquisition time = 30 sec, laser power ∼10 mW at the sample.

to is robustness in the cell culture environment. The Corning quartz disks show no evidence of solubility or corrosion due to extended immersion in cell growth media or buffer solution. Furthermore, the cell cultures used in this work adhere readily to the quartz surface within 24 hours of deposition, and appear to grow in the same fashion as in the polystyrene culture dishes. Cleaning and autoclaving of the quartz slides has been successful as well, with only minimal damage to the disks due to abrasion from various cleaning and handling tools (Kimwipes, cell scraper, tweezers, etc...).

Unfortunately, it appears that all Corning quartz is not completely equal. Corning quartz discs were obtained from a second supplier (Technical Glass Products, Painesville Twp., OH, USA), and high SNR spectra of two discs from each supplier were acquired using 2 minute acquisitions, with a laser power of ∼50 mW at the sample. The spectra from the four discs, in the spectral window of interest (∼600-1800 cm^{-1}), are shown in figure 4.21. Clearly, disc #1 from the second supplier (Technical Glass Products) is inferior to the other 3 discs, especially in the high wavenumber region. This is most likely due to heterogeneity in impurity levels between different

batches of quartz used to make the discs. As such, each disc will be screened before use to ensure it gives a comparable background level to that of the other 3 discs.

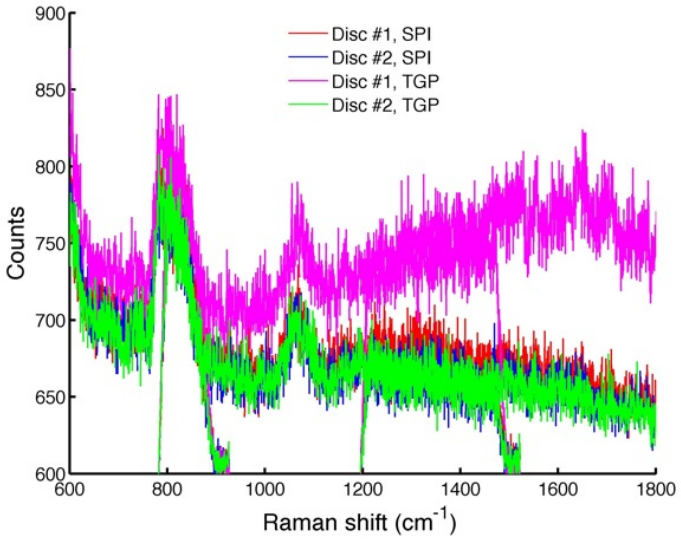

Figure 4.21: Raman spectra, in the window of interest for biological RM (600-1800 cm^{-1}), of Corning 7980 type low-fluorescence quartz discs obtained from Structure Probe Inc. (SPI) and Technical Glass Products (TGP). Acquisition time = 2 min, laser power ~50 mW at the sample.

4.4 Summary

The RM system developed for this work has been successfully characterized, and it has been shown that the performance of the system is optimized for cellular imaging when using the 100x objective and the 50 μm confocal aperture. Quantitative measurements of the spatial, confocal, and spectral resolutions of the RM system have been performed. The spatial resolutions determined, 0.53 μm for the X-axis and 1.3 μm for the Y-axis, are suitable for investigating the interior structure of the cells used in this work (10-50 μm in diameter). The confocal resolution of 3.0 μm is also well suited for these cells due to their thickness (1-4 μm). The spectral resolutions determined, 2.8 cm^{-1} for the 600 g/mm grating and 1.7 cm^{-1} for the 1200 g/mm grating, are both less than the minimum separation between spectral features (6 cm^{-1}) in the window of interest (recall section 2.5.2). Finally, a spectral investigation of micro-

scope slide materials has shown that Corning quartz is a suitable substrate material for RM studies of cells.

Chapter 5

Results and Discussion II: Raman microscopy of human tumor cells

A primary application of this work will be to investigate the effects of ionizing radiation on human cells. This will eventually involve correlating a change in cell spectra between cell cultures that have been exposed to a therapeutic dose of ionizing radiation, and cell cultures that have not. Furthermore, it would be desirable to correlate any observed spectral changes with an accurate position or structure (such as the nucleus, mitochondria, etc...) within the cell volume. Such an experiment could involve collecting Raman spectra from, for example, the nuclear region of 20 individual cells that have been irradiated, calculating an average spectra for the nuclei of irradiated cells, and comparing this resulting spectra with the averaged spectra from 20 cell nuclei that have not been irradiated (averaging spectra from multiple cells is a common technique for spectral comparisons between cell samples [36, 37, 41, 42]). For such an experiment to be successful, the spectral differences observed between the irradiated cell nuclei and the non-irradiated cell nuclei would have to be statistically more significant than the spectral differences observed between individual cells within the irradiated (or non-irradiated) population. Before such an experiment can be performed with any degree of confidence, the normal (non-irradiated) Raman

spectra of a given cell population must be investigated, and the spectral variability between cells (or between like cell structures) must be quantified.

It was shown in chapter 4 that the RM system is optimized for micron-scale confocal Raman collection when using the 100x objective with the 50 μm confocal aperture. The purpose of this chapter is to use these proven capabilities to undertake a detailed Raman spectroscopic analysis of the human tumor cell lines A549 (lung) and DU145 (prostate). The initial investigations (section 5.1) characterize the single-point Raman spectra obtained from within the nucleus of four selected cells, for each cell type (A549 and DU145). A detailed analysis of the observed Raman features in the cell spectra is also provided (section 5.1.2). Horizontal line scans across the nuclear region of the same four selected cells, for each cell type, are then presented and discussed (section 5.2). This analysis quantifies the spectral variability within a single cell, and correlates observed signals with visually observed cell structures. Continuing onward in imaging complexity, Raman peak intensity maps of protein and DNA bands from a single selected cell of each cell type are presented and discussed (section 5.3). Lastly, the results are summarized and discussed, and some initial conclusions are made regarding intra-batch spectral variability (section 5.4).

5.1 Single-point spectra of A549 and DU145 cell nuclei

5.1.1 Optical images and Raman spectra of selected cells

For the purposes of this study, four A549 cells and four DU145 cells were chosen for full analysis. The four cells were chosen simply to cover a wide range of variability in both general appearance and Raman spectral response (the origins of this variability are discussed in section 5.4). Optical images of the selected A549 cells are shown in figure 5.1, and images of the selected DU145 cells are shown in figure 5.2. The red spot on the images estimates the position and area of Raman collection, with the 100x objective, based on the known spatial resolution and laser spot size measurements

presented in chapter 4. Figures 5.1 and 5.2 show that signal is collected from a very small fraction of the total volume of the cell. The locations of all the single-point Raman collections were chosen to be as close to the centre of the cell's nuclear region (if visible) as possible.

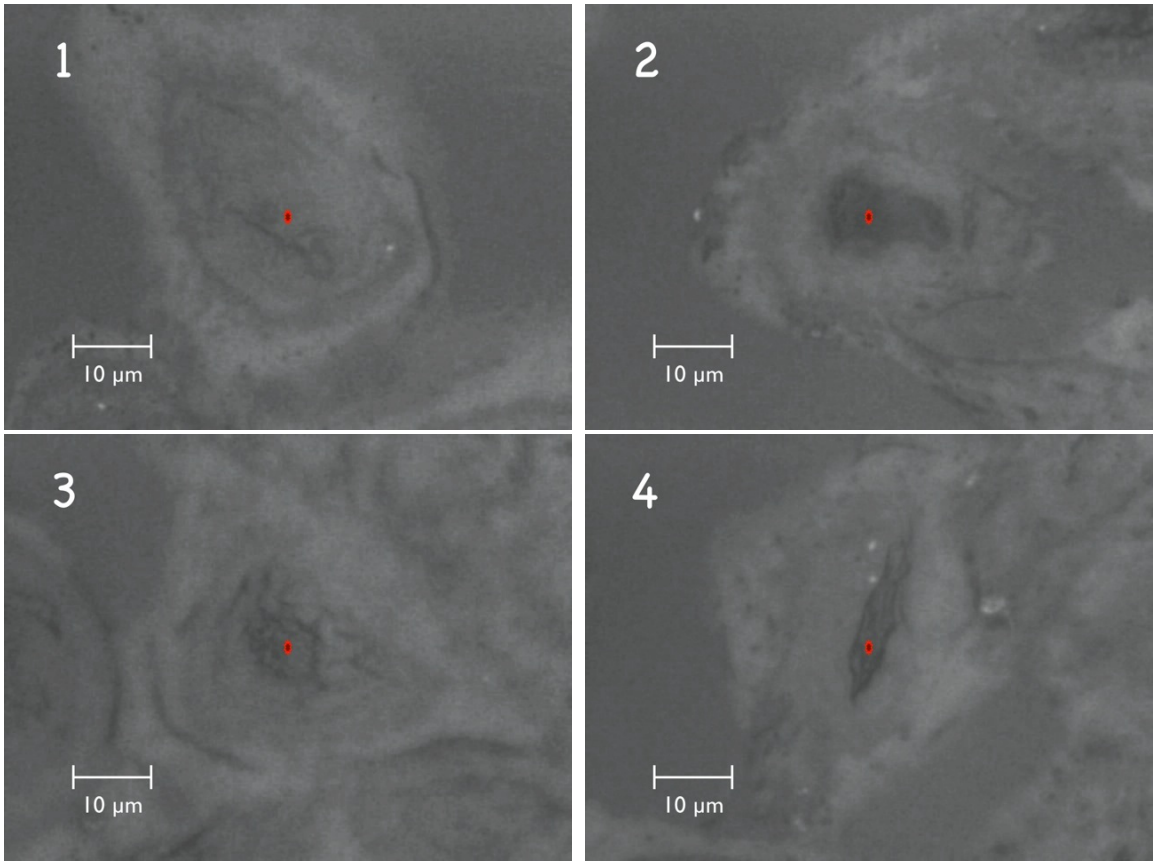

Figure 5.1: Optical microscope images of A549 cells 1-4, obtained with the 50x objective. Red spot shows estimate of theoretical collection area. Field of view is 72 × 54 μm.

Recall from chapter 3, section 3.2.3, that in order to cover the full spectral window acquired in this work (700-1850 cm^{-1}), two diffraction grating angles, and therefore two separate acquisitions, are required. Therefore, all cell spectra shown in this chapter are displayed such that the low-wavenumber and high-wavenumber figures are adjacent. In this manner, raw single-acquisition Raman spectra for the A549 cells are shown in figures 5.3a-b, and the corresponding spectra for the DU145 cells are shown in figures 5.4a-b. Also shown in these figures is the raw signal from the quartz

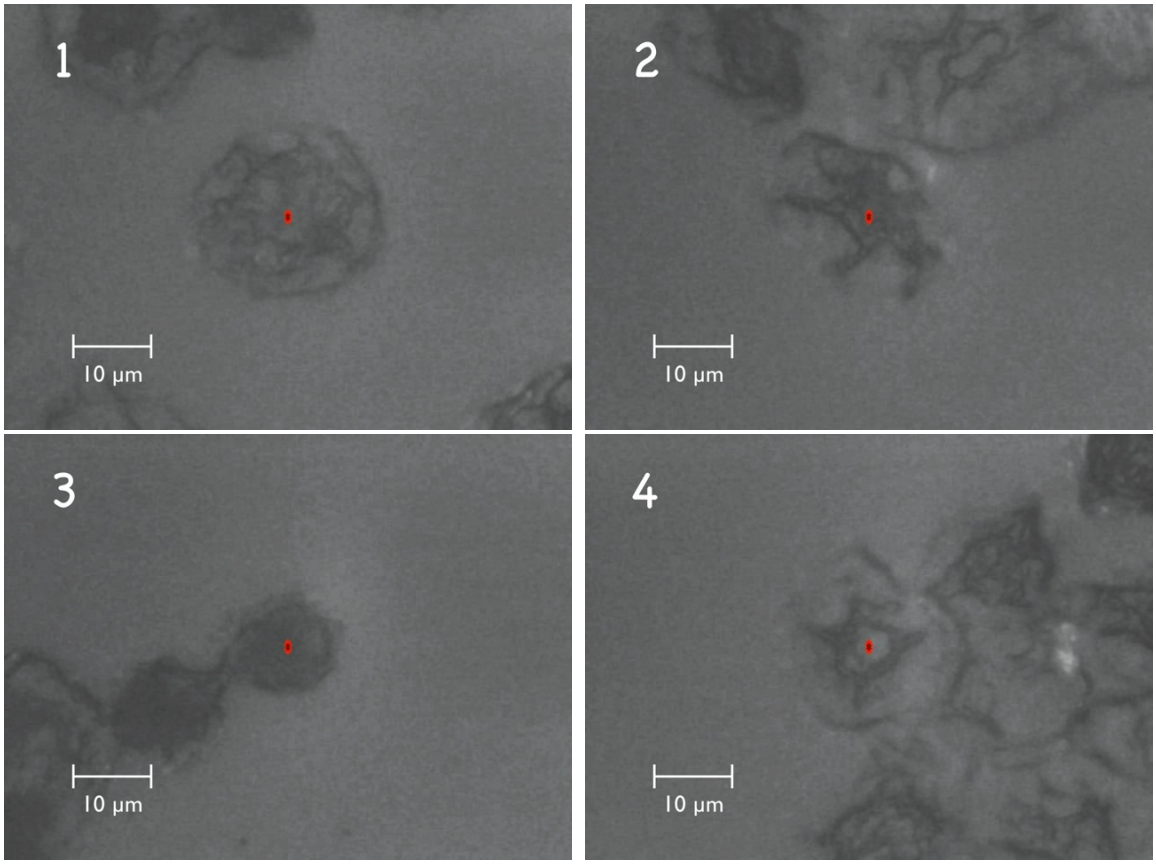

Figure 5.2: Optical microscope images of DU145 cells 1-4, obtained with the 50x objective. Red spot shows estimate of theoretical collection area. Field of view is 72×54 μm.

substrate (yellow spectra), obtained directly from the quartz at a nearby location to the four cells, at the same focus depth. The black trace shows the result of TPMEM smoothing on the quartz background, which was then subtracted from each raw cell spectra before further processing. Four 2-minute acquisitions per cell, per grating angle, were obtained, and figures 5.3c-d and 5.4c-d show the resulting A549 and DU145 cell spectra after subtracting the quartz background, removing any cosmic rays, averaging the four spectra from each cell, and applying TPMEM smoothing.

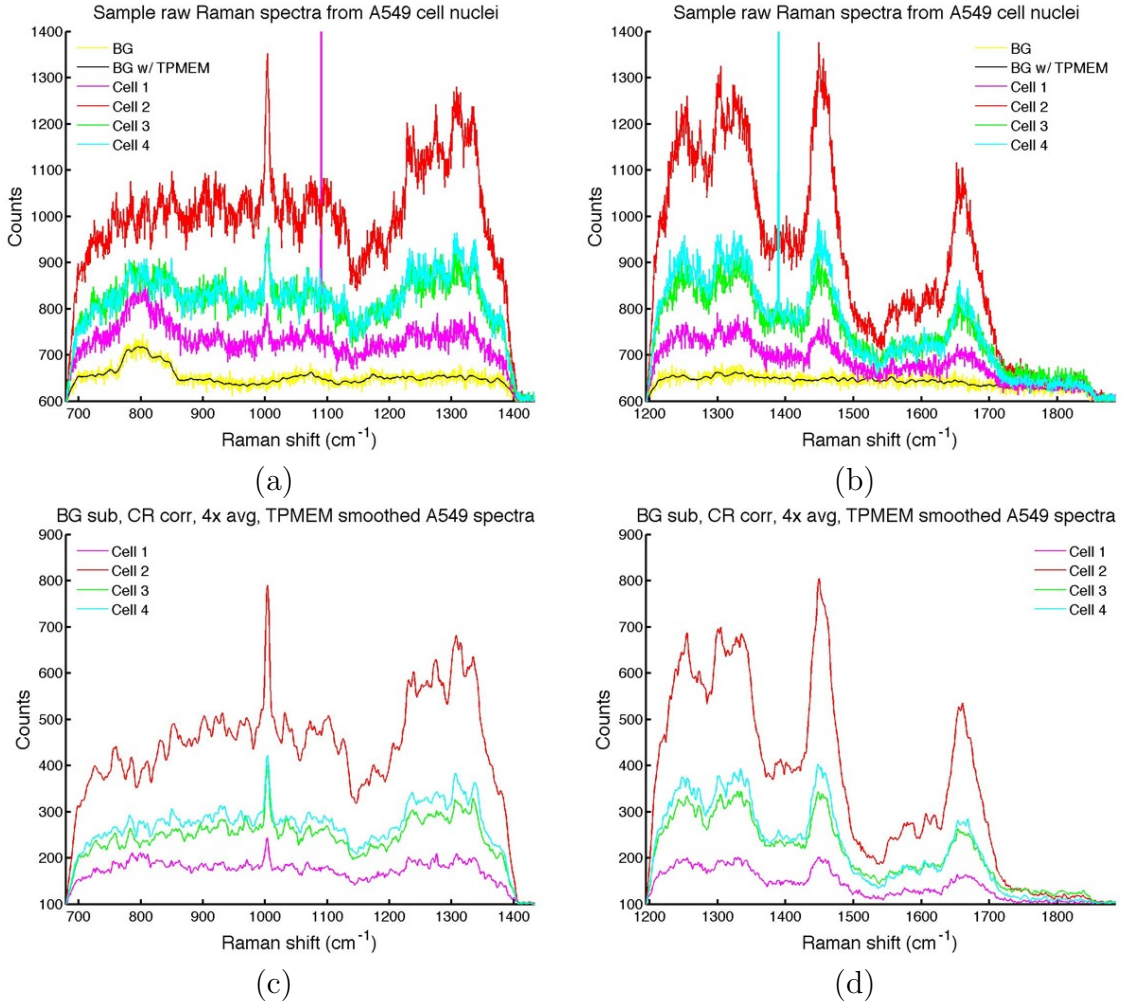

Figure 5.3: Single-point Raman spectra of the four A549 cell nuclei shown in figure 5.1. (a,b) Sample raw spectra from each cell and the quartz substrate (BG), and (c,d) fully processed spectra after quartz background subtraction, cosmic ray (CR) removal, 4x averaging, and TPMEM smoothing. Acquisition time = 2 min, laser power ∼50 mW at the sample.

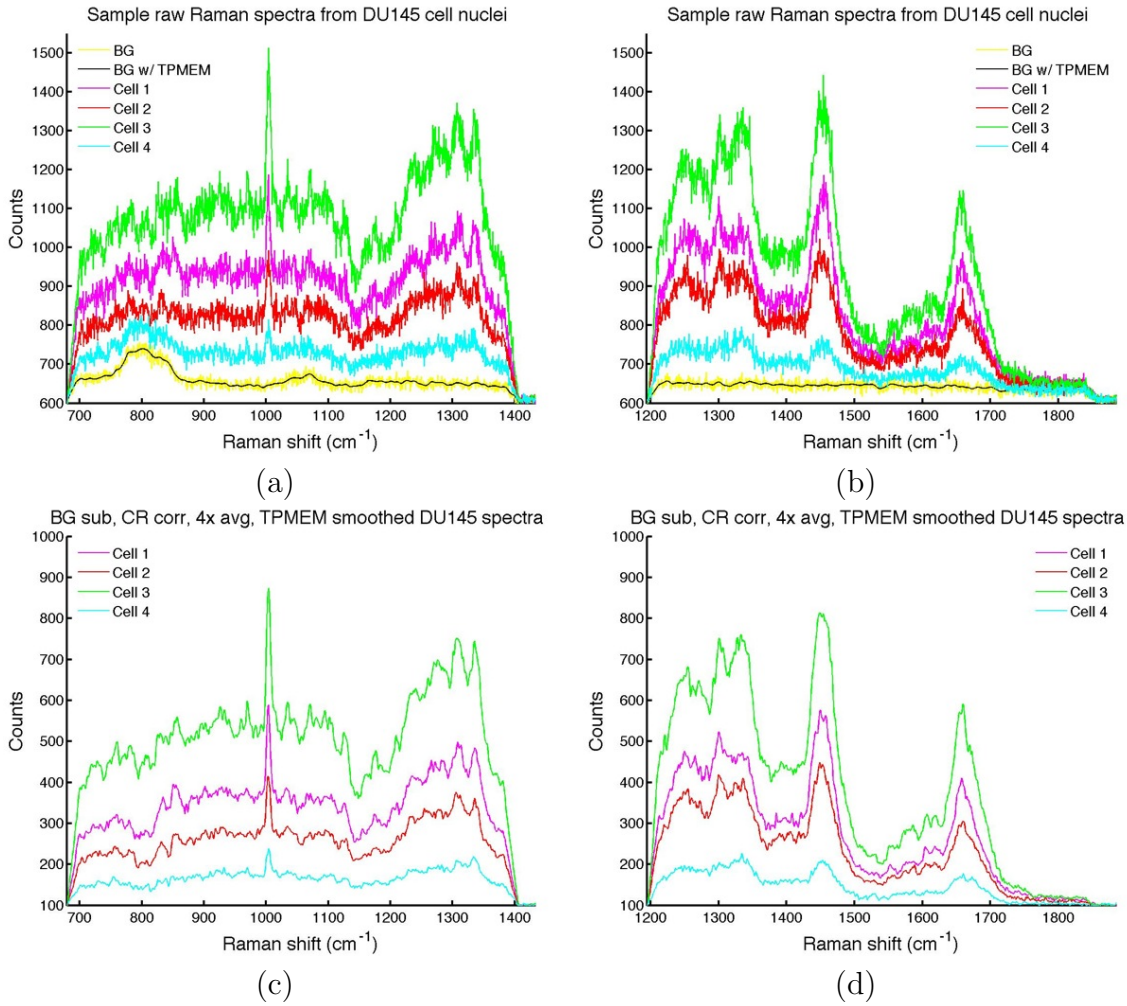

Figure 5.4: Single-point Raman spectra of the four DU145 cell nuclei shown in figure 5.2. (a,b) Sample raw spectra from each cell and the quartz substrate (BG), and (c,d) fully processed spectra after quartz background subtraction, cosmic ray (CR) removal, 4x averaging, and TPMEM smoothing. Acquisition time = 2 min, laser power ∼50 mW at the sample.

A detailed analysis of the spectral features will be presented in section 5.1.2, but for now it can be seen that there are a few obvious Raman peaks that dominate the spectra: a sharp peak near 1000 cm^{-1}, a broad peak near 1450 cm^{-1}, and another broad peak near 1650 cm^{-1}. There is also a significant underlying baseline, upon which the Raman peaks are superimposed, which can be attributed to fluorescence from biological material (all the single-point spectra obtained for this section are presented without applying any baseline correction). The measured Raman shifts for each peak are very constant between spectra (i.e., < 1 cm^{-1} variability), as is the general shape of the baseline. However, it is immediately evident that there is significant variability in spectral intensity between the chosen cells in terms of the height of the fluorescent baseline, and in terms of the Raman peak height above the baseline. The nature of this spectral variability will be examined further in sections 5.2 and 5.3, and will be thoroughly discussed in section 5.4.

5.1.2 Raman peak assignments for A549 and DU145 cells

Human cells are composed of all four types of biomolecules, namely proteins, lipids, carbohydrates, and nucleic acids. As such, the Raman spectra obtained from a cell will have contributions (however minor) from all types of biomolecules. The single-point spectra displayed in the previous section all show the same major Raman peaks, but only the strongest signal spectra detect weaker features. As such, for the purpose of assigning a molecular origin to as many peaks as possible, the strongest spectra obtained for each cell type are plotted in figure 5.5. The two spectra shown are from A549 cell 2 and DU145 cell 3. Almost all of the peaks visible in figure 5.5 were successfully assigned based on human cell Raman spectra recently reported in the literature [30–32, 41]. The locations of the peaks are indicated by arrows, accompanied by the Raman shift (in cm^{-1}), and, if possible, the type of biomolecule (d=DNA / nucleic acid, p=protein, lp=lipid, c=carbohydrate) and specific molecular bond or group responsible for the Raman scattering.

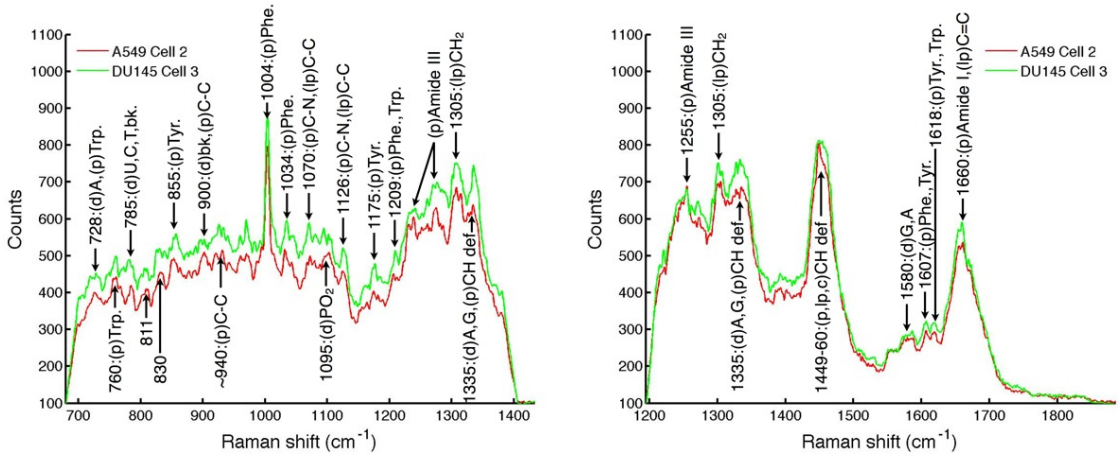

Figure 5.5: Raman peak assignments for A549 (cell 2) and DU145 (cell 3) spectra. For each peak (if possible), the Raman shift (in cm^{-1}), biomolecule type (d=DNA, p=protein, lp=lipid, c=carbohydrate), and specific molecule or bond type is given (see table 5.1 for further description). Abbreviations - A: adenine, U: uracil, C: cytosine, T: thymine, G: guanine, bk: backbone, Trp: tryptophan, Tyr: tyrosine, Phe: phenylalanine, def: deformation.

A more detailed description of the peak assignments is given in table 5.1. For each observable peak in figure 5.5, table 5.1 lists the type of biomolecule, the specific molecule or bonds responsible, and, if possible, the type of molecular vibration. In some cases, Raman peaks arising from more than one biomolecule type overlap to form only one detectable peak. For example, the 728 cm^{-1} peak has contributions from the DNA base adenine (A), the amino acid tryptophan (Trp.), and the carbon-nitrogen bonds (C-N) in phospholipids. In other cases, Raman peaks arising from different sub-units of the same biomolecule type will overlap to form a single peak. For example, the 785 cm^{-1} peak has contributions from the aromatic ring breathing of the nucleic acid pyrimidines uracil (U), cytosine (C), and thymine (T), as well as from the stretching of the oxygen-phophorus-oxygen (O-P-O) bonds in the phosphate groups that comprise the DNA backbone (recall chapter 1, figure 1.2).

The strongest features present in all spectra acquired in this study arise from proteins. The sharp peak at 1004 cm^{-1} is due to the aromatic ring breathing in

the amino acid phenylalanine (Phe.). The cluster of peaks between 1250 and 1300 cm^{-1} is largely due to amides, which are the molecular groups resulting from the formation of peptide bonds, the links that result when amino acids join together to form proteins (recall chapter 1, figure 1.1). The strong broad peak at 1449 cm^{-1} is due to deformations of carbon-hydrogen (CH) bonds, which are common to all biomolecules but are mainly found in proteins, lipids and carbohydrates. The strong broad peak at 1660 cm^{-1} is primarily an amide group feature. Other weaker protein signatures are detectable as well. The aromatic ring breathing of the amino acids tryptophan (Trp.) and tyrosine (Tyr.) give peaks at 728 and 760 cm^{-1}, and 830 and 855 cm^{-1}, respectively. Cytoskeleton proteins give peaks from carbon-carbon (C-C) bonds at 900 and 940 cm^{-1}, and other various amino acid vibrations give rise to peaks at 1034, 1209, 1607 and 1618 cm^{-1}.

The only two peaks that are solely lipid in origin are at 811 cm^{-1}, arising from the O-P-O vibrations in phospholipids, and at 1305 cm^{-1}, arising from the twisting of the CH_2 groups which form the long hydrocarbon chains found in all lipids.

Many DNA (or nucleic acid) signals in human cell spectra compete with Raman signals from other biomolecules (mainly proteins). However, two peaks are distinct DNA spectral markers. The first is the 785 cm^{-1} peak (described above), and the second is the 1580^{-1} peak, which arises from ring vibrations in the nucleic acid purines adenine (A) and guanine (G).

For the remainder of this study the spectral analysis is restricted to four Raman peaks: the two strongest peaks, the phenylalanine peak at 1004 cm^{-1} and the CH deformation peak at 1449 cm^{-1}, and the two distinct DNA peaks at 785 cm^{-1} and at 1580 cm^{-1}. For simplicity, the Phe. 1004 cm^{-1} and the CH def. 1449 $^{-1}$ peaks will both be referred to as "protein" signals.

Table 5.1: Peak assignment for Raman spectra of A549 and DU145 cells. Superscript numbers indicate references used for the particular assignment.

Peak Position (cm^{-1})	Assignment			
	DNA / RNA	Proteins	Lipids	Carbohydr.
728	A[30–32, 41]	Trp ring br[41]	C-N[41]	
760		Trp ring br[41]		
785	U,C,T ring br[30–32, 41] O-P-O str[31, 41]			
811			O-P-O[41]	
830	O-P-O str[31, 41]	Tyr ring br[30, 31, 41]		
855		Tyr ring br[30, 31, 41]		
900	backbone[31, 41]	C-C skeletal modes[31]		
∼940		α-helix[31, 41] C-C skeletal modes[30, 31, 41]		
1004		Phe sym ring br[30–32, 41]		
1034		Phe C-H in plane[31, 41]		
1070		C-N str[31, 41]	C-C str[30, 41]	C-O str[31, 41]
1095	PO_2^-[30–32, 41]	C-N str[31]	C-C str[41]	C-C str[41]
1126		C-N str[31, 41]	C-C str[30, 41]	
1209		Phe, Trp C-C_6H_6 str[30, 31, 41]		
1239		Amide III β-sheet[30, 31, 41]		
1255		Amide III β-sheet[30, 31, 41]		
1274		Amide III α-helix[41]		
1305			CH_2 tw[30, 41]	
1335	A[30, 31, 41], G[41]	CH def[41]		
1449		CH def[30–32, 41]	CH def[41]	
1460		CH def[41]	CH def[41]	CH def[41]
1580	A, G[30–32, 41]			
1607		Phe, Tyr C=C[41]		
1618		Tyr, Trp C=C[41]		
1660		Amide I α-helix[30–32, 41]	C=C str[30, 41]	

Abbreviations - A: adenine, U: uracil, C: cytosine, T: thymine, G: guanine, Trp: tryptophan, Tyr: tyrosine, Phe: phenylalanine, br: breathing, def: deformation, str: stretch, tw: twist, sym: symmetric.

5.2 Raman profiles across A549 and DU145 cells

In section 5.1.1, significant variability was observed in the intensity of Raman scatter between cell nuclei. From the optical images of the A549 and DU145 cells in figures 5.1 and 5.2, it is apparent that there is a rough correlation between optical image "darkness" within the cell at the location of Raman collection, and the resulting intensity of the Raman spectra. A darker central region of a cell very likely corresponds to an increased concentration of dense nuclear material. The concentration of proteins and nucleic acids in the nucleus is significantly higher than in the cell cytoplasm [31, 96], and as such it is natural to expect that for a cell with a highly concentrated "dark" nuclei, one would expect to measure more protein and DNA signals than from a cell with a less concentrated, "light" nuclear region. In addition, one would expect to see a sharp increase in the Raman signal collected over the darker regions of the cell, which correspond to dense nuclear material, when compared to the lighter regions of the same cell, which correspond to the cytoplasm or other structures. To further investigate this hypothesis, Raman profiles through all four A549 and DU145 cell nuclei were collected, the results of which are displayed and discussed below.

5.2.1 A549 cells

Raman profiles through the nuclei of A549 cells 1, 2, 3 and 4 are shown in figures 5.6a, 5.6b, 5.6c and 5.6d, respectively. The peak intensities of the Phe. 1004 cm^{-1} peak, the CH def. 1449 cm^{-1} peak, the DNA 785 cm^{-1} peak, and the DNA 1580 cm^{-1} peak are plotted together as a function of position across the cell, given by the locations of the red spots in the optical images. The peak values that make up the profiles shown were obtained after applying baseline correction using the methods described in chapter 3, and include a constant baseline offset of 100 counts which was applied to the spectra after baseline subtraction. As such, the profile values represent the Raman peak intensity above the fluorescent background signal, plus

100 counts. Baseline correction was necessary since the amount of fluorescence itself varies significantly across the cell area.

It is clear from figure 5.6 that the intensity of the protein signal collected is highly dependent on the presence of dark nuclear material at the point of collection. This is most evident when comparing the profiles of cell 1, which is a very "light" cell with no discernible dark regions (figure 5.6a), to those of cell 2, which has a very well defined dark central region (figure 5.6b). The cell 1 profiles give very little Raman signal (protein or otherwise), whereas the cell 2 profiles give a dramatic increase in protein signal over the central dark region. Outside of the central dark region, the cell 2 profiles show comparable signal to cell 1 ($\sim$50 counts above baseline). This effect is also seen in cell 4 (figure 5.6d), where very little signal (if any) is observed, except in the very narrow central dark region.

The spectral SNR is too poor to detect much DNA signal from these cells, but there is a very slight rise in the 785 cm^{-1} peak over the central dark regions of cells 2 and 4 (figures 5.6b and 5.6d), and a similar rise in the 1580 cm^{-1} peak over cell 2 (figure 5.6b). However, the scattered intensity is too weak to draw any quantitative conclusions about DNA distribution within these cells, except that DNA signals are indeed detectable within the nuclear region of cells 2 and 4, but not detectable elsewhere.

5.2.2 DU145 cells

In the exact same manner as the A549 cell profiles described above, Raman profiles through the nuclei of DU145 cells 1, 2, 3 and 4 are shown in figures 5.7a, 5.7b, 5.7c and 5.7d, respectively. Since these cells are smaller, rounder, and more compact than the A549 cells, it is not as easy to delineate a dark nuclear region directly from the optical images.

Cell 1 appears round and relatively homogenous (figure 5.7a). The protein profiles for cell 1 are symmetric, peak in the middle, and fall off gradually away from the

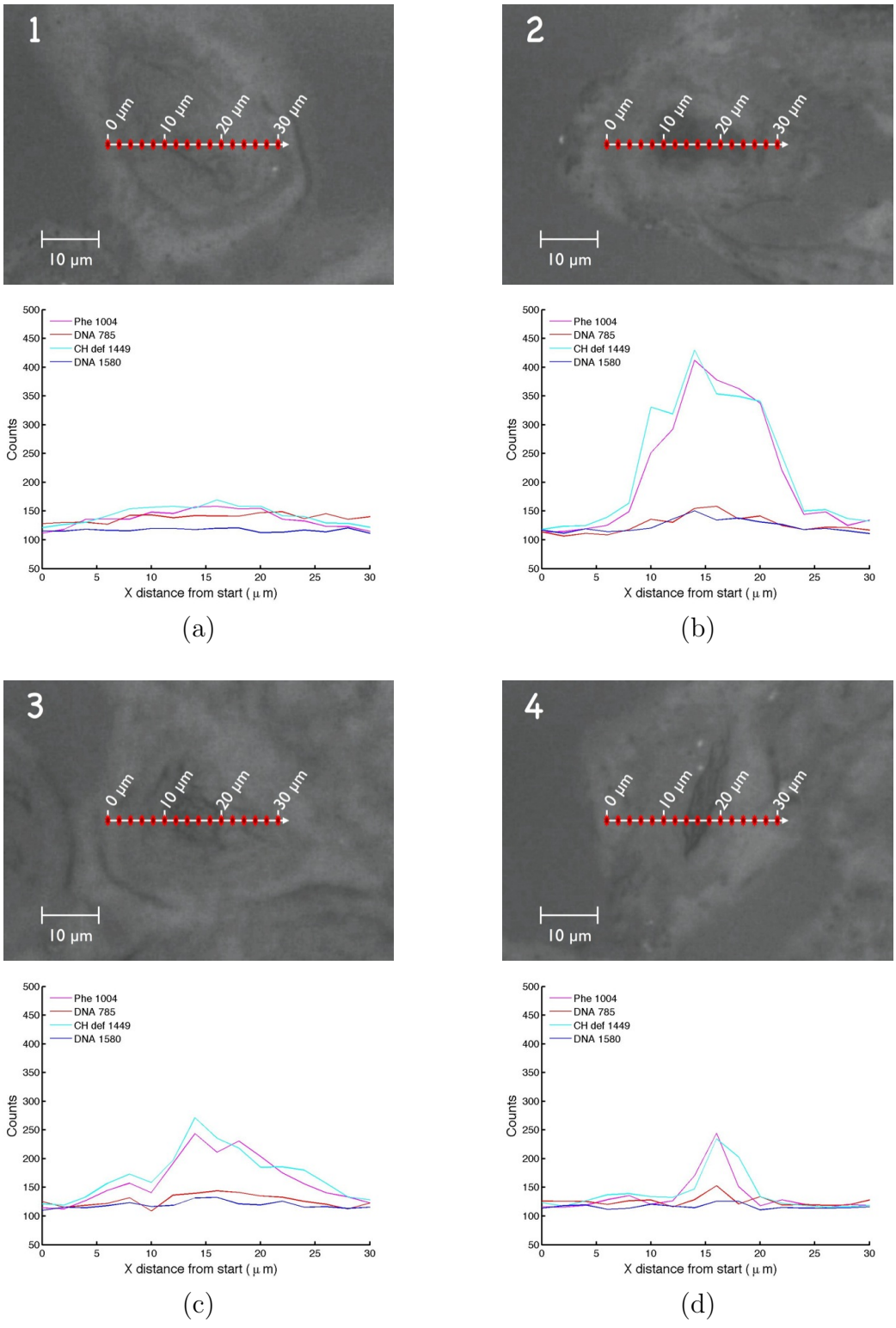

Figure 5.6: Optical images and Raman peak profiles of A549 cells (a) 1, (b) 2, (c) 3, and (d) 4. Optical images obtained with the 50x objective, and red spots show profile scan collection points. Field of view is 68×49 μm, scan step size is 2 μm. Acquisition time = 2 min / step, laser power $\sim$50 mW at the sample.

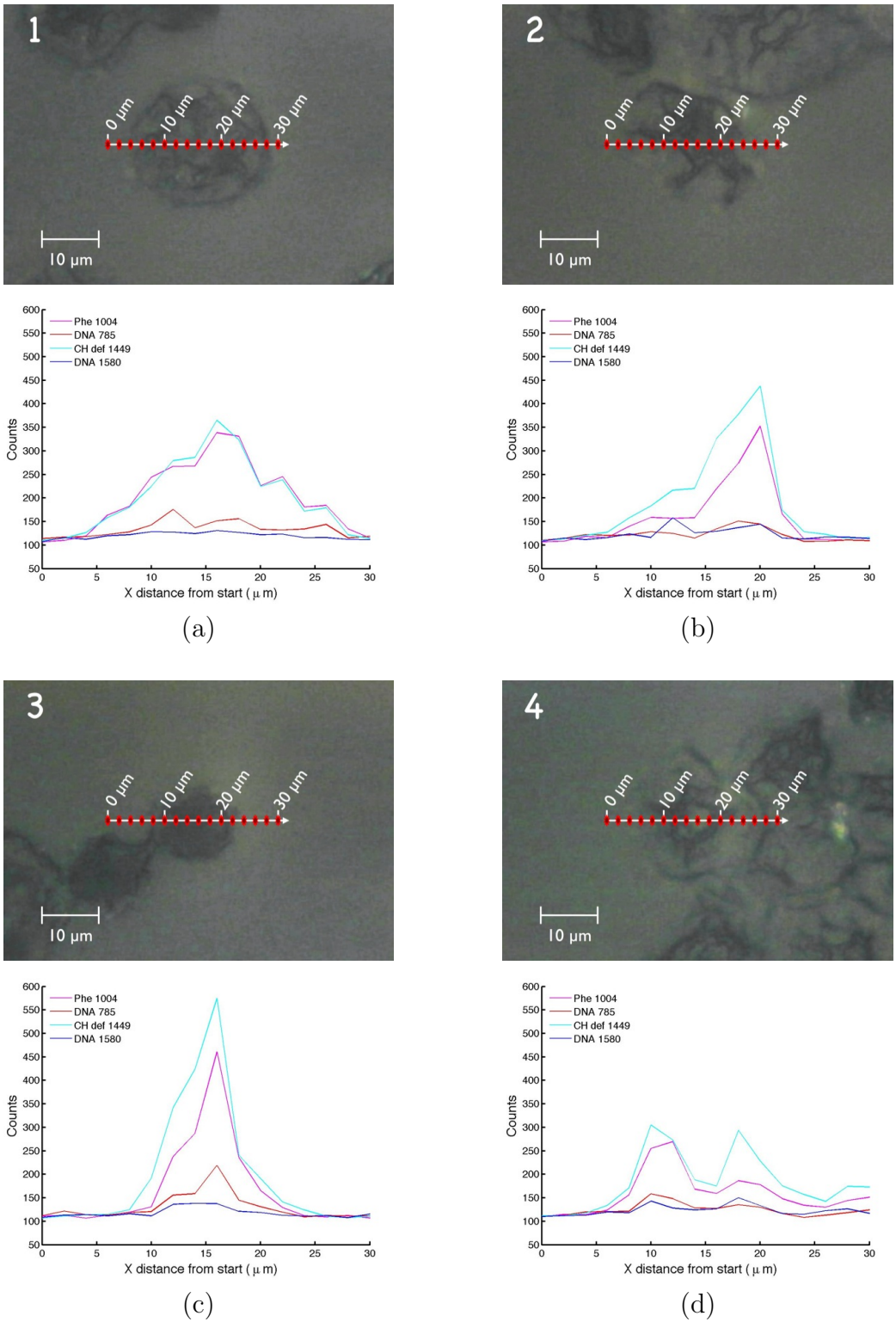

Figure 5.7: Optical images and Raman peak profiles of DU145 cells (a) 1, (b) 2, (c) 3, and (d) 4. Optical images obtained with the 50x objective, and red spots show profile scan collection points. Field of view is 68×49 μm, scan step size is 2 μm. Acquisition time = 2 min / step, laser power $\sim$50 mW at the sample.

cell centre, suggesting a rather spherical distribution of nuclear material that is not tightly concentrated. Cell 2, however, has a very distinct irregularly shaped dark nuclear region (figure 5.7b). The protein profiles seem to correlate well with the location of the dark region, showing a higher concentration of nuclear material in the right half of the cell.

For cell 3 (figure 5.7c) it is evident from the optical image that the cell was fixed during the process of division. When adherent cells divide, they tend to "round up" and become more loosely attached to the growth substrate. As such, the cell is smaller, thicker, and rounder, and thus darker throughout the observable area. It is likely due to the increased cell thickness, combined with an increased level of proteins required for cell division, that cell 3 yields the strongest amount of Raman signal compared to any other DU145 cell. A single dark nuclear region is not visible in the optical image, but the profiles clearly show a sharp increase in protein signals in the centre-right part of the cell. There is also a definite increase in the 785 cm^{-1} DNA peak at the same location, indicating a maximum concentration of both nuclear proteins and DNA. Cell 3 will be analyzed further in section 5.3.

Cell 4 (figure 5.7d) is also an interesting case, as the dark nuclear region forms a ring around a central light part of the cell. The profiles confirm that very little signal is detected in the light regions inside or outside the dark ring, and that the maximum protein signal arises purely from the ring itself. This cell is likely in a stage just prior to division, in which the nuclear material (protein and DNA) is actively being separated into two distinct groups by spindle fibers, which are protein-based themselves. Both DNA peak profiles indeed show a slight rise in peak intensity over the darker areas, correlating well with the rise in protein intensity.

5.3 Raman mapping of cells

To further investigate the protein and DNA distribution within the cells, and (more importantly) to demonstrate the ability of the RM system to perform such analyses, full Raman spectroscopic maps of A549 cell 4 and DU145 cell 3 were obtained. These cells were chosen due to their interesting structure, and because they yielded an appreciable amount of Raman signal. The A549 cell has a very dark narrow nuclear region, which yielded fairly strong protein signals, and some weak DNA signals as well. The DU145 cell has very little discernible internal structure from the optical image, yet has been fixed just before completing cell division, making it an interesting sample in itself. Furthermore, this cell yielded the strongest protein and DNA signals of all the Raman profiles displayed in section 5.2.

5.3.1 Raman mapping of A549 cell #4

The results from Raman mapping the protein distribution in the nuclear region of A549 cell 4 are shown in figure 5.8. The optical image (figure figure 5.8a) includes a 15×17 μm grid indicating the scan field of view (which encompasses most of the central dark nuclear region) and the points of Raman collection. The red spot shows the coordinate where the displayed sample spectra were obtained. The sample spectra plots (figures 5.8b & 5.8c) show the raw spectra, the TPMEM smoothed spectra, the baseline estimate, and the resulting spectra after baseline correction. The peak heights above the baseline are used to generate the Phe. and CH def. maps shown (figures 5.8d & 5.8e).

The CH def. map (figure 5.8e) clearly delineates the entire central dark nuclear region from the rest of the cell. The Phe. map (figure 5.8d) is nearly identical, except it shows a lack of Phe. signal in the top and bottom areas of the nuclear region, when compared to the CH def. distribution. This demonstrates that when mapping the protein distribution using RM, the results depend on which protein peak is selected.

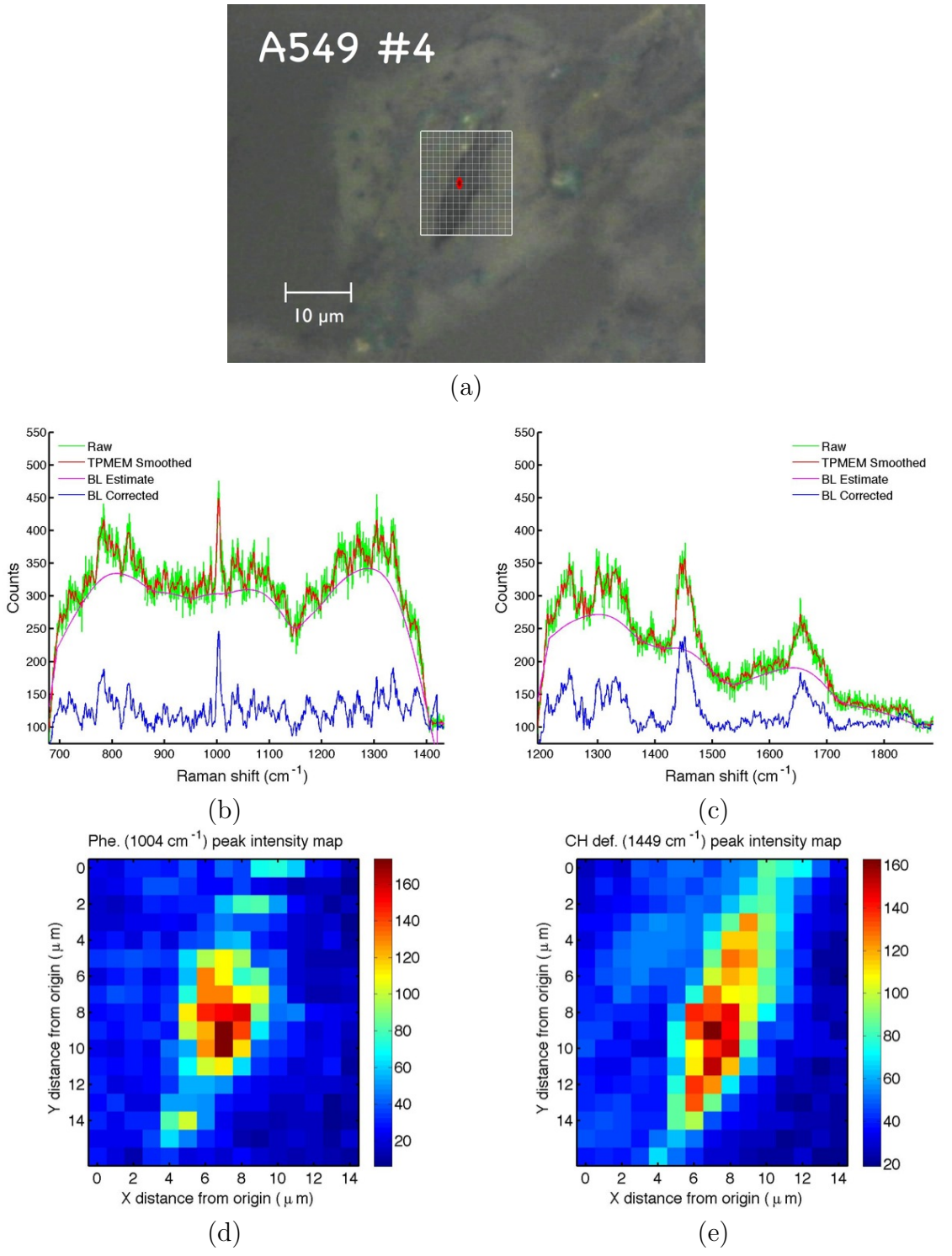

Figure 5.8: (a) Optical image, (b,c) sample spectra, and (d,e) protein maps of A549 cell #4. Optical image obtained with the 50x objective; white grid shows scan collection points and red spot shows position where displayed sample spectra were obtained. Optical field of view is 72×54 μm, scan field of view is 15×17 μm, and scan step size is 1 μm. Acquisition time = 2 min / pixel, laser power ~50 mW at the sample.

In this case, there could be an uneven distribution of Phe. amino acids with respect to the total protein distribution within the cell. Alternatively, the extra signal in the CH def. map could arise from lipids or carbohydrates.

The corresponding Raman maps of the two DNA peaks are shown in figures 5.9a and 5.9b. The SNR in these images is quite poor, so, for comparison, figures 5.9c and 5.9d show maps which were generated from the maximum intensity in spectral regions known to be devoid of Raman signals. This was done for a specific spectral range for each data set acquired: 870-875 cm^{-1} for the low-wavenumber data set (figure 5.9c), and 1520-1525 cm^{-1} for the high-wavenumber data set (figure 5.9d). These "no signal" maps represent the maximum noise floor contributions to any spectral map, assuming the noise floor is relatively constant across the spectral range, and the peaks chosen to create the map are not too near the edges of the spectra, where the baseline correction is problematic. Thus, by comparing the DNA maps to the "no signal" maps, it is evident that for both the low and the high-wavenumber data sets the DNA maps do show a measurable signal within the known nuclear region. However, the low SNR prevents any further conclusions from being drawn regarding DNA distribution with the cell.

5.3.2 Raman mapping of DU145 cell #3

In the same manner as presented above, the results from Raman mapping the protein distribution in the DU145 cell are shown in figure 5.10. The scan field of view is now 15×15 μm, which encompasses the entire visible area of the cell.

The conclusions drawn from the Phe. and CH def. maps of the DU145 cell are similar in nature to those drawn from the maps of the A549 cell, except that the nuclear region is not clearly visible in the optical image (figure 5.10a). However, the CH def. map (figure 5.10e) yields a highly concentrated band of Raman signal near the centre of the cell, which is oriented perpendicular to the cell division axis. Based on the previous results, it is very likely that the area of maximum CH def. intensity

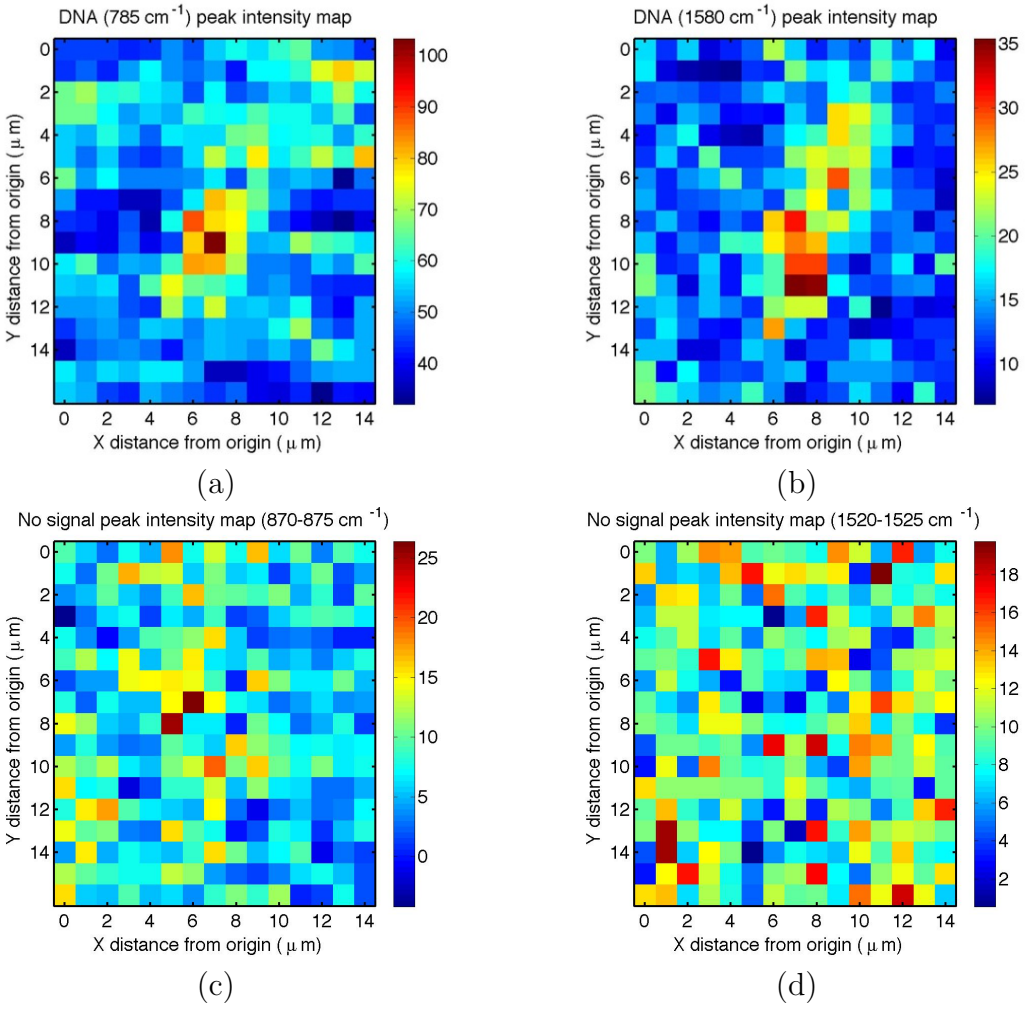

Figure 5.9: (a,b) Raman DNA maps of A549 cell #4, compared to (c,d) maps generated from the "no signal" region of same data set. Scan field of view is 15 × 17 μm, and scan step size is 1 μm. Acquisition time = 2 min / pixel, laser power ∼50 mW at the sample.

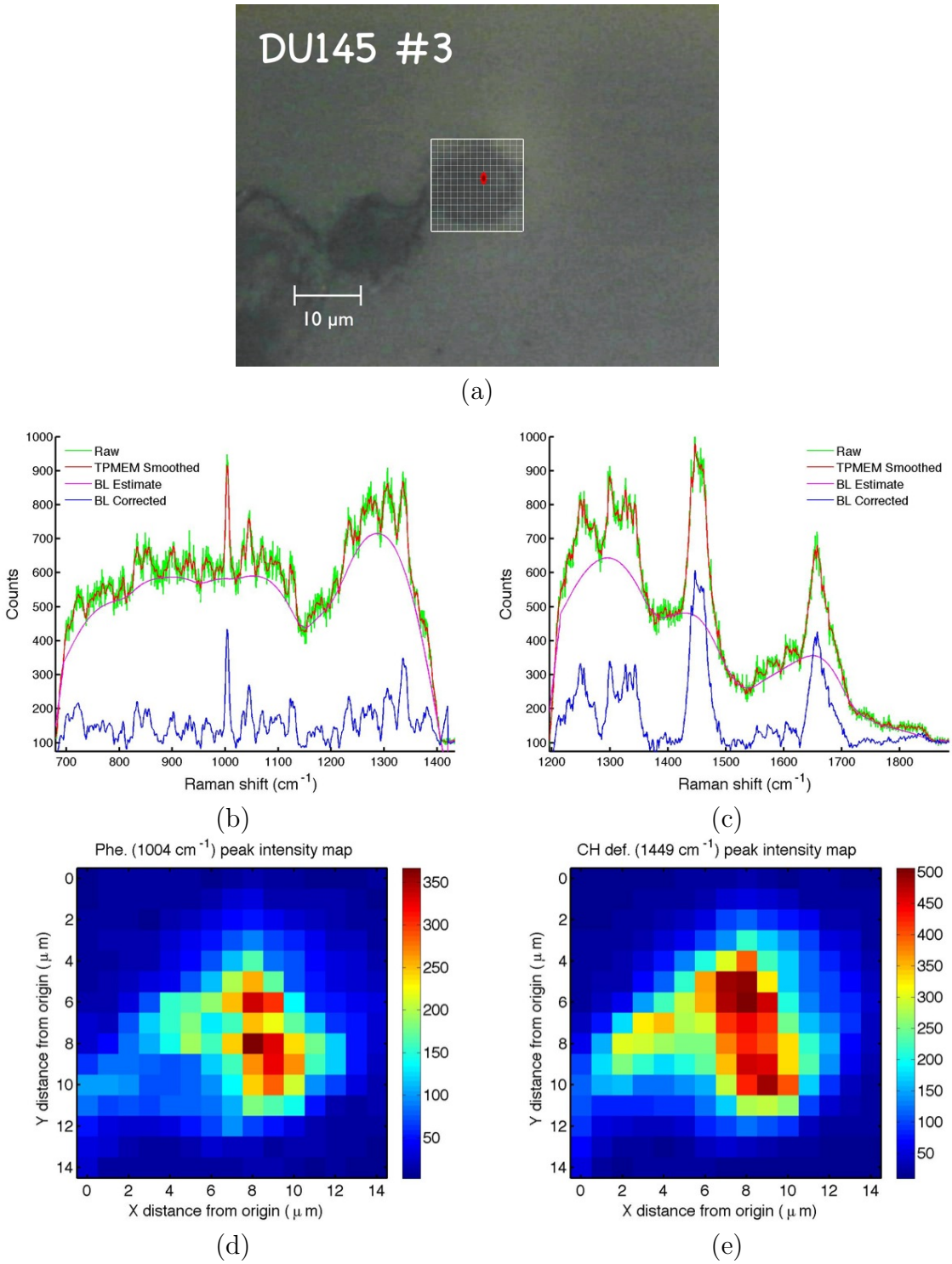

Figure 5.10: (a) Optical image, (b,c) sample spectra, and (d,e) protein maps of DU145 cell #3. Optical image obtained with the 50x objective; white grid shows scan collection points and red spot shows position where displayed sample spectra were obtained. Optical field of view is 72×54 μm, scan field of view is 15×15 μm, and scan step size is 1 μm. Acquisition time = 2 min / pixel, laser power ~50 mW at the sample.

indeed indicates the area of maximum nuclear material. As was found with the A549 cell, the Phe. map (figure 5.10d) displays a lack of signal in some areas of this nuclear region, and also in regions corresponding to the cell's mitotic "tail", which is more clearly outlined by the CH def. map (figure 5.10e).

The corresponding Raman maps of the two DNA peaks are shown in figures 5.11a and 5.11b. As was the case for the A549 cell, the SNR is quite low, so the "no signal" maps (generated from the same spectral ranges as for the A549 cell) are shown in figures 5.11c and 5.11d. By comparing the DNA maps to the "no signal" maps, it is evident that the DNA distribution is indeed detectable within this cell, and appears to be distributed rather evenly throughout the nuclear region outlined by the CH def. map. However, the SNR is too low to draw any more insightful conclusions.

5.4 Intra-batch cell spectral variability

In sections 5.1-5.3, it was shown that the most significant spectral differences arise from variations in the peak height above the baseline, and in the height of the baseline itself. These differences are correlated with optical image "darkness" in the area of Raman collection. This optical image darkness can be attributed to higher concentrations of dense nuclear material, which is reflected in the cell spectra both as higher levels of protein signal, and as detectable amounts of DNA signal. Since the height of the fluorescent baseline itself is also correlated with increased Raman peak height above the baseline, it is evident that there is indeed a higher concentration of biological material in the darker regions of the image, which gives rise to a higher fluorescent baseline. Simply stated, more nuclear material in the Raman collection volume yields both stronger Raman scattering and a stronger fluorescent baseline.

The important conclusion from these results is that the distribution and concentration of nuclear material is very different between individual cells, and as a result, the intensity of the Raman signal collected from a given cell is highly dependent on

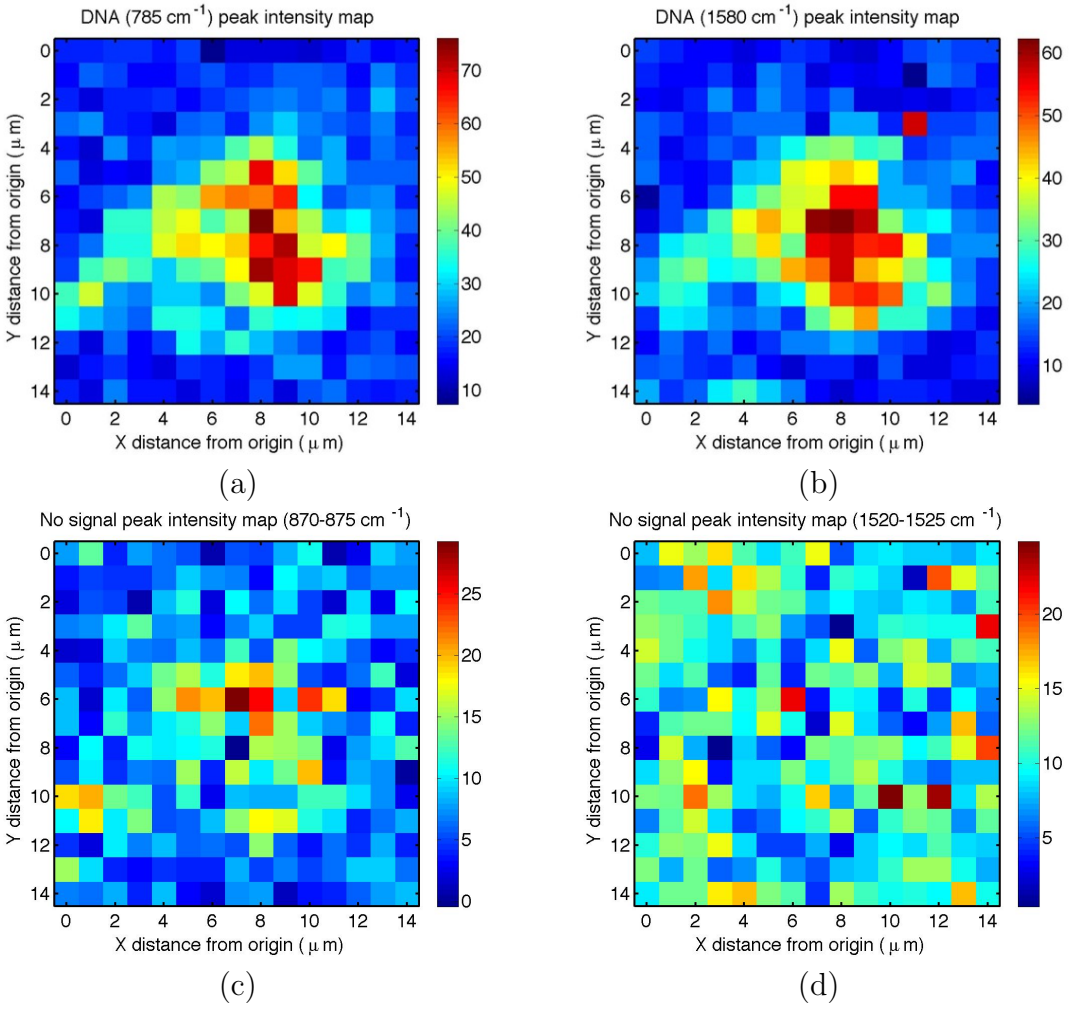

Figure 5.11: (a,b) Raman DNA maps of DU145 cell #3, compared to (c,d) maps generated from "no signal" region of same data set. Scan field of view is 15 × 15 μm, and scan step size is 1 μm. Acquisition time = 2 min / pixel, laser power ∼50 mW at the sample.

where you are sampling from within the cell. For the RM parameters used in this study, the sampling volume is roughly 1×2 μm wide and 3-4 μm in depth. This is a very small volume compared to the size of the adherent cells used in this experiment, which are on the order of 10-50 μm in diameter and 1-4 μm thick (cell thickness varies from 1-4 μm both between cells and within a given cell, depending on the distribution of nuclear material), and is also much smaller than the spread of nuclear material within a given cell. As such, the amount of Raman signal collected is very sensitive to local inhomogeneities within the cell.

It is important to recall that the primary application of this work will be to look for spectral differences between irradiated cells and non-irradiated cells. Since it is unfeasible with the current facilities to examine the exact same cell before and after irradiation, the inherent spectral variability between cells due to inhomogeneity of cell structure and nuclear material raises an interesting problem which will have to be addressed very carefully. Other research groups who have undertaken RM studies to compare the spectra from separate batches of human tumor cells have used different focusing optics such that the Raman collection volume encompasses either the entire cell [36, 41, 42], or multiple cells in a continuous tissue layer [35, 37, 44]. The spectra obtained are often normalized to the area of the CH def. peak, which is said to be a consistent marker of how much biological material is within the collection volume. However, this technique is only valid for inter-cell comparisons if the spectra is collected over a significant volume of the cell itself. As such, any information about the spatial location within the cell where spectral changes are occurring is lost.

A possible method to reduce the spectral variability between cells is to attempt to prepare the cells such that they grow in a more homogeneous fashion. However, the internal structure, morphology, and concentration of nuclear material in an adherent cell is strongly dependent on the local growth conditions (local cell density, substrate defects, access to growth media nutrients, etc...), the parent cell properties, and the

current phase of its cell cycle. There are known chemicals and protocols available to synchronize a cell culture with respect to cell cycle, but these protocols are not 100% efficient, and whether a cell will progress normally through a mitotic cycle depends heavily on its local growth conditions. Attempting to standardize the local growth conditions within a cell culture is difficult using standard lab techniques, but is an important issue that should be investigated.

An alternative method for reducing spectral variability is to improve the cell selection procedure such that it is known, with confidence *a priori*, that a certain part of a certain cell will yield a relatively consistent level of signal. In this study, the strongest observable correlation with Raman scattering intensity is the optical image "darkness". The image darkness at the point of collection can be quantified using the grayscale intensity in a region of interest (ROI) centered at the point of Raman collection, and with dimensions equal to the known collection area of the RM system.

To investigate the utility of such an approach with the current apparatus, 35 A549 cells were selected, and optical images were acquired of each cell. Single point Raman spectra were acquired from the central nuclear region of each cell, which was aligned with the centre of the optical image as best as possible. The mean grayscale intensity in a 1×2 μm ROI at the centre of the optical image was calculated, with a corresponding standard deviation. Figure 5.12 shows the resulting grayscale intensities plotted against the corresponding Raman peak intensities (above baseline) for the Phe. and CH def. peaks, using the standard deviation for the length of the vertical error bars. Also included for comparison are the maximum intensities of the "no signal" spectral regions described in section 5.3.

Figure 5.12 does indeed show a correlation between a decreased grayscale intensity (increased image darkness) and an increased peak intensity of the two protein bands. However, the distribution is very broad, and seems to broaden as the grayscale in-

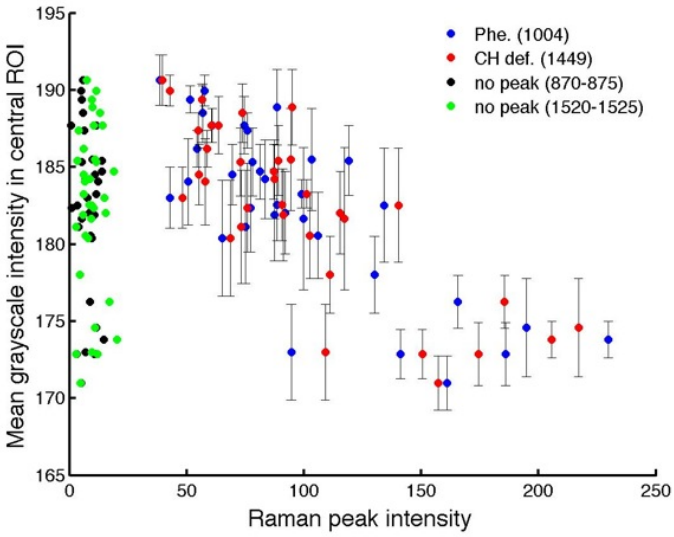

Figure 5.12: Relationship between mean grayscale intensity (optical "lightness") in A549 cell nuclear regions (ROI approximates true Raman collection area) and the Raman peak intensity from protein bands (Phe. and CH def.), acquired from 35 individual A549 cell nuclei. Acquisition time = 2 min per cell, laser power ∼50 mW at the sample. Error bars obtained from the standard deviation of the mean grayscale intensity in the collection ROI.

tensity decreases. It is likely that this is partially due to the poor contrast and poor resolution in the optical imager itself. In addition, there is a significant amount of local inhomogeneity in the dark nuclear regions that is not detected by the optical imager, but will have a large effect on the intensity of Raman scatter. For example, figure 5.12 shows that at grayscale intensities below 175, the measured Raman peak intensities range from ∼100 to over 200 counts, indicating a 100% difference in peak intensity for the same measured grayscale intensity. Even for grayscale intensities of, for example, ∼182, the Raman peak intensities range from ∼50 to just under 150 counts, indicating a 200% difference in peak intensity. As such, it would be very difficult to conduct any quantitative analyses with this data set.

Despite the difficulties presented here, there are many opportunities for improvement. This work was limited, due to the available equipment, by poor SNR and insufficient spectral window size (i.e., requiring two separate acquisitions to cover the necessary spectral window). The spectral SNR can be greatly improved by increas-

ing the laser power at the sample, and by collecting signal over the whole spectral window at once with longer acquisition times. In addition, it is definitely possible to improve the cell selection protocol by increasing the quality of the optical imaging equipment. There are also techniques available to decrease the inherent variability in a cell culture by synchronizing the cells with respect to cell cycle, and by controlling the local growth environment. Once the spectral variability has been reduced using any (or all) of these techniques, then spectral averaging over a large number of cells in a given culture will allow spectral comparisons between cultures. However, if the local inhomogeneity within a given cell proves to be too great a source of spectral variability that cannot be feasibly addressed, it is a fairly simple step to alter the focusing optics such that the Raman signal can be collected from the entire cell volume (or multiple cells) at once, at the expense of spatial information, allowing the aforementioned CH def. normalization technique to be utilized.

Chapter 6

Conclusions and Future Work

6.1 Conclusions

This work has been successful in developing a Raman microscopy (RM) system for future studies of the effects of ionizing radiation on human cells. Raman imaging of 5 μm diameter microbeads dispersed on silicon has shown that the apparatus is suitable for RM investigation of the interior structure of single cells. This analysis has also shown that the RM system is optimized for sub-cellular imaging when using the 100x objective and the 50 μm confocal collection aperture. Methods have been implemented for obtaining quantitative measurements of the spatial, confocal, and spectral resolution of the RM system; furthermore, the resolution values obtained in this work are competitive with those of modern commercial RM systems, and are suitable for RM of single cells.

Protocols for cell culture and sample preparation have been developed, and low-fluorescence quartz has been shown to be a suitable substrate material for RM of cells. Human lung (A549) and prostate (DU145) tumor cells have been analyzed successfully with the RM system, through (i) the collection of single-point spectra from cell nuclei, (ii) horizontal Raman profiles of protein and DNA signals across single cells, and (iii) 2D Raman maps of protein and DNA distributions within single cells. This analysis has shown that the intensity of Raman scattering from a single

cell is highly dependent on the local concentration of dense nuclear material within the cell, resulting in a high degree of variability in spectral intensity between cells in the same culture. Possible methods to address intra-batch variability of cell cultures have been discussed, such as altering the focusing optics, averaging over many cells, and cell-cycle synchronization.

6.2 Future work

Much of the future work will be performed using a new commercial RM system that has recently been purchased and installed (Renishaw Inc., Illinois, IL, USA). The new system has three distinct advantages over the RM system developed in this work: increased efficiency of Raman light collection, increased speed and efficiency of spatial scanning and mapping, and a novel spectrometer and diffraction grating design that allows for any desired spectral window width to be acquired in a single acquisition. The primary disadvantage of the new system is a loss of flexibility and accessibility due to a fully integrated and automated apparatus. In addition, the spectral resolution of the new system is limited due to a shorter spectrometer focal length. However, for RM of cells, the spectral resolution requirements are such that the new system should be more than adequate. The RM system used in this work will be useful in future investigations where increased spectral resolution is required. The first phase of future work will involve characterizing the performance of the new RM system, following the methods developed in this work.

For future studies, it will be necessary to develop a robust experimental method for comparing cell spectra, possibly implementing multivariate statistical methods such as principal component analysis or cluster analysis. It will also be necessary to account for intra-batch spectral variability. Possible methods for addressing this issue have been discussed, and the new RM system will be instrumental in these developments by providing higher signal-to-noise ratio cell spectra both faster and

more efficiently than was previously possible. Once the necessary experimental methods have been developed, preliminary radiotherapy irradiation experiments will be performed. Separate batches of A549 or DU145 cells will be cultured; one batch of cells will be irradiated, both cultures will be fixed using the methods described in this work, and a comparative Raman microscopic analysis of the two cultures will be performed.

Another future direction will be to apply RM to the study of live, unfixed cells, as it has been shown that the spectra obtained using RM are sensitive to the hydration state of a cultured human cell [30]. Live cells must remain in an aqueous environment during RM acquisition, which requires the use of a water immersion objective or an oil immersion objective with a cover slip. RM analysis of live cells, using both water and oil immersion objectives, will be investigated and characterized using the methods developed in this work, and comparative Raman microscopic analyses of irradiated and non-irradiated live cell cultures will follow.

Bibliography

[1] WC Röntgen. On a New Kind of Rays. *Nature*, 53(1369):274–276, 1896.

[2] JE Aldrich and BC Lentle. A New Kind of Ray: The Radiological Sciences in Canada. *University of British Columbia, Vancouver, BC*, 1995.

[3] D Brian. The Curies: A Biography of the Most Controversial Family in Science. *J. Wiley, Hoboken, NJ*, 2005.

[4] DI Thwaites and JB Tuohy. Back to the future: the history and development of the clinical linear accelerator. *Phys Med Biol*, 51:R343–R362, 2006.

[5] NCIC. Canadian Cancer Statistics. *National Cancer Institute of Canada*, 2008.

[6] HE Johns and JR Cunningham. The Physics of Radiology. *Charles C. Thomas Publisher, Springfield, Il*, 1983.

[7] FM Khan. The Physics of Radiation Therapy, 3rd edition. *Lippincott Williams & Wilkins, Philadelphia, PA*, 2003.

[8] EL Travis. Medical Radiobiology, 2nd edition. *Year Book Medical Publishers, Inc., Chicago, Il*, 1989.

[9] EJ Hall and AJ Giaccia. Radiobiology for the Radiologist, 6th edition. *Lippincott Williams & Wilkins, Philadelphia, PA*, 2006.

[10] Franklin Hutchinson. The Distance That a Radical Formed by Ionizing Radiation Can Diffuse in a Yeast Cell. *Radiat Res*, pages 473–483, 1957.

[11] M Dizdaroglu. Application of capillary gas-chromatography mass-spectrometry to chemical characterization of radiation-induced base damage of DNA - Implications for assessing DNA-repair processes. *Anal Biochem*, 144:593–603, 1985.

[12] DD Ager, WC Dewey, K Gardiner, W Harvey, RT Johnson, and CA Waldren. Measurement of radiation-induced DNA double-strand breaks by pulsed-field gel-electrophoresis. *Radiat Res*, 122:181–187, 1990.

[13] M Bergqvist, D Brattstrom, M Stalberg, H Vaghef, O Brodin, and B Hellman. Evaluation of radiation-induced DNA damage and DNA repair in human lung cancer cell lines with different radiosensitivity using alkaline and neutral single cell gel electrophoresis. *Cancer Lett*, 133:9–18, 1998.

[14] VS Dhillon, P Thomas, and M Fenech. Comparison of DNA damage and repair following radiation challenge in buccal cells and lymphocytes using single-cell gel electrophoresis. *Int J Radiat Biol*, 80:517–528, 2004.

[15] NCRP. Report #150: Extrapolation of radiation-induced cancer risks from non-human experimental systems to humans. *National Council on Radiation Protection & Measurements*, 2005.

[16] P Rubin. Clinical Oncology, 8th edition. *W. B. Saunders Company, Philadelphia, PA*, 2001.

[17] LJ Peters. Radiation therapy tolerance limits - For one or for all? Janeway lecture. *Cancer*, 77:2379–2385, 1996.

[18] FB Geara, LJ Peters, KK Ang, JL Wike, and WA Brock. Prospective comparison of in-vitro normal-cell radiosensitivity and normal tissue-reactions in radiotherapy patients. *Int J Radiat Oncol*, 27(5):1173–1179, 1993.

[19] WA Brock and SL Tucker. In vitro radiosensitivity and normal tissue damage. *Radiother Oncol*, 55(2):93–94, 2000.

[20] EP Malaise, B Fertil, N Chavaudra, and M Guichard. Distribution of radiation sensitivities for human-tumor cells of specific histological types - comparison of in vitro to in vivo data. *Int J Radiat Oncol*, 12(4):617–624, 1986.

[21] E López, R Guerrero, MI Nunez, R del Moral, M Villalobos, J Martinez-Galan, MT Valenzuela, J Munoz-Gamez, FJ Oliver, D Martin-Oliva, and JMR de Almodovar. Early and late skin reactions to radiotherapy for breast cancer and their correlation with radiation-induced DNA damage in lymphocytes. *Breast Cancer Res*, 7:R690–R698, 2005.

[22] H Nagasawa and JB Little. Induction of sister chromatid exchanges by extremely low-doses of α-particles. *Cancer Res*, 52(22):6394–6396, 1992.

[23] M Folkard, KM Prise, AG Michette, and B Vojnovic. The use of radiation microbeams to investigate the bystander effect in cells and tissues. *Nucl Instrum Meth A*, 580(1):446–450, 2007.

[24] WF Morgan and MB Sowa. Non-targeted bystander effects induced by ionizing radiation. *Mutat Res-Fund Mol M*, 616(1-2):159–164, 2007.

[25] GJ Puppels, FFM Demul, C Otto, J Greve, M Robertnicoud, DJ Arndtjovin, and TM Jovin. Studying single living cells and chromosomes by confocal Raman microspectroscopy. *Nature*, 347(6290):301–303, 1990.

[26] D Naumann, S Keller, D Helm, C Schulz, and B Schrader. FT-IR Spectroscopy and FT-Raman Spectroscopy are powerful analytical tools for the noninvasive characterization of intact microbial-cells. *J Mol Struct*, 347:399–405, 1995.

[27] KC Schuster, I Reese, E Urlaub, JR Gapes, and B Lendl. Multidimensional information on the chemical composition of single bacterial cells by confocal Raman microspectroscopy. *Anal Chem*, 72:5529–5534, 2000.

[28] KC Schuster, E Urlaub, and JR Gapes. Single-cell analysis of bacteria by Raman microscopy: spectral information on the chemical composition of cells and on the heterogeneity in a culture. *J Microbiol Meth*, 42:29–38, 2000.

[29] K Maquelin, C Kirschner, LP Choo-Smith, N van den Braak, HP Endtz, D Naumann, and GJ Puppels. Identification of medically relevant microorganisms by vibrational spectroscopy. *J Microbiol Meth*, 51:255–271, 2002.

[30] C Krafft, T Knetschke, A Siegner, RHW Funk, and R Salzer. Mapping of single cells by near infrared Raman microspectroscopy. *Vib Spectrosc*, 32:75–83, 2003.

[31] N Uzunbajakava, A Lenferink, Y Kraan, B Willekens, G Vrensen, J Greve, and C Otto. Nonresonant Raman imaging of protein distribution in single human cells. *Biopolymers*, 72:1–9, 2003.

[32] C Matthäus, S Boydston-White, M Miljković, M Romeo, and M Diem. Raman and infrared microspectral imaging of mitotic cells. *Appl Spectrosc*, 60:1–8, 2006.

[33] N Uzunbajakava, A Lenferink, Y Kraan, E Volokhina, G Vrensen, J Greve, and C Otto. Nonresonant confocal Raman imaging of DNA and protein distribution in apoptotic cells. *Biophys J*, 84:3968–3981, 2003.

[34] A Nijssen, TCB Schut, F Heule, PJ Caspers, DP Hayes, MHA Neumann, and GJ Puppels. Discriminating basal cell carcinoma from its surrounding tissue by Raman spectroscopy. *J Invest Dermatol*, 119(1):64–69, 2002.

[35] J Choi, J Choo, H Chung, DG Gweon, J Park, HJ Kim, S Park, and CH Oh. Di-

rect observation of spectral differences between normal and basal cell carcinoma (BCC) tissues using confocal Raman microscopy. *Biopolymers*, 77:264–272, 2005.

[36] P Crow, B Barrass, C Kendall, M Hart-Prieto, M Wright, R Persad, and N Stone. The use of Raman spectroscopy to differentiate between different prostatic adenocarcinoma cell lines. *Brit J Cancer*, 92:2166–2170, 2005.

[37] CM Krishna, GD Sockalingum, G Kegelaer, S Rubin, VB Kartha, and M Manfait. Micro-Raman spectroscopy of mixed cancer cell populations. *Vib Spectrosc*, 38:95–100, 2005.

[38] M Short, H Lui, D McLean, H Zeng, and M Chen. Preliminary micro-Raman images of normal and malignant human skin cells. *Proceedings of SPIE*, 2006.

[39] M Short, H Lui, D McLean, H Zeng, A Alajlan, and et al. Changes in nuclei and peritumoral collagen within nodular basal cell carcinomas via confocal micro-Raman spectroscopy. *Journal of Biomedical Optics*, 11(3):034004–9, 2006.

[40] BWD de Jong, TCS Bakker, K Maquelin, T van der Kwast, CH Bangma, DJ Kok, and GJ Puppels. Discrimination between nontumor bladder tissue and tumor by Raman spectroscopy. *Anal Chem*, 78(22):7761–7769, 2006.

[41] I Notingher, S Verrier, S Haque, JM Polak, and LL Hench. Spectroscopic study of human lung epithelial cells (A549) in culture: Living cells versus dead cells. *Biopolymers*, 72:230–240, 2003.

[42] S Verrier, I Notingher, JM Polak, and LL Hench. In situ monitoring of cell death using Raman microspectroscopy. *Biopolymers*, 74:157–162, 2004.

[43] K Sailer, S Viaggi, and M Nusse. Radiation-induced structural modifications in dsDNA analysed by FT-Raman spectroscopy. *Int J Radiat Biol*, 69:601–613, 1996.

[44] A Synytsya, P Alexa, J Besserer, J De Boer, and et al. Raman spectroscopy of tissue samples irradiated by protons. *International Journal of Radiation Biology*, 80(8):581–591, 2004.

[45] RJ Lakshmi, VB Kartha, CM Krishna, JGR Solomon, G Ullas, and PU Devi. Tissue Raman spectroscopy for the study of radiation damage: Brain irradiation of mice. *Radiat Res*, 157:175–182, 2002.

[46] F Adar, E Lee, S Mamedov, and A Whitley. Raman imaging: Defining the spatial resolution of the technology. *SPECTROSCOPY Supplement: Raman*, June:1–3, 2006.

[47] A Smekal. Zur Quantentheorie der Dispersion. *Naturwissenschaften II*, 43:873–875, 1923.

[48] CV Raman and KS Krishnan. A new type of secondary radiation. *Nature*, 121:501–502, 1928.

[49] J Brand. The Discovery of the Raman Effect. *Notes and Records of the Royal Society of London*, pages 1–23, 1989.

[50] CV Raman and KS Krishnan. A new class of spectra due to secondary radiation. *Indian J. Phys.*, 2:399–419, 1928.

[51] FP Kerschbaum. *Z. Instrumentenk*, 34:43, 1914.

[52] B Veskatesachar and L Sibaiya. *Indian J. Phys.*, 5:747, 1930.

[53] JH Hibben. The Raman Effect and Its Chemical Applications. *Reinhold Publishing Corp., New York, NY*, 1939.

[54] TR Gilson and PJ Hendra. Laser Raman Spectroscopy. *Wiley-Interscience, London, UK*, 1970.

[55] DH Rank, RJ Pfister, and PD Coleman. Photoelectric detection and intensity measurement in Raman spectra. *J Opt Soc Am*, 32:390–396, 1942.

[56] RF Stamm, CF Salzman, and T Mariner. Photoelectric Raman spectrometer with automatic range changing. I. Conversion of photographic instrument. *J Opt Soc Am*, 43(2):119–125, 1953.

[57] Y Talmi. Spectrophotometry and spectrofluorometry with the self-scanned photo-diode array. *Appl Spectrosc*, 36(1):1–18, 1982.

[58] DG Jones. Photodiode array detectors in UV-VIS spectroscopy. Part 1. *Anal Chem*, 57(9):1057A, 1985.

[59] PM Epperson, JV Sweedler, RB Bilhorn, GR Sims, and MB Denton. Applications of charge-transfer devices in spectroscopy. *Anal Chem*, 60(5):327A–335A, 1988.

[60] JE Pemberton, RL Sobocinski, and GR Sims. The effect of charge traps on Raman-spectroscopy using a Thomson-CSF charge coupled device detector. *Appl Spectrosc*, 44(2):328–330, 1990.

[61] E Smith and G Dent. Modern Raman Spectroscopy: A Practical Approach. *John Wiley & Sons Ltd, West Sussex, England*, 2005.

[62] JR Ferraro and K Nakamoto. Introductory Raman Spectroscopy. *Academic Press, Inc., San Diego, CA*, 1994.

[63] J Tang and AC Albrecht. Developments in the theories of vibrational Raman intensities, *in* "Raman Spectroscopy" (HA Szymanski, Ed.) Vol. 2. *Plenum Press, New York, NY*, 1970.

[64] H Eyring, J Walter, and GE Kimball. Quantum Chemistry. *John Wiley, New York, NY*, 1944.

[65] FA Cotton. Chemical Applications of Group Theory. *John Wiley, New York, NY*, 1971.

[66] JM Lerner and A Thevenon. The Optics of Spectroscopy - A Tutorial. *HORIBA Jobin Yvon Inc., Edison, NJ*, 1988.

[67] KR Spring and MW Davidson. Basic Concepts and Formulas in Microscopy. *Molecular Expressions, Tallahassee, FL*, 2008.

[68] JM Lerner and A Thevenon. An Introduction to Raman Spectroscopy. *HORIBA Jobin Yvon Inc., Edison, NJ*, 1988.

[69] GJ Puppels, JHF Olminkhof, GMJ Segersnolten, C Otto, FFM Demul, and J Greve. Laser irradiation and Raman spectroscopy of single living cells and chromosomes: sample degradation occurs with 514.5 nm but not with 660 nm laser light. *Exp Cell Res*, 195(2):361–367, 1991.

[70] I Notingher, S Verrier, H Romanska, AE Bishop, JM Polak, and LL Hench. In situ characterisation of living cells by Raman spectroscopy. *Spectroscopy*, 16(2):43–51, 2002.

[71] I Notingher, JR Jones, S Verrier, I Bisson, P Embanga, P Edwards, JM Polak, and LL Hench. Application of FTIR and Raman spectroscopy to characterisation of bioactive materials and living cells. *Spectroscopy*, 17(2-3):275–288, 2003.

[72] CM Creely, G Volpe, GP Singh, M Soler, and DV Petrov. Raman imaging of floating cells. *Optics Express*, 13(16):6105–6110, 2005.

[73] JW Chan, H Winhold, MH Corzett, JM Ulloa, M Cosman, R Balhorn, and T Huser. Monitoring dynamic protein expression in living E-coli. Bacterial Cells by laser tweezers raman spectroscopy. *Cytom Part A*, 71A:468–474, 2007.

[74] G Schulze, A Jirasek, MML Yu, A Lim, RFB Turner, and MW Blades. Investigation of selected baseline removal techniques as candidates for automated implementation. *Appl Spectrosc*, 59:545–574, 2005.

[75] M Yoshikawa and N Nagai. *in* "Handbook of Vibrational Spectroscopy" (J Chalmers and P Griffiths, Eds.) Vol. 4. *John Wiley & Sons, Inc., New York, NY*, pages 2593–2600, 2001.

[76] Y Nishimura and M Tsuboi. Local conformations and polymorphism of DNA duplexes as revealed by their Raman spectra, *in* "Advances in Spectroscopy" (RJH Clark and RE Hester, Eds.) Vol. 13. *John Wiley, New York, NY*, 1986.

[77] P Dhamelincourt, F Wallart, M Leclercq, AT N'Guyen, and DO Landon. Laser Raman molecular microprobe (MOLE). *Anal Chem*, 51:414A–421A, 1979.

[78] A Paipetis, C Vlattas, and C Galiotis. Remote laser Raman microscopy (ReRaM). 1 - Design and testing of a confocal microprobe. *J Raman Spectrosc*, 27(7):519–526, 1996.

[79] J Chalmers and P Griffiths (Eds.). Handbook of Vibrational Spectroscopy, Vol. 4. *John Wiley & Sons, Inc., New York, NY*, 2001.

[80] MD Schaeberle, DD Tuschel, and PJ Treado. Raman chemical imaging of microcrystallinity in silicon semiconductor devices. *Appl Spectrosc*, 55(3):257–266, 2001.

[81] CM Hodges and J Akhavan. The use of Fourier-transform Raman-spectroscopy in the forensic identification of illicit drugs and explosives. *Spectrochim Acta A*, 46(2):303–307, 1990.

[82] EA Cutmore and PW Skett. Application of Fourier-transform Raman-

spectroscopy to a range of compounds of pharmaceutical interest. *Spectrochim Acta A*, 49(5-6):809–818, 1993.

[83] TG Spiro (Ed.). Biological Applications of Raman Spectroscopy, Vol. 3. *John Wiley, New York, NY*, 1988.

[84] HU Gremlich and B Yan (Eds.). Infrared and Raman Spectroscopy of Biological Materials. *Marcel Dekker, Inc., New York, NY*, 2001.

[85] SW Smith. The Scientist and Engineer's Guide to Digital Signal Processing. *California Technical Publishing, San Diego, CA*, 2006.

[86] WH Richardson. Bayesian-based iterative method of image restoration. *J Opt Soc Am*, 62(1):55–59, 1972.

[87] LB Lucy. An iterative technique for the rectification of observed distributions. *Astronomical Journal*, 79(6):745–754, 1974.

[88] A Compaan, MC Lee, and GJ Trott. Phonon populations by nanosecond-pulsed Raman-scattering in Si. *Phys Rev B*, 32:6731–6741, 1985.

[89] A Jirasek, Q Matthews, M Hilts, G Schulze, MW Blades, and RFB Turner. Investigation of a 2D two-point maximum entropy regularization method for signal-to-noise ratio enhancement: application to CT polymer gel dosimetry. *Phys Med Biol*, 51:2599–2617, 2006.

[90] Q Matthews, A Jirasek, N Virji-Babul, A Babul, and T Cheung. Investigation of a two-point maximum entropy regularization method for signal enhancement applied to magnetoencephalography data. *Biomedical Signal Processing and Control*, 3:78–87, 2008.

[91] LS Greek, HG Schulze, MW Blades, AV Bree, BB Gorzalka, and RFB Turner.

SNR enhancement and deconvolution of Raman-spectra using a 2-point entropy regularization method. *Appl Spectrosc*, 49(4):425–431, 1995.

[92] HG Schulze, RB Foist, AI Jirasek, A Ivanov, and RFB Turner. Two-point maximum entropy noise discrimination in spectra over a range of baseline offsets and signal-to-noise ratios. *Appl Spectrosc*, 61:157–164, 2007.

[93] A Savitzky and MJE Golay. Smoothing and differentiation of data by simplified least squares procedures. *Anal Chem*, 36:1627, 1964.

[94] E Gazi, J Dwyer, NP Lockyer, J Miyan, P Gardner, C Hart, M Brown, and NW Clarke. Fixation protocols for subcellular imaging by synchrotron-based Fourier transform infrared microspectroscopy. *Biopolymers*, 77(1):18–30, 2005.

[95] J Russell. Raman spectrum of calcium fluoride. *P Phys Soc Lond*, 85:194–197, 1965.

[96] B Mohlenhoff, M Romeo, M Diem, and BR Wood. Mie-type scattering and non-Beer-Lambert absorption behavior of human cells in infrared microspectroscopy. *Biophys J*, 88(5):3635–40, 2005.